Parameter recovery in AC solution-phase voltammetry and a consideration of some issues arising when applied to surface-confined reactions

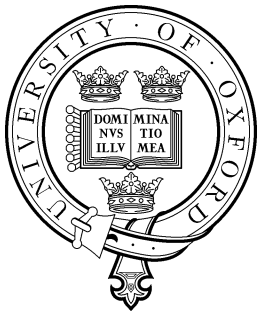

Graham Morris

St. Anne's College

University of Oxford

A thesis submitted for the degree of

Doctor of Philosophy

Trinity Term 2014

Acknowledgements

Any program of doctoral study is a long road, and this one has had its fair share of bumps. It is fair to say that without the steadfast support of many people, I may have slipped and fallen by the wayside.

Academically, my biggest thanks must go to my three supervisors for their patience and perseverance while working with me on this project. Professor David Gavaghan has enthusiastically lead the Oxford end of the AC voltammetry project for over a decade, and has always been able to offer positive advice and overall guidance. Dr Ruth Baker has given another perspective to the project, and helped to introduce some additional mathematical directions, as well as providing a constant reality check when things became unclear. Last but by no means least, Dr Kathryn Gillow has been a source of constant encouragement through the good and the bad, and has always been willing to make time to address even the smallest of problems. Special thanks also go to David and Kathryn for initially showing faith in me and giving me the opportunity to work on this project via this studentship, and to my tutors at Balliol College, Professor Frances Kirwan and Dr Keith Hannabuss, for encouraging me to apply in the first place. I have also been fortunate to receive enthusiastic support from our collaborators at Monash University. On his visits during the summers, Professor Alan Bond has felt almost like a fourth supervisor, and working alongside

him with access to his wealth of knowledge of the field has been enlightening and highly enjoyable. In addition, Dr Alexandr Simonov has shown great forbearance working together with me as well optimistic enthusiasm, and I am grateful for his support on the experimental side of the project.

Financially, my work has been possible due to a studentship awarded as part of the OCCAM project, funded by King Abdullah University of Science and Technology (KAUST). This grant has allowed me to pursue my research, and as such is gratefully acknowledged.

On a personal level, I have a lot to be grateful for. My parents have never wavered in their belief in me, and have provided me with both financial and significant moral support through difficult times. Even though things were not always easy for her, my sister has also always done her best to encourage me. Thank you to all my family for their ongoing support!

Among my friends and colleagues, thanks goes to my housemates Yi Ming and Alex for putting up with me for one and two years respectively – an unenviable task! I am especially grateful to Mike, Agnese and Kevin. Even though I have been prone to disappear at times, you have always stood by me as friends over the years, which is very much appreciated. Additional thanks, in no particular order, goes to Matt, Thanasis, Feng, James, Marco, Stephen, Alastair, Patricio, Chris, and Damien. A final special mention goes to Akiko for support and encouragement, particularly over the long finishing stretch of this project!

Abstract

A major problem in the quantitative analysis of AC voltammetric data has been the variance in results between laboratories, often resulting from a reliance on "heuristic" methods of parameter estimation that are strongly dependent on the choices of the operator. In this thesis, an automatic method for parameter estimation will be tested in the context of experiments involving electron-transfer processes in solution-phase. It will be shown that this automatic method produces parameter estimates consistent with those from other methods and the literature in the case of the ferri-/ferrocyanide couple, and is able to explain inconsistency in published values of the rate parameter for the ferrocene/ferrocenium couple. When a coupled homogeneous reaction is considered in a theoretical study, parameter recovery is achieved with a higher degree of accuracy when simulated data resulting from a high frequency AC voltammetry waveform are used.

When surface-confined reactions are considered, heterogeneity in the rate constant and formal potential make parameter estimation more challenging. In the final study, a method for incorporating these "dispersion" effects into voltammetric simulations is presented, and for the first time, a quantitive theoretical study of the impact of dispersion on measured current is undertaken.

Contents

List of Figures

Chapter 1

Introduction

Voltammetry is a technique of electrochemistry used for studying electrochemical reactions, which are chemical reactions which involve the transfer of electrons. Since electron transfer reactions feature in many highly important processes in, for example, biology and industry, the development and use of tools such as voltammetry is required if we are to further our understanding.

In this introductory chapter we will briefly discuss the background of the field of voltammetry, and describe some of the problems currently being tackled by researchers. We will introduce the main mathematical model that will be used in this thesis, and also some of the mathematical tools which will be employed during the course of our investigations. Finally, we will give a brief summary of the overall content of this work.

1.1 Motivation and background

Chemical reactions involving electron transfer form an integral part of many systems that feature at the forefront of technological development today. One important example is the development of batteries and fuel cells. With a growing emphasis being placed upon the generation of renewable energy, for example solar and wind power, the non-constant supply and demand of electricity requires the development of efficient methods of electrical charge storage. Researchers are also attempting to develop alternative fuel cells, for example using the biological catalysts called hydrogenases in platinum-free H_2/O_2 fuel cells [102]. Another example is found in organic light emitting diodes, or OLEDs. An OLED consists of an organic compound which emits light in response to electric currents, sandwiched between two electrodes. These have been finding significant use in display technologies such as televisions and mobile phone screens as an alternative to LCD (liquid crystal display) or plasma technologies due to their increased brightness and superior power efficiency. Systematic studies of these electrochemical processes may lead to improvements in performance of these devices, as the reactions involving the organic compounds which are used become better understood. Yet more examples of technologies or processes where electron transfer reactions are of fundamental importance are some biosensors, where a biological component might be attached to an electrode surface and used to measure a current resulting from an electron transfer reaction involving the target molecule, or the production via electrolysis of raw materials such as aluminium or chlorine. In all of the above examples, further insight into the underlying reactions, and the understanding required to bring about advances, can be gained by using an electroanalytical technique, such as voltammetry, to investigate key system parameters such as rates of reactions.

Voltammetry, as a class of techniques, involves measuring the current resulting

from applying a controlled potential across an electrochemical cell. Numerous forms of this applied potential have been proposed and used, but the most common has been linear sweep voltammetry, which we will refer to as "DC voltammetry", or the closely related cyclic DC voltammetry. This technique involves a potential that varies linearly with time and, in the case of the cyclic variant, reverses at a chosen "switching potential" to return to its initial value. DC voltammetry has been in use as an investigative technique for over 70 years, with key contributions to the initial development of its theory coming from, among others, Randles [83], Sevcick [91], Delahay [32], Matsuda and Ayabe [66], and early work by Nicholson [75, 76]. As the DC technique is still widely used to this day, theoretical understanding has become very advanced and, in addition to various empirical tools for interpreting the resulting current-potential curves based on features such as peak height and position, a wide array of commercial software exists for aiding with experiment-theory comparisons, for example [1,2,86]. While good qualitative assessment of results is often obtained using DC voltammetry, this often requires a series of experiments at different scan-rates, i.e. rates of variation of potential with time, and the DC method also sometimes displays an insufficiently high power of discrimination for complex mechanisms.

An alternative technique, pioneered by the work of Smith [94], involves superimposing one or more rapidly oscillating perturbations on top of the underlying DC linear ramp potential. This class of method, referred to as "AC voltammetry" [18], seems intuitively more sensitive, as the reaction under investigation is tested not only on the timescale of the DC linear sweep, but also on the much faster timescale of the AC perturbation. A drawback for the widespread adoption of AC voltammetry when compared with DC voltammetry has been the increased complexity of solving the underlying mathematical model to allow experiment-theory comparisons to be undertaken. In some special cases, the linearly varying poten-

tial of the DC technique allows the equations of the mathematical model of a DC voltammetry experiment to be solved analytically using techniques such as Laplace transforms [14,85], but for AC voltammetry, the availability of analytical solutions is even more limited [41]. Instead, numerical solution algorithms are required and, until relatively recently, these were too computationally demanding to allow the method to be used in routine practice. In more recent times, however, collaborative work between Monash University and the University of Oxford [38,40,92], among others, has lead to the development of tools for the simulation of AC voltammetric experiments which have been applied with some success (e.g. [46,58]).

One of the major problems facing any experimentalist in voltammetry is that of how to estimate the parameters of the reaction they are investigating using experiment-theory comparisons. While some efforts have been made in the fields of both DC and AC voltammetry to produce automated methods of parameter estimation [3], these often still require input from an operator in order to function appropriately. Far more common, however, is for an operator to compare the results of an experiment with theoretical predictions, and adjust the parameters of the model according to their experience until they judge that the theoretical prediction and experiment match sufficiently well. This inherent dependence on operator experience is a problem and, among other things, leads to lack of reproducibility, or lack of consistency between results published on what appears to be the same experiment between different laboratories. An over-arching goal in the field should therefore be to produce an algorithm capable of accurately estimating these reaction parameters without any input from an operator, and this goal is the central theme of this thesis.

1.2 Mathematical modelling of electrochemistry in the solution phase

In this section we will follow a standard derivation of the mathematical model for voltammetry applied to a reaction happening in solution, as can be found in [11], for example. A general reaction involving the transfer of a single electron can be represented by the equation

$$Red \underset{k_{red}}{\overset{k_{ox}}{\rightleftharpoons}} Ox + e^{-}, \tag{1.1}$$

where k_{ox} and k_{red} are the rates of the oxidation and reduction reactions, respectively. We wish to write down an equation relating the current measured as a function of the potential applied to the system. Current flows as electrons are transferred at the electrode surface between the electrode and the electroactive species.

A standard three-electrode experimental setup is shown in the diagram in Figure 1.1. The half-cell reaction of interest, represented by Equation (1.1), takes place at the working electrode. The other half-cell reaction takes place at the auxiliary electrode, which can sometimes be partitioned off from the working electrode so that reaction products there cannot interfere with the species involved in the reaction at the working electrode. An electrochemical cell involving only these working and auxiliary electrodes is a two-electrode cell, and can be used for voltammetry. However, the use of a two-electrode cell can result in problems with highly resistive solutions, as there can be a significant ohmic drop in the potential, which is measured between the electrodes. In the three-electrode cell, the reference electrode is positioned as near as possible to the working electrode, and the potential of the working electrode is measured against this reference electrode in order to minimise the effect of solution resistance. As the electrodes cannot be placed in exactly the

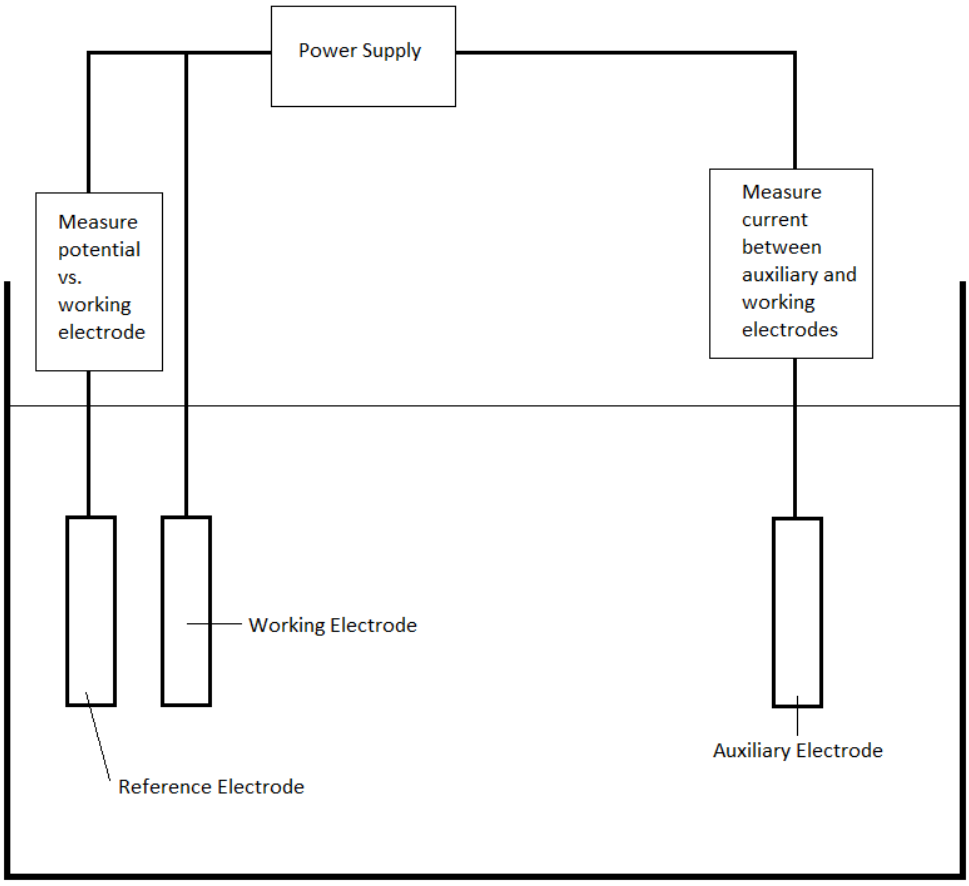

Figure 1.1: A diagram of a standard three-electrode setup for a voltammetric experiment. Current flows between the working and auxiliary electrodes, with the reaction of interest occurring at the working electrode. Potential is measured versus the reference electrode, which is positioned near to the working electrode to minimise the effects of resistance in the solution.

same position, there will still be some effect, which is referred to as uncompensated resistance, and which will be explored further in Section 1.2.1. However, the use of a device for measuring potential which has high impedance results in negligible

current flowing between the reference and working electrodes [11].

The rate of reaction at the electrode surface is governed mainly by the rate of electron transfer and the rate of mass transport of Red and Ox to and from the electrode or, equivalently, their concentrations. Mass transport is composed of contributions from diffusion, migration due to an electric field, and convection. When the solution is stagnant and not agitated by stirring, for example, convective effects can be ignored on the timescale over which experiments take place. In order to counteract the effects of migration, voltammetric experiments are often performed in the presence of an electrolyte, typically at a much higher concentration than the electroactive species the experimenter is interested in. This electrolyte solution will contain ions which are not electroactive, and that, ideally, will not react with either of the species taking part in the electron transfer reaction. These ions offer additional pathways for the electrons to flow through the solution and, importantly, the vastly greater numbers of the ions from the electrolyte solution means that migration effects are negligible in the electroactive species. An additional benefit of using this electrolyte solution is immediately apparent: the improved conductivity of the solution results in lower values of resistance, which is an effect we will return to slightly later.

This leaves diffusion as the remaining contributor to mass transport. Diffusion can be modelled by Fick's law, which gives

$$\frac{\partial c_i}{\partial t} = D_i \nabla^2 c_i, \tag{1.2}$$

where t is time, and c_i are the concentrations and D_i the diffusion coefficients, for $i = Ox, Red$. We will consider only the use of macro-electrodes, which can be considered as planar, so diffusion occurs in only a single direction and Fick's law is reduced to

$$\frac{\partial c_i}{\partial t} = D_i \frac{\partial^2 c_i}{\partial x^2}, \tag{1.3}$$

where x is the space variable with the electrode at $x = 0$.

If we assume we are modelling an oxidation reaction, we have the initial conditions

$$c_{red}(x, 0) = c_\infty, \tag{1.4}$$

$$c_{ox}(x, 0) = 0, \tag{1.5}$$

and the semi-infinite boundary conditions far from the electrode

$$c_{red} \to c_\infty, \tag{1.6}$$

$$c_{ox} \to 0, \quad \text{as} \quad x \to \infty, \quad t > 0. \tag{1.7}$$

At the electrode surface, the fact that every molecule of species *Red* which reacts at the electrode becomes a molecule of species Ox means that the fluxes of *Red* and Ox to and from the electrode must be in balance, so

$$D_{red}\frac{\partial c_{red}}{\partial x} = -D_{ox}\frac{\partial c_{ox}}{\partial x} \quad \text{at} \quad x = 0. \tag{1.8}$$

For the final boundary condition at the electrode surface, we look to the rates of reaction. For a species in solution phase, the reaction rate is often of the form given by the Arrhenius equation

$$k = A' \exp\left[\frac{-E_A}{RT}\right], \tag{1.9}$$

where E_A represents activation energy, A' is a so-called frequency factor, R is the gas constant, and T the absolute temperature. Assuming that the rates of reaction k_{ox} and k_{red} from Equation (1.1) are of Arrhenius-form, then the empirical Butler-Volmer formulation [11] states that

$$k_{ox} = k_0 \exp\left[\frac{(1-\alpha)F}{RT}(E(t) - E^0)\right], \tag{1.10}$$

$$k_{red} = k_0 \exp\left[\frac{-\alpha F}{RT}(E(t) - E^0)\right], \tag{1.11}$$

where F is Faraday's constant, α is a dimensionless constant with $0 \leq \alpha \leq 1$ called the "charge-transfer coefficient", $E(t)$ is the potential, which will be defined later, E^0 is the "formal" potential where by definition $k_{ox} = k_{red}$, and k^0 is the "standard rate constant" defined at E^0 to be the value $k^0 = k_{ox} = k_{red}$.

Furthermore, appealing to the law of mass action applied to Equation (1.1), we have that the rate of conversion of Red to Ox, r_{ox}, which is proportional to an "oxidation" component of the current, I_{ox}, is given by

$$r_{ox} = k_{ox} c_{red} = \frac{I_{ox}}{FS}, \tag{1.12}$$

where S is the surface area of the electrode. Similarly for the conversion of Ox back to Red, we have

$$r_{red} = k_{red} c_{ox} = \frac{I_{red}}{FS}. \tag{1.13}$$

Combining these, the total Faradaic current, I_f, flowing due to electron transfer is given by

$$I_f = I_{ox} - I_{red} = FS\left(k_{ox} c_{red} - k_{red} c_{ox}\right). \tag{1.14}$$

Now substituting the expressions in Equations (1.10) and (1.11) into Equation (1.14) we have

$$\begin{aligned} I_f = \; & FSk_0 \left[c_{red} \exp\left(\frac{(1-\alpha)F}{RT}(E(t) - E^0) \right) \right. \\ & \left. - c_{ox} \exp\left(\frac{-\alpha F}{RT}(E(t) - E^0) \right) \right], \end{aligned} \tag{1.15}$$

for $x = 0$, $t > 0$, which is the Butler-Volmer equation.

Finally, in order to relate the Faradaic current to the concentration gradient at the electrode, we take from the Nernst-Planck equation [11] in the absence of migration and convection effects, that

$$J_{red} = -D_{red} \frac{\partial c_{red}}{\partial x}, \tag{1.16}$$

where J_{red} is the flux of Red, and then at the electrode surface we have the relationship

$$J_{red} = -\frac{I_f}{FS}, \quad \text{at} \quad x = 0, \tag{1.17}$$

which combine to give

$$I_f = FSD_{red}\frac{\partial c_{red}}{\partial x}, \quad x = 0, t > 0. \tag{1.18}$$

It is also worth noting that in the case that $D_{red} = D_{ox}$, Equation (1.8) in combination with the boundary and initial conditions gives

$$c_{red} + c_{ox} = c_{\infty}. \tag{1.19}$$

We can substitute Equation (1.19) into Equation (1.15) and then consider only equations and boundary conditions involving a single species.

1.2.1 Uncompensated resistance and double-layer capacitance

Two further phenomena which contribute significantly to the measured current from a voltammetric experiment are uncompensated resistance and double-layer capacitance.

Uncompensated resistance refers to the resistance that is not removed by the use of a potentiostat. Predominantly, this is the resistance inherent in the solution present between the working and reference electrodes. Although, as mentioned previously, this can be reduced as a side-effect of adding a significant amount of buffering electrolyte, we still expect a drop in potential as predicted by Ohm's law

$$E_{drop} = I_{tot}R_u, \tag{1.20}$$

where I_{tot} is the total current recorded. This then results in the potential effectively seen by the system being

$$E(t) = E_{applied}(t) - E_{drop}(t) = E_{applied}(t) - I_{tot}R_u, \tag{1.21}$$

where $E_{applied}$ denotes the controlled input potential for the voltammetric experiment.

In some potential ranges, electrodes are capable of exhibiting behaviour characteristic of a so-called "ideal polarised electrode". When this happens, charge builds up and the electrode-solution interface acts as a capacitor, governed by the equation

$$\frac{q}{E} = C, \tag{1.22}$$

where q is the charge stored on the capacitor and C the capacitance. This gives rise to a charging current, I_c, given by

$$I_c = \frac{\mathrm{d}q}{\mathrm{d}t} = \frac{\mathrm{d}}{\mathrm{d}t}\left(CE\right), \tag{1.23}$$

and then

$$I_{tot} = I_f + I_c. \tag{1.24}$$

This effect is often referred to as "double-layer capacitance", as a so-called electrical double-layer develops, in which there is a local excess of cations near the electrode, and the term C is often written as C_{dl}. C_{dl} can be modelled as being either a constant, or as being a function dependent on the potential, E, as we will see in Chapter 3.

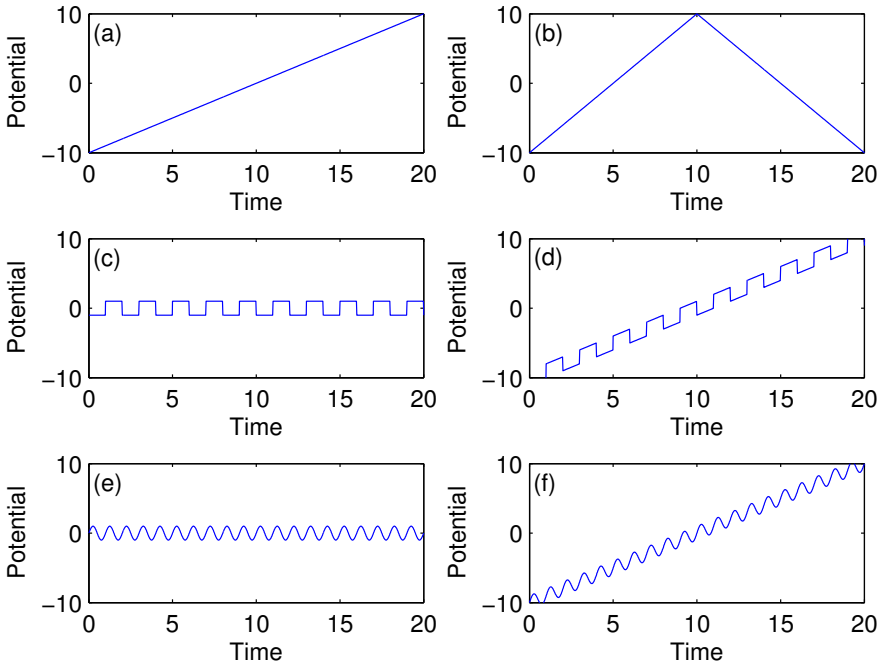

Figure 1.2: Some potentials used in voltammetry, corresponding to: (a) DC linear sweep voltammetry (E_{DC}), (b) DC cyclic voltammetry (E_{CDC}), (c) square wave voltammetry (E_{SQ}), (d) square wave voltammetry on top of a linear ramp ($E_{DC} + E_{SQ}$), (e) AC sine wave voltammetry (E_{AC}), (f) AC voltammetry on top of a linear ramp ($E_{DC} + E_{AC}$).

1.2.2 Voltammetry potentials

The remaining variable in our model of voltammetry is the form used for the applied potential. Some variations which have been used are

$$E_{DC}(t) = E_{start} + \nu t, \tag{1.25}$$

$$E_{CDC}(t) = \min\left(E_{start} + \nu t, E_{start} + \nu(t_{max} - t)\right), \tag{1.26}$$

$$E_{SQ}(t) = \Delta E(-1)^{[\frac{\omega t}{\pi}]}, \tag{1.27}$$

$$E_{AC}(t) = \Delta E \sin(\omega t), \tag{1.28}$$

where E_{DC} and E_{CDC} are linear sweep and cyclic DC potentials, E_{SQ} is a rarely-used square-wave oscillation with the square brackets in Equation (1.27) denoting the integer part of the frequency term, and E_{AC} is the standard AC voltammetry sine wave perturbation. In all of the above forms, ν represents the scan rate (units V s^{-1}), and ΔE and ω the amplitude and frequency of an AC perturbation, respectively. An overall input potential could then be a combination of the above, with the most common being DC cyclic voltammetry represented simply by

$$E_{applied}(t) = E_{CDC}(t), \tag{1.29}$$

and (cyclic) AC voltammetry usually having the form

$$E_{applied}(t) = E_{CDC}(t) + E_{AC}(t). \tag{1.30}$$

Figure 1.2 shows the potentials of Equations (1.25)–(1.28) in panels (a)–(c) and (e), along with combinations of E_{DC} with E_{SQ} and E_{AC} in panels (d) and (f).

An example of a voltammogram, taken from an experiment featured in Chapter 2 that uses cyclic AC voltammetry, is shown in Figure 1.3. We see two time intervals during which there is an increased amount of current being measured. These peaks, corresponding to increased Faradaic current resulting from electron transfer, occur in response to the potential becoming close to $E(t) = E^0$, as we might expect from Equation (1.15). One peak occurrs on each of the forwards and backwards sections of the underlying cyclic potential ramp. An experimentalist would note the positions and magnitudes of these peak currents in order to assist with parameter estimation, as well as other features such as the magnitude of the current outside of this "Faradaic" region, which provides a means of estimating the charging or background current, I_c.

As has been discussed previously, while it may not immediately be apparent what differences there are between the AC and DC methods, the addition of an extra

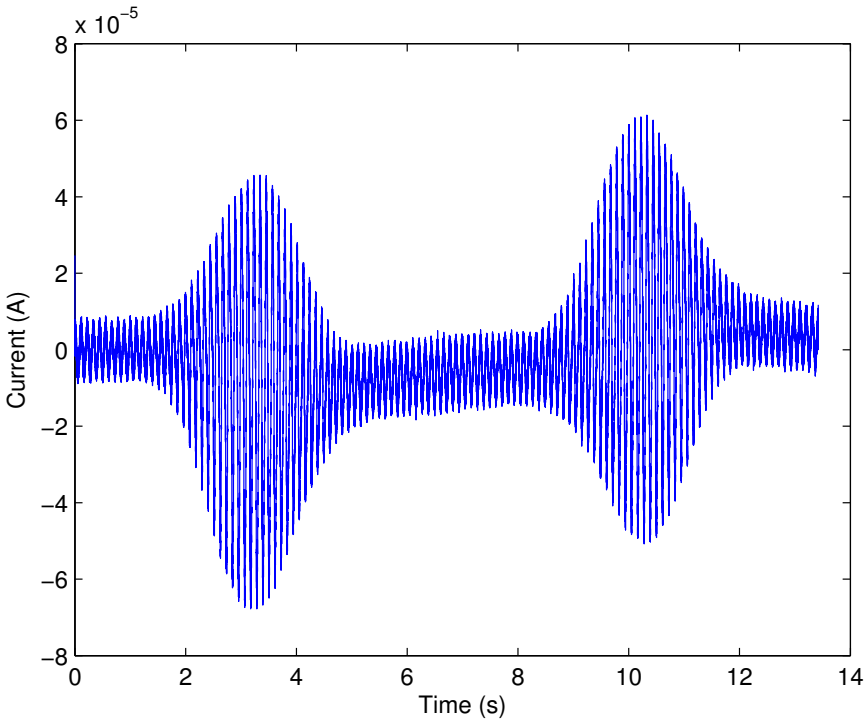

Figure 1.3: An example of a voltammogram taken from a cyclic AC voltammetric experiment using a sine wave with a frequency of 9 Hz and an amplitude of 80 mV, and an underlying cyclic potential with scan rate 89.4 mV s^{-1}. The reaction mechanism was a single-electron transfer, as described in Section 1.2.

timescale controlled by the frequency of the AC perturbation allows powerful and intuitive tools to be applied to the analysis of voltammetric data, an example of which we will see in the following section.

1.3 Use of the Fourier transform

One of the most valuable tools for analysing data from AC voltammetric experiments is the Fourier transform. With the addition of an AC perturbation on top

of the DC linear ramp giving a second timescale of variation of the applied potential, the current response in the time-domain is visually dominated by a rapidly oscillating portion that is due to the AC perturbation. At the same time, the very nature of this AC signal suggests that there are components of the current response which result from this perturbation at both its base and higher harmonic frequencies.

Theory-experiment comparisons are often performed using an heuristic method, involving an operator adjusting certain parameters of the simulated model until it appears to predict results that best match the experimental data, an example of which we will see in Chapter 2. This is not only difficult in the cluttered time-domain, but also splitting up the signal into harmonic components allows for a much more intuitive approach to this problem as different harmonics are more sensitive to variations in certain parameters, creating an illusion of there being more information and allowing an experienced operator to gain deeper understanding of the underlying mechanisms. This approach will be discussed in more detail in Chapter 2. The tool by which this division of the signal is implemented is the Fourier transform and its inverse, and it has been used to considerable success in previous studies by this collaboration [61, 92, 97].

In practical terms, as we are dealing with a discrete time-series of measurements, we will use the discrete Fourier transform. This is defined on a sequence $x(j)$, $j = 1, ..., N$, as

$$X_k = \sum_{j=1}^{N} x_j \exp\left(\frac{-2\pi i(j-1)(k-1)}{N}\right), \quad k = 1, ..., N, \tag{1.31}$$

and implemented in Matlab according to the Cooley-Tukey algorithm as `fft`. The corresponding inverse Fourier transform, implemented as `ifft`, is calculated ac-

cording to

$$x_j = \frac{1}{N}\sum_{k=1}^{N} X_k \exp\left(\frac{2\pi i(j-1)(k-1)}{N}\right), \quad j = 1, ..., N. \tag{1.32}$$

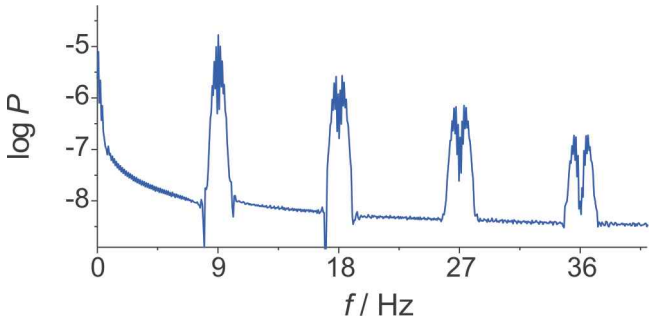

Figure 1.4: An example of a power spectrum resulting from the AC voltammetric experiment using a sine wave frequency of 9 Hz that was featured in Figure 1.3. The contributions from the fundamental harmonic at 9 Hz, and the 2nd, 3rd and 4th harmonics, as well as the contribution from the DC component in the first few entries, are clearly visible.

The Fourier transform of an AC voltammetry current time-series contains contributions from the DC component, and then the base frequency of the oscillation, f, and its harmonics at nf, for $n = 1, 2, 3, ...$ If we define the power, P, by

$$P_j = \sqrt{\mathrm{Re}(X_j)^2 + \mathrm{Im}(X_j)^2}, \quad j = 1, ..., N, \tag{1.33}$$

then we can plot P or $\log P$ against the frequency, and these harmonics are easily identified. An example of this, taken from the same experiment from Chapter 2 as was used for Figure 1.3, is shown in Figure 1.4.

In order to isolate a harmonic, we take the Fourier-transformed data and identify the entries corresponding to the contribution from that harmonic. It is essential to note that each harmonic contains contributions at both positive frequencies around X_k, with $k \leq N/2$, and the corresponding negative frequency around

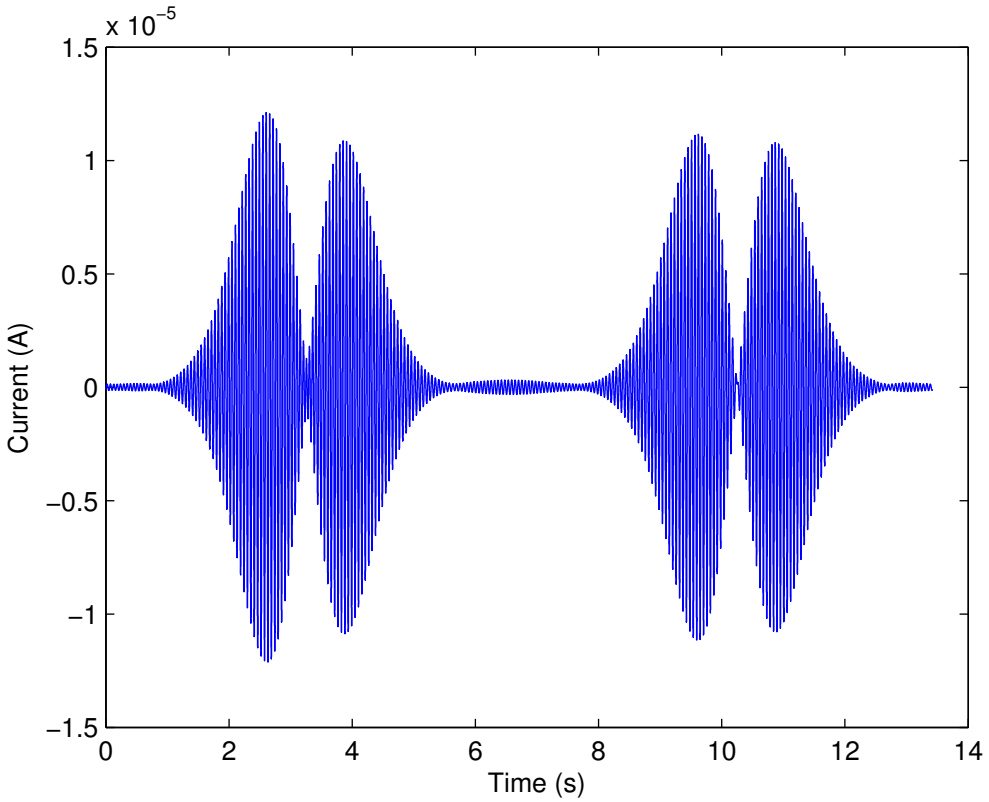

Figure 1.5: An example of the 2nd harmonic isolated from the AC voltammetric experiment featured in Figures 1.3 and 1.4 using the process detailed in the text.

X_{N-k}, which is the complex conjugate of X_k. After identifying both of these contributions, all other entries in the Fourier transform are set to zero, and the inverse Fourier transform is applied. Since the inverse Fourier transform may now produce complex numbers, we take the absolute value, and preserve the sign of the real part, so our recovered harmonic time-series y, say, is given by

$$y_j = \text{sign}(\text{Re}(x_j))|x_j|, \quad j = 1, ..., N, \tag{1.34}$$

where x_j represent the results of the inverse Fourier transform, obtained according to Equation (1.32). An example of the result of this process, applied to the AC voltammetric experiment whose power spectrum was shown in Figure 1.4 and used

to isolate its 2nd harmonic, is shown in Figure 1.5. Each harmonic has a distinct shape and sensitivity to combinations of model parameters, and an experienced operator can use knowledge of this to derive information about the electron transfer process that is being investigated.

Using the Fourier transform in this way has some advantages and disadvantages, and these will be discussed further in Chapter 2.

1.4 The inverse problem

As was mentioned in the opening remarks to this chapter, one of the main goals in the research field of voltammetry is to provide a reliable, operator-independent method of estimating parameters of an electrochemical reaction using an automated method of experiment-theory comparison. Using the techniques of Fourier transformation of AC voltammetric data and simplex optimisation over the harmonics, some efforts have already been made on this front by our collaborators at Monash using the Nimrod software [3]. This method, as we will discuss in Chapter 2, is not fully operator-independent, however, due to decisions required for the circumvention of numerical artefacts introduced during the isolation of harmonics. In this section, we will quickly outline a standard derivation of a least-squares optimisation, which will form the basis of a time-domain or "global" optimisation method. In subsequent chapters, we will then apply this algorithm for parameter estimation to data taken from AC voltammetric experiments and simulations. Although we use a probability theory approach, it should be noted that this is not required or relevant to the rest of this thesis, and is used to link in with ideas introduced in the future work section in Chapter 6.

To formalise the inverse problem for the algorithmic approach, we will adopt a Bayesian approach [93]. Let y be a vector of unknown parameters, in our case the experimental unknowns E^0, k^0, α, R_u and C_{dl}, let I be a time-series of measured current points, and let G be a nonlinear function such that

$$I = G(y). \tag{1.35}$$

Using the notation of π to represent a probability density function, we wish to know the parameters y for which the posterior probability function $\pi(y|I)$ is maximised. From Bayes' theorem we have

$$\pi(y|I) = \frac{\pi(I|y)\pi(y)}{\pi(I)}, \tag{1.36}$$

and we know $\pi(I)$ is constant, so we need to determine expressions for $\pi(I|y)$ and $\pi(y)$.

For the prior distribution, $\pi(y)$, we assume the elements of y are independent, and then the principle of maximum entropy suggests that for each element, y_i, the probability density function is

$$\pi(y_i) = \frac{1}{\overline{y_i}} \exp\left[-\frac{y_i}{\overline{y_i}}\right], \tag{1.37}$$

where $\overline{y_i}$ is the prior estimate of y_i. We can then write

$$\pi(y) = \prod_{i=1}^{n} \pi(y_i). \tag{1.38}$$

In order to determine the likelihood function, $\pi(I|y)$, we assume that our measured current values, I, are affected by measurement errors, which are normally distributed with zero mean and standard deviation σ. Then

$$\pi(I|y) = c \exp\left[-\frac{1}{2\sigma^2} \sum_{i=1}^{n} ((I_i - G_i(y))^2)\right], \tag{1.39}$$

where c is a suitable normalisation constant. Thus our posterior function is given by

$$\pi(y|I) = c \exp\left[-\frac{1}{2\sigma^2}\sum_{i=1}^{n}((I_i - G_i(y))^2) - \sum_{i=1}^{n}\left[\frac{y_i}{\overline{y_i}}\right]\right]. \tag{1.40}$$

Taking logarithms and making the further assumption that no prior estimates for y are available, making $\pi(y)$ constant, we simplify our optimisation problem to the minimisation of

$$L_{Glo} = \sum_{i=1}^{n}\left[(I_i - G_i(y))^2\right], \tag{1.41}$$

where L_{Glo} will denote the objective function for this "global" or time-domain method.

While the least squares approach is hardly novel, the idea of bypassing the intuitively appealing frequency domain approach of the heuristic method and Nimrod software and simply acquiring the optimal match between simulation and experiment in the time domain has not been adequately explored. In principle, all information available via Fourier transformation and subsequent isolation of the harmonics is available to time-domain analysis as well. In the course of this thesis, we will investigate the viability of this time-domain approach, as well as consider some of the advantages and disadvantages it has when compared with the other methods of parameter estimation.

1.5 Overview of thesis

In the course of this chapter, we have provided some motivation for the study of voltammetry as a technique for increasing understanding of electrochemical processes. We then worked through a standard formulation of a mathematical model describing electron transfer reactions at a solution-electrode surface interface, and

described some of the different forms of voltammetry that can be used to investigate such electron transfer reactions. We discussed the way in which the Fourier transform is used as an essential part of analysis of AC voltammetric data, and finally introduced a possible method for attempting to automate the process of parameter estimation from experimental data, which is one of the major goals in this field.

In Chapter 2, we will take the example of the simplest theoretical electrode process, and demonstrate a numerical solution of our mathematical model from this chapter. Following this, we will use experimental data provided by our collaborators, from experiments on the reduction of ferricyanide, as a means of introducing the different methods of parameter estimation currently in use, and comparing their advantages and disadvantages with our proposed fully-automated method.

In Chapter 3, we will consider another single-electron transfer process, namely the oxidation of ferrocene. Again, with significant experimental data to support our study, we will investigate the dangers of using inappropriate models, and in particular, issues of over- and under-parameterisation. Making use of mathematical techniques such as bootstrapping, we will be able to shed some light on the widely-varying values of the rate constant, k^0, reported for this process over many years by different laboratories.

In Chapter 4, we will look at the case study of an EC reaction mechanism consisting of an electron transfer reaction coupled with a chemical reaction involving one of the electroactive species. Focusing on this simple example, we will perform a theoretical study under conditions including simulated noise representing instrumentation measurement errors. Again making use of the bootstrapping technique, we will demonstrate some of the difficulties encountered in estimating the parameters of more complex reaction systems, including some comparison of the

relative performance of the DC and AC voltammetric techniques.

In Chapter 5, we will shift our focus to reactions involving molecules confined to the electrode surface. We will discuss the lack of agreement often found in the literature between theoretical predictions and experimental data, and introduce the phenomenon of dispersion, which is often cited as a possible reason for this. After referencing recent studies as a motivation for the inclusion of dispersion in a mathematical model of surface-confined electron-transfer reactions, we will provide two possible methods for modelling these processes, and detemine their equivalence under typical experimental conditions. One of these models will then be used to investigate the effects of kinetic and thermodynamic dispersion in a purely theoretical study, considering both DC and AC voltammetry, and we will comment on whether the inclusion of dispersion is sufficient to account for the discrepancies between experimental results and current theory.

Finally, in Chapter 6 we will summarise our results, and use what we have learned in the course of this research to motivate areas of further study.

1.6 Collaboration

The AC voltammetry project is highly inter-disciplinary, employing researchers with backgrounds in electrochemistry, mathematics, computer science and engineering. There is a large scope for collaboration, and we are fortunate to have the support of the Bond Electrochemistry Research Group at Monash University, Australia, who are among the leading research teams in the world in the field of voltammetry. Their input on the chemistry side of the project has been invaluable, and their contribution to this thesis has come particularly in the form of the exper-

iments performed which are analysed in Chapters 2 and 3, and all Nimrod software calculations in those chapters, run using the parallel computing grid resources at Monash.

Chapter 2

An introductory example

In this chapter, we will consider an introductory example based on one of the "simplest" experimental systems. We will use this as a test case to illustrate the solution of the forwards problem of simulation, and then apply our inverse problem algorithm, firstly in simulation and then to supporting experimental data in an in-depth study. We will compare our method to existing techniques, and discuss the relative advantages and disadvantages of each. The work on which this chapter is based has appeared in [71].

2.1 Background

The simplest reaction in electrochemistry is a single-electron transfer according to

$$A \rightleftharpoons B + e^{-}, \tag{2.1}$$

where A and B are species in solution, and electron transfer takes place at the electrode surface. By virtue of being the simplest reaction mechanism, this is

a good initial system on which to test both our model and simulation method for the forwards problem, and also our method for parameter estimation via the time-domain inverse problem algorithm.

After testing our methods in a theoretical setting, we will proceed to use them in the context of an experimental example, namely the quasi-reversible reduction of ferricyanide to ferrocyanide

$$[\mathrm{Fe(CN)}_6]^{3-} + e^- \rightleftharpoons [\mathrm{Fe(CN)}_6]^{4-}. \tag{2.2}$$

This system has been widely studied previously [9, 13, 15, 29, 47, 52, 70, 78], and while some variation in the parameter values reported exists, an electrochemist would say with some confidence that they would expect those parameter values to lie within a relatively narrow range. As such, this system should prove to be a suitable test case for the inverse problem, as we have some preconceived idea of what the reported parameter values should be. We will show that even in the non-ideal, imperfect world of genuine experimental data, where considerations such as noise due to measurement error must also be taken into account, our parameter estimation algorithm performs very well, provided sufficient care is taken to make the simulation model as accurate as it can be.

We will compare the results of three different methods of parameter recovery: our proposed time-domain method, a commonly-used heuristic approach, and a semi-heuristic optimisation performed in the frequency domain. These experiments and comparisons will be performed as part of our collaboration with the Bond electrochemistry group at Monash University, Australia, and this joint work between our two laboratories will serve to highlight some of the advantages and disadvantages of each method.

In addition to providing us with suitable testing grounds for our methods, the use

of ten repeated experiments performed under as close to identical conditions as could be managed will allow us not only to comment on the reproducibility and reliability of our results, but also to contribute to the scientific discussion of this pathologically variable reaction system.

2.2 Methods

Before we begin to attempt analysis of experimental data, we must first solve numerically the equations of our mathematical model to produce simulated data for comparison, and establish that our parameter estimation algorithm works on at least these simulated data when noise is added artifically to mimic the effect of measurement error.

2.2.1 The forwards problem: solution scheme

In Chapter 1, we have explained the theory behind the mathematical model of solution-phase electron transfer, along with the technique of voltammetry. Here, we will start from this model, and then demonstrate an already-established numerical solution method (see, for example, [38, 92]).

From Section 1.2 in Chapter 1, the system of equations modelling single-electron transfer in solution involving species with equal diffusion coefficients is given below. The concentration of the reduced species, c_{red}, evolves according to

$$\frac{\partial c_{red}}{\partial t} = D\frac{\partial^2 c_{red}}{\partial x^2}, \quad x > 0, t > 0, \tag{2.3}$$

subject to the boundary conditions

$$c_{red}(x,0) = c_\infty, \quad x \geq 0, \tag{2.4}$$

$$c_{red} \to c_\infty \quad \text{as} \quad x \to \infty, \quad t > 0, \tag{2.5}$$

and at $x = 0$, for $t > 0$,

$$\begin{aligned} I_f = \; & FSk_0 \left[c_{red} \exp\left(\frac{(1-\alpha)F}{RT}(E(t) - E^0) \right) \right. \\ & \left. -(c_\infty - c_{red}) \exp\left(\frac{-\alpha F}{RT}(E(t) - E^0) \right) \right], \end{aligned} \tag{2.6}$$

and

$$I_f = FSD\frac{\partial c_{red}}{\partial x}. \tag{2.7}$$

Furthermore, we have

$$E(t) = E_{applied}(t) - I_{tot}R_u, \tag{2.8}$$

$$E_{applied}(t) = E_{start} + \nu t + \Delta E \sin(\omega t), \tag{2.9}$$

$$I_{tot} = I_c + I_f, \tag{2.10}$$

$$I_c = C_{dl}\frac{dE}{dt}. \tag{2.11}$$

For our next step, we non-dimensionalise the model. Scaling $x \sim l$, $t \sim t_0/\nu$ and $c \sim c_\infty$, we immediately see from (2.3) that choosing $l^2 = Dt_0/\nu$ gives

$$\frac{\partial u}{\partial t^*} = \frac{\partial^2 u}{\partial x^{*2}}, \tag{2.12}$$

where u, x^* and t^* are the dimensionless concentration, space and time variables, and we also have the boundary and initial conditions

$$\begin{aligned} u(x^*, 0) = 1 \quad & \text{for} \quad x^* \geq 0, \\ u \to 1 \quad & \text{as} \quad x^* \to \infty, \quad t > 0. \end{aligned} \tag{2.13}$$

We must also have $E \sim RT/F$ from the exponential term in (2.6), and hence $t_0 = RT/F$ as well, so $t = t^* RT/F\nu$, from (2.9). Writing $E_{start} = E^*_{start} RT/F$, $\Delta E = \Delta E^* RT/F$ and $\Omega = \omega RT/F\nu$ gives

$$E^*_{applied}(t^*) = E^*_{start} + t^* + \Delta E^* \sin(\Omega t^*), \tag{2.14}$$

provided we choose the values of E_{start} and Ω such that $\Omega E_{start} F/RT = 2n\pi$, which can be done as these are at our discretion.

We can now write $k^*_0 = k_0(RT/FD\nu)^{1/2}$ and $l = (DRT/F\nu)^{1/2}$, and then $I_{tot} \sim FAc_\infty(DF\nu/RT)^{1/2}$. Finally, we have the relationships

$$\begin{aligned} R^*_u &= \frac{F^2 A c_\infty}{RT}\left[\frac{DF\nu}{RT}\right]^{1/2} R_u, \\ C^*_{dl} &= \frac{\nu}{FAc_\infty}\left[\frac{RT}{DF\nu}\right]^{1/2} C_{dl}. \end{aligned} \tag{2.15}$$

We can then complete the model with

$$I^*_c = C^*_{dl}\frac{dE^*}{dt^*}, \tag{2.16}$$

$$I^*_{tot} = I^*_f + I^*_c, \tag{2.17}$$

$$E^*(t^*) = E^*_{applied}(t^*) - I^*_{tot} R^*_u, \tag{2.18}$$

$$I^*_f = \left[\frac{\partial u}{\partial x^*}\right]_{x^*=0}, \tag{2.19}$$

$$\begin{aligned} I^*_f = k^*_0 \big[& u\exp((1-\alpha)(E^*(t^*) - E^{0*})) \\ & -(1-u)\exp(-\alpha(E^*(t^*) - E^{0*}))\big] \quad \text{at} \quad x^* = 0. \end{aligned} \tag{2.20}$$

From here on, we will drop the asterisks that were used to mark dimensionless variables, and assume that all are of that kind.

We will now develop a method to obtain a numerical approximation to the solution using the finite difference method for partial differential equations [72]. Firstly, we

combine Equations (2.14), (2.16)–(2.18) and (2.20) to give at the electrode surface, $x = 0$, $t > 0$

$$\begin{aligned} & I_{tot} - C_{dl}\left[1 + \Delta E\Omega\cos(\Omega t) - R_u\frac{dI_{tot}}{dt}\right] = \\ & k_0\left[u\exp\left[(1-\alpha)(E_{applied}(t) - I_{tot}R_u - E^0)\right] - \right. \\ & \left.(1-u)\exp\left[-\alpha(E_{applied}(t) - I_{tot}R_u - E^0)\right]\right]. \end{aligned} \tag{2.21}$$

We discretise space and time with a uniform mesh in each variable, so $x_j = j\Delta x$ and $t^m = m\Delta t$. As we are dealing with a semi-infinite spatial domain, we must choose a value of x_{max} sufficiently large that behaviour there approximates behaviour at "infinity", and it has been shown that in terms of dimensionless variables, choosing $x_{max} = 6$ is sufficient to fulfill this criterion over the timescale of interest [38]. Then, using the notation U_j^m to represent the numerical approximation to $u(x = j\Delta x, t = m\Delta t)$, $\mu = \Delta t/(\Delta x)^2$, we employ a simple Theta-method [72] on the diffusion equation:

$$\begin{aligned} & -\theta\mu U_{j-1}^{m+1} + (1+2\theta\mu)U_j^{m+1} - \theta\mu U_{j+1}^{m+1} = \\ & (1-\theta)\mu U_{j-1}^m + (1-2(1-\theta)\mu)U_j^m + (1-\theta)\mu U_{j+1}^m, \end{aligned} \tag{2.22}$$

for $1 \leq j \leq N-1$, $m \geq 0$.

This is an equation of the form

$$-a_j U_{j-1}^{m+1} + b_j U_j^{m+1} - c_j U_{j+1}^{m+1} = d_j^{m+1}, \tag{2.23}$$

where the right-hand side is in terms of known quantities, computed at the previous timestep. The Thomas algorithm [72] directly reduces this to

$$U_j^{m+1} - e_j U_{j-1}^{m+1} = f_j^{m+1}, \tag{2.24}$$

with

$$e_j = \frac{a_j}{b_j - c_j e_{j+1}},$$
$$f_j^{m+1} = \frac{f_{j+1}^{m+1} c_j + d_j^{m+1}}{b_j - c_j e_{j+1}}. \tag{2.25}$$

The boundary condition $U_N^{m+1} = 1$ then gives us $e_N = 0$ and $f_N^{m+1} = 1$, so the e_j and f_j^{m+1} can easily be determined for $j = N-1, ..., 1$ using (2.25). Discretising (2.19) to give

$$\Delta x I_f^{m+1} = U_1^{m+1} - U_0^{m+1}, \tag{2.26}$$

U_0^{m+1} can be found in terms of I_f using (2.24) and (2.26):

$$U_0^{m+1} = \frac{\Delta x I_f^{m+1} - f_1^{m+1}}{e_1 - 1}. \tag{2.27}$$

Substitution back into (2.21), and using (2.14) and (2.16)–(2.18) to write I_f in terms of I_{tot}, gives us an equation of the form

$$g(I_{tot}^{m+1}) = 0, \tag{2.28}$$

for some known, but algebraically complicated, nonlinear function g. This equation can then be solved via a zero-finding routine such as Brent's method [22], which is implemented in Matlab [100] as the function `fzero`.

2.2.2 The forwards problem: simulations

The results of varying parameters in forwards simulations of AC voltammetry have been extensively documented by previous authors [92, 95]. We have verified all of these, but rather than presenting the entire set, we will show one example which will prove relevant throughout the course of this thesis.

In our simulations, a typical spatial step of $\Delta x = 0.005$ (dimensionless) has been used, along with 2^{13} or 2^{14} equally spaced time steps of length determined by the

potential limits and scan rate of the experiment. Both of these values have been tested, and are sufficiently small that the numerical solution remained unchanged upon further reduction in mesh size. A value of $\theta = 0.5$ was used, being the most accurate in time [72].

Our simulations were run using computer codes that we wrote initially in Matlab, and then later in C++ for anything involving parameter optimisation. Unless stated otherwise, these codes were run on a desktop PC with an AMD Phenom II X4 925 processor and 4 GB RAM. In each language the simulation of a single-electron transfer reaction, using the numerical solution scheme described in Section 2.2.1, requires under one second of computation time on this PC.

To orientate the reader, we include two figures showing the results of simulations using our numerical solution scheme, and displaying some of the features of the underlying electron-transfer process. Figure 2.1 shows the case of simulation of cyclic DC voltammetry. The figure can be divided into two parts, corresponding to the forwards and reverse sweeps of the cyclic linear ramp introduced in Chapter 1. Considering the forwards sweep, we see the standard shape of the current response in linear sweep voltammetry. Initially, the current grows exponentially as $E(t)$ approaches E^0 as A is oxidised more rapidly to B at the electrode, as is predicted by the Butler-Volmer equation, given earlier in Equation (2.6). At some point in time, the limiting factor controlling the rate of reaction is no longer the rate of electron transfer, however, but instead the rate of mass transport by which species A can be replaced at the electrode. This limitation results in the current reaching a peak and then decaying, as the solution around the electrode is predominantly composed of species B. Similar features are seen on the reverse sweep of the potential.

Figure 2.2 shows a simulation of cyclic AC voltammetry, this time also including

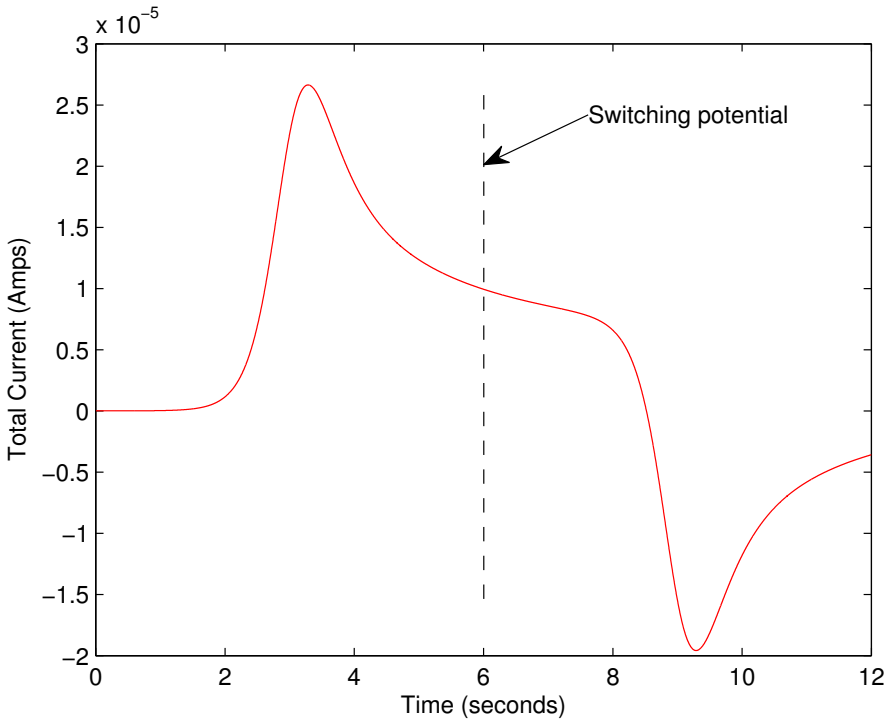

Figure 2.1: An example of the current resulting from the simulation of a cyclic DC voltammetric experiment, with the time at which the switching potential is reached indicated. Parameters used were $E_{start} = -0.3$ V, $E_{max} = 0.3$ V, $\nu = 0.1$ V s^{-1}, $D = 2.5 \times 10^{-5}$ cm^2 s^{-1}, $S = 0.071$ cm^2, $c_\infty = 1$ mM, $T = 296$ K, $E^0 = 0$ V, $k^0 = 10^3$ cm s^{-1}, $\alpha = 0.5$, $R_u = 0\ \Omega$, $C_{dl} = 0\ \mu$F cm^{-2}.

the effects of uncompensated resistance and double-layer capacitance. We see similar features as $E(t)$ approaches E^0, as we see exponential growth in the envelope of the current, before decay as a mass-transport-limited regime is reached. We also see that when $E(t) \approx E^0$, the almost equal rates of the forwards and backwards reactions given by the Butler-Volmer formulation of Chapter 1, seen in Equations (1.10) and (1.11), result in rapid oscillations between positive and negative currents of near-equal magnitude due to the AC perturbation. The other interesting thing to note is the constant oscillation outside of the Faradaic areas, which is the

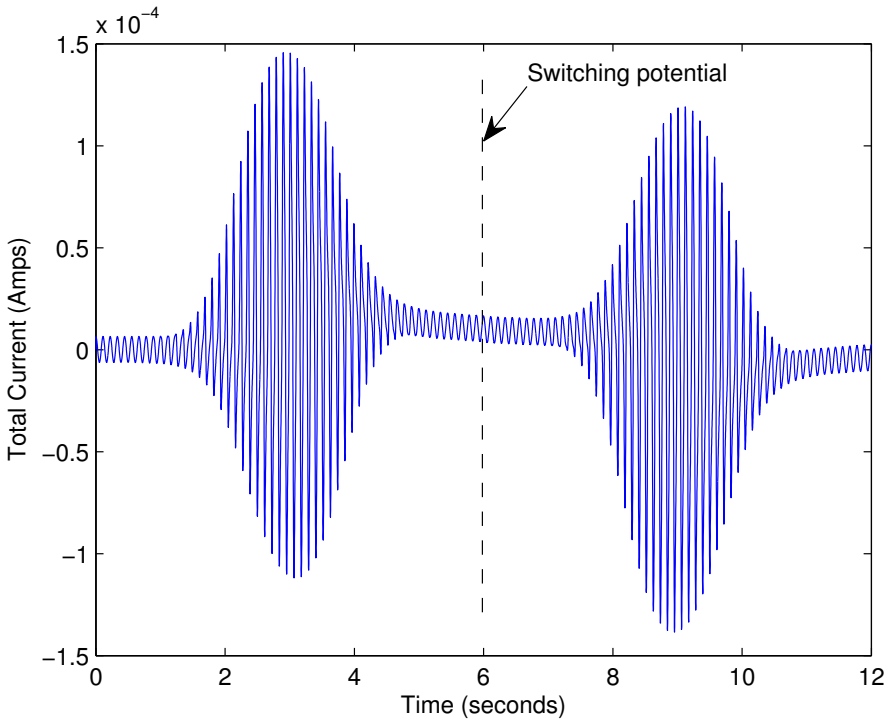

Figure 2.2: An example of the current resulting from the simulation of a cyclic AC voltammetric experiment including the effects of resistance and capacitance, with the time at which the switching potential is reached indicated. Parameters used were $E_{start} = -0.3$ V, $E_{max} = 1.0$ V, $\nu = 0.1$ V s^{-1}, $dE = 0.08$ V, $\omega = 2\pi \times 9$ Hz, $D = 2.5 \times 10^{-5}$ cm^2 s^{-1}, $S = 0.071$ cm^2, $c_\infty = 1$ mM, $T = 296$ K, $E^0 = 0$ V, $k^0 = 10^3$ cm s^{-1}, $\alpha = 0.5$, $R_u = 80\ \Omega$, $C_{dl} = 20\ \mu$F cm^{-2}.

oscillating background current due to capacitive effects.

Figure 2.3 shows the effects of varying k^0, with other parameter values fixed and listed in the caption. As we would expect, the peak current in general increases with k^0, as this parameter governs how quickly reactions are taking place. However, it is important to notice that beyond a certain value, here somewhere between $k^0 = 0.1$ cm s^{-1} and $k^0 = 1$ cm s^{-1}, a stage is reached beyond which there is

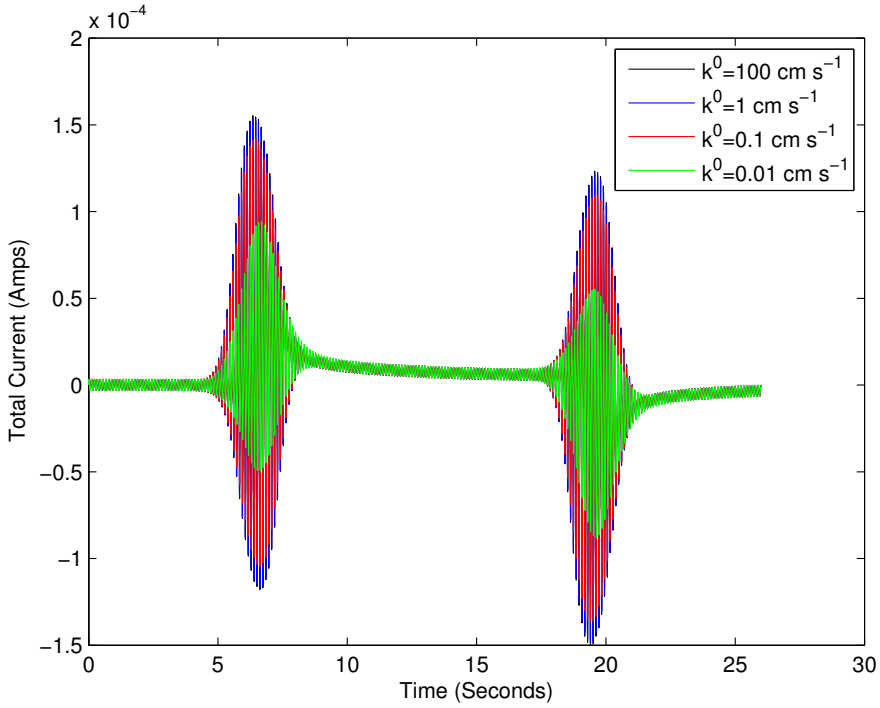

Figure 2.3: An example of the effect of varying k^0 on the resulting current in a simulation of a voltammetric experiment. Parameters used were $E_{start} = -0.3$ V, $E_{max} = 1.0$ V, $\nu = 0.1$ V s^{-1}, $dE = 0.08$ V, $\omega = 2\pi \times 9$ Hz, $D = 2.5 \times 10^{-5}$ cm^2 s^{-1}, $S = 0.071$ cm^2, $c_\infty = 1$ mM, $T = 296$ K, $E^0 = 0.3$ V, $\alpha = 0.5$, $R_u = 50\ \Omega$, $C_{dl} = 10\ \mu$F cm^{-2}.

no noticeable change in the current recorded as k^0 is increased. This can be seen in Figure 2.3, where the black line corresponding to $k^0 = 100$ cm s^{-1} is indistinguishable from the blue line corresponding to $k^0 = 1$ cm s^{-1}. We will refer to this as the "reversible limit". Beyond this value, reactions are taking place as frequently as possible within the restrictions of the other parameters, and k^0 is no longer a limiting factor. Chemical systems whose rate constants lie in such a range will be referred to as being "fully reversible", whereas those with rate constants below the reversible limit will be referred to as "quasi reversible".

2.2.3 The inverse problem

Having formulated and tested our simulation method, we continue by testing the parameter fitting method outlined in Chapter 1. We want to minimise our objective function value, L_{Glo}, given by

$$L_{Glo} = \sum_{i=1}^{n} \left[(I_i - G_i(y))^2 \right], \tag{2.29}$$

with I_i being the known current values, for example experimental data, $G_i(y)$ being simulated data, and n being the number of discrete measurements in each of these data structures. In order to do this, we re-calculate $G_i(y)$ after adjusting parameter values, employing a quasi-Newton method [43] implemented in the NAG C library [77] as `e04fcc`. This algorithm contains the strategy for updating values of the free parameters in order to obtain a minimal value of L_{Glo}. It works by approximating the objective function as quadratic in all variables around the minimum, but uses approximations to the Hessian matrix, unlike the standard Newton method, making it more computationally efficient.

A general search space for the parameters would be over all possible physical values, so in the case of the five parameters in the single electron transfer reaction, this might be

$$E_{min} \leq E^0 \leq E_{max}, \tag{2.30}$$

$$0 \leq \alpha \leq 1, \tag{2.31}$$

$$0 \leq k^0 \leq 100, \tag{2.32}$$

$$0 \leq C_{dl} \leq 1, \tag{2.33}$$

$$0 \leq R_u \leq 500. \tag{2.34}$$

In the above expressions, E_{min} and E_{max} represent the minimum and maximum values of the DC linear (or cyclic) component of the potential, between which E^0

should always lie assuming the experiment is well-designed. The bounds on α are part of the definition that it should lie between zero and one, and the lower bounds of zero on k^0, C_{dl} and R_u are imposed to keep the system physical. The upper bounds on those parameters are somewhat arbitrary, although in all cases significantly larger than one would expect to encounter, and can be increased should the algorithm report values close to those bounds. However we note that in an experimental setting it is often possible to provide an estimate of at least R_u based on measurements taken from a separate electrochemical impedance spectroscopy (EIS) [12] experiment performed prior to the main voltammetry exercise, so we are forewarned if it is likely to exceed the limit. In the cases of C_{dl} and k^0 we would adjust the upper bounds if the algorithm moves close to those values for a particular reaction, though we note that in all cases we have investigated the bounds given in Equations (2.31)–(2.34) are far above reported values for the parameters and, in particular, the bound on k^0 is far above the reversible limit for those cases.

The `e04fcc` algorithm is designed for unconstrained minimisation. In the case of the upper bounds on k^0, C_{dl} and R_u this is acceptable, but we must impose the lower bounds on all parameters, and the upper bounds on E^0 and α, to be able to guarantee reporting values which have any physical meaning. We accomplish this via setting a condition that the objective function value, L_{Glo}, becomes "infinite", taking a value many orders of magnitude larger than it otherwise would, should those parameters move out of their permitted ranges.

The final comment to make addresses the selection of starting values for the search algorithm. Again, when investigating a real chemical system, we often have information either from measurements obtained during the experiment or from previous work on the system in question, which allows us to choose our initial guess with some bias. In a general case, however, we may simply choose uniform random

numbers taken between the lower and upper bounds of the ranges for each parameter. As the minimisation algorithm is trivially parallelisable, it can be run multiple times with independently chosen random starting values. After all runs have completed, the algorithm is set to report the parameter values which result in the overall minimum value of L_{Glo} over all runs. Following this procedure gives us a way of tackling the problems associated with local minima in the objective function surface.

We will now present some results from testing our parameter recovery algorithm using only simulated experimental data. To begin with, we will simply fit parameters to unaltered simulations, in other words without the introduction of artificial noise, as the simplest example of the inverse problem.

It should be noted that although during the course of our simulations all variables are non-dimensionalised prior to the numerical solution scheme being implemented, we convert them back to dimensional form as a matter of course at the end of the simulation in order to facilitate discussion with our experimental collaborators, and this procedure is followed even in purely theoretical studies.

The results of these experiments are shown in Table 2.1. We have conducted two separate experiments, with extreme values of R_u (Experiment 1) and C_{dl} (Experiment 2). The other "unknown" parameters were set to values at realistic levels, i.e. ones that might be encountered in a real experiment. Values used for the "known" parameters were $E_{start} = -0.3$ V, $E_{max} = 1.0$ V, $\nu = 0.1$ V s^{-1}, $dE = 0.08$ V, $\omega = (2\pi)\times 9$ Hz, $D = 2\times 10^{-5}$ cm^2 s^{-1}, $S = 0.071$ cm^2, $c_\infty = 1$ mM, $T = 297$ K.

As we would hope and expect, in the case where we have not altered the simulated data at all, the algorithm is able to recover the parameter values exactly. In an

	Experiment 1		Experiment 2	
Parameter	Simulated	Recovered	Simulated	Recovered
α	0.50	0.50	0.50	0.50
E^0 / V	0.00	0.00	0.20	0.20
k^0 / cm s^{-1}	0.10	0.10	0.10	0.10
R_u / Ω	2000	2000	140	140
C_{dl} / μF cm^{-2}	25	25	500	500

Table 2.1: The parameter values recovered from a simulation using an AC signal with no added noise. Values of the fixed experimental parameters were $E_{start} = -0.3$ V, $E_{max} = 1.0$ V, $\nu = 0.1$ V s^{-1}, $dE = 0.08$ V, $\omega = (2\pi) \times 9$ Hz, $D = 2 \times 10^{-5}$ cm^2 s^{-1}, $S = 0.071$ cm^2, $c_\infty = 1$ mM, $T = 297$ K.

experimental context, however, we must account for the fact that there is random noise on the signal due to measurement errors in the instrumentation. If our "perfect" simulated data is perturbed slightly, it is not necessarily obvious that the parameter recovery algorithm will report parameter values which are even remotely close to the ones used to generate the data in the first place.

In order to investigate the effect of noise on the algorithm, we must first develop a strategy for including noise in our simulations. In [39], the authors propose two possible methods for including noise. In the first case, noise at each time point where a measurement of current occurs is assumed to be proportional to the current measured at that time point, whereas in the second case, noise at each time point is assumed to be proportional to the peak current measured throughout the experiment. In both cases, the noise is drawn from a normal distribution with zero mean, and the standard deviation taken to be a percentage of either this varying

or peak current, so that at each time value, either

$$I_{noisy} = I_{exact} + prI_{exact}, \tag{2.35}$$

or

$$I_{noisy} = I_{exact} + prI_{max}. \tag{2.36}$$

In both cases p is the percentage of the current which determines the standard deviation, r is a realisation of a $N(0,1)$ random variable, I_{exact} is the numerically simulated value for the current, and I_{max} is the maximum absolute value of the current over the whole experiment.

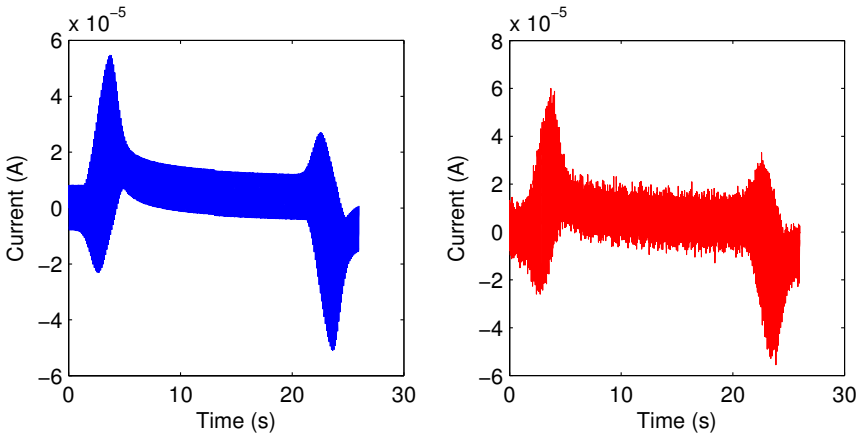

Figure 2.4: A comparison between the signal resulting from simulation of an AC voltammetric experiment with (right, red) and without (left, blue) added noise. Noise was added according to Equation (2.36) with $p = 0.05$, and simulation parameters were set to be those used in Experiment 1 of Table 2.1, so $E^0 = 0.0$ V, $k^0 = 0.1$ cm s^{-1}, $\alpha = 0.5$, $R_u = 2000\ \Omega$, $C_{dl} = 25\ \mu$F cm^{-2}, $E_{start} = -0.3$ V, $E_{max} = 1.0$ V, $\nu = 0.1$ V s^{-1}, $dE = 0.08$ V, $\omega = (2\pi) \times 9$ Hz, $D = 2 \times 10^{-5}$ cm^2 s^{-1}, $S = 0.071$ cm^2, $c_\infty = 1$ mM, $T = 297$ K.

We will choose to add noise of the form given in Equation (2.36) at a value of 5%,

i.e. $p = 0.05$, and using this, repeat the experiments whose results were presented in Table 2.1. The form of noise is chosen based on analysis of the actual noise recovered from an experimental data set, as we will see in Section 2.3.3, where the magnitude of the noise is around 2% of I_{max}. Figure 2.4 shows the effect of adding noise to the signal, with the left panel (blue) showing the clean signal, and the right panel (red) showing the signal after 5% noise has been added.

	Experiment 1			Experiment 2		
Parameter	Simulated	Recovered	std	Simulated	Recovered	std
α	0.50	0.50	0.00	0.50	0.50	0.00
E^0 / V	0.000	0.000	0.000	0.200	0.200	0.000
k^0 / cm s^{-1}	0.1000	0.1040	0.0185	0.1000	0.1000	0.0051
R_u / Ω	2000	2000	15	140	140	0.19
C_{dl} / μF cm^{-2}	25	25	0.0	500	500	0.0

Table 2.2: Parameters recovered from a simulation with 5% noise added, along with the standard deviation (std). For each parameter, the recovered value reported represents the average from ten runs. Other parameter values used were the same as for the experiments in Table 2.1, and are given in the text.

The results of repeating these experiments ten times each are given in Table 2.2. Even with what we will later see is a higher level of added noise than is typically encountered in a voltammetric experiment, the algorithm is able to recover most parameters with a high degree of accuracy, with only k^0 and R_u having any noticeable deviation from the values used in simulation. For these two parameters, the averaged values are almost equal to those values used in the simulation, and the standard deviations are around 1-2% of the values. Although only ten repeats were used, no reduction in the standard deviations reported for these parameters

is noticed upon doubling this to 20 runs, and while increasing this further to 100 or 1000 repeats may result in minimal reduction in these standard deviations, the accuracy of the estimates of most parameters would not change.

2.3 Results using experimental data

After testing our method in simulation, we will continue by investigating data acquired from AC cyclic voltammetric experiments conducted on the ferricyanide-ferrocyanide redox couple, the reaction given in Equation (2.2). As was mentioned already, we will test three possible methods of parameter recovery, and we have ten sets of data to enable us to comment on the reproducibility of the results, both with each individual method and overall for this particular system.

Experiments were conducted by our collaborators at Monash University, who also performed frequency-domain parameter estimation exercises using the Nimrod software. Analysis labelled as being conducted by the "Oxford" group was mainly done by the author without assistance, with the exception of the application of the "heuristic" parameter estimation method, where collaboration with Prof Bond was undertaken.

A plot of the recorded current against time taken from the first of the ten experiments is displayed in Figure 2.5. As the reaction is a reduction, rather than an oxidation, the underlying cyclic DC ramp initially has negative gradient, with $E_{start} = 0.5$ V, $E_{min} = -0.1$ V, and scan rate $\nu = 0.0894$ V s^{-1}. The AC perturbation has amplitude $\Delta E = 0.08$ V and frequency $f = 9.015$ Hz (angular frequency $\omega = 2\pi f$). Other controlled parameters are the electrode surface area $S = 0.07$ cm^2, ambient temperature $T = 297$ K, electrolyte concen-

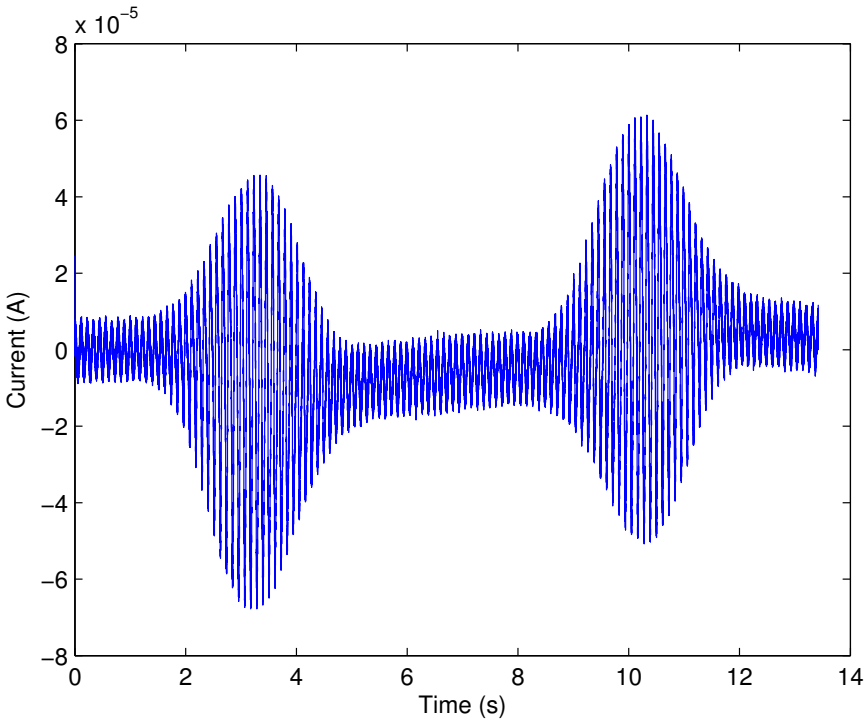

Figure 2.5: An example voltammogram taken from the first $[Fe(CN)_6]^{3-/4-}$ experiment.

tration $c_\infty = 1.0$ mM, and for simulations, the diffusion coefficient of the analyte, $K_3Fe^{III}(CN)_6$, was $D = 7.2 \times 10^{-6}$ cm^2 s^{-1}. These parameters were the same for all ten repeats of the experiment. Features to note in the time-domain plot in Figure 2.5 are the two peaks, or areas of activity, corresponding to potentials close to E^0 on the backwards and forwards sweeps of the cyclic potential, which are referred to as the "Faradaic regions", as well as the relatively constant background current present across the rest of the plot.

2.3.1 Heuristic method

Heuristic methods are among the most widely used methods for parameter estimation in (particularly) AC voltammetry. In such a method, an operator will use software for simulating voltammetric experimental data, and follow a preferred recipe for adjusting parameter values until a visual match between theory and experiment is obtained. In the case of AC voltammetry, this will usually involve the DC component, and a selection of the available filtered harmonics chosen based on experience as ones which might most easily show the effects of variation of specific subsets of the free parameters. The operator will switch between the selected harmonics adjusting the free parameters until all chosen harmonics are seen to match when comparing theory to experiment.

This short description already serves to hint at the major disadvantage of heuristic methods, namely that they are always somewhat arbitrary. Even if every laboratory followed an identical recipe for parameter adjustment, which is certainly not the case in reality, criteria for acceptance of a particular value are based entirely on operator choice. Furthermore, there is an implicit assumption in the heuristic method that when a suitable visual match between experiment and simulation is obtained, the unique solution for the values of the model parameters has also been obtained. This is not necessarily the case, and we shall see one example of non-uniqueness in Chapter 3. This results in the heuristic method being inherently unreproducible.

As a partial demonstration of this lack of reproducibility, as well as for later comparison of results with those obtained using other methods, we give the parameter estimates recovered by the operators at two laboratories, Oxford and Monash, using subtly different heuristic methods on exactly the same ten sets of experimental

data. In order not to bias the results, there was no consultation between the two groups at any point during the experiment, including on the choice of heuristic method itself.

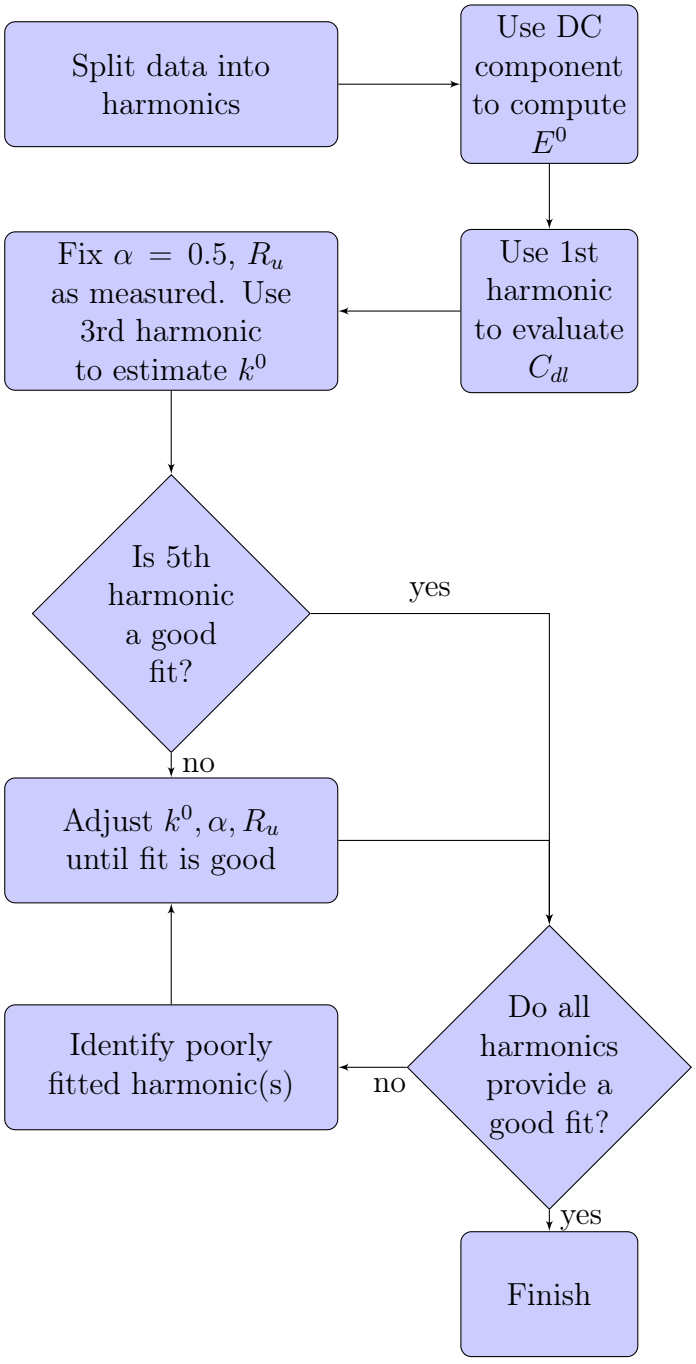

Figure 2.6: A recipe for a heuristic method of analysis of AC Fourier-transformed voltammetric data as used at Oxford.

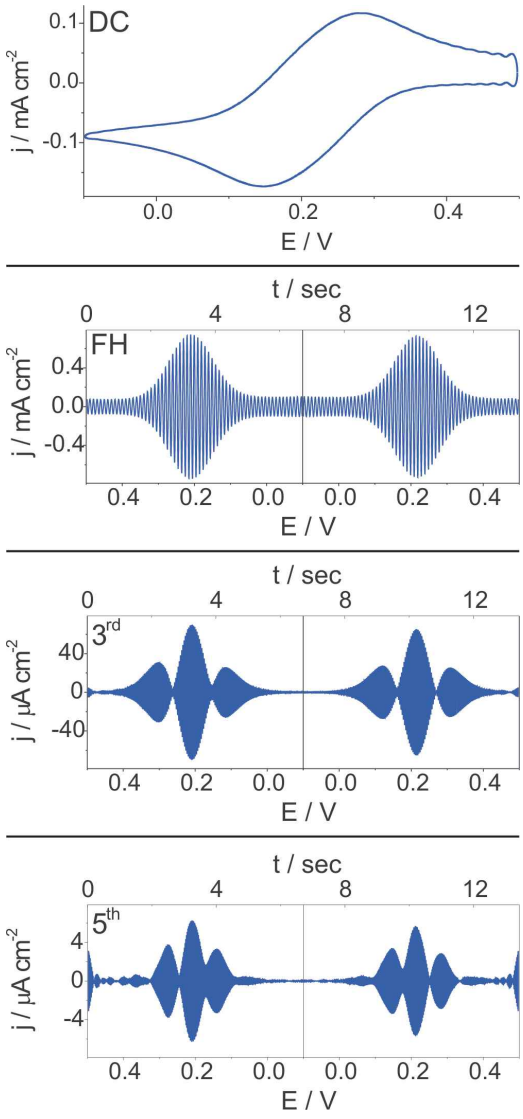

Figure 2.7: The DC component along with the first, third and fifth harmonics as used in the heuristic approach outlined in Figure 2.6 and described in the text. Some ringing is visible at the edges of the fifth harmonmic.

The recipe followed at Oxford, based on one developed during a previous study [92], is shown as a flowchart in Figure 2.6. The harmonics, shown in Figure 2.7, are filtered out via the process described in Chapter 1. From the DC component, E^0 is set to be the average of the oxidation and reduction peak potentials. As almost all of the background capacitative current is contained in the fundamental (1st) harmonic because the response to C_{dl} is linear, C_{dl} is adjusted to match the background currents in this harmonic in the regions away from the peaks resulting from Faradaic current. These two parameters are regarded as fixed, and the remaining three, being k^0, α and R_u, are adjusted to match particularly the 3rd and 5th harmonics, before a check over all harmonics is performed at the end. The higher harmonics are used here, as they are typically much more sensitive to changes in especially k^0 and α.

In the case of this particular set of experiments, at Oxford we chose to fix $\alpha = 0.5$ after initial analysis, and regard any variation from this value as being within experimental error. We were also unable to identify R_u precisely, only obtaining the condition $R_u \leq 10\ \Omega$ due to the current response being insensitive to minor variations in the value of R_u at that range. As a result, we chose to accept the experimentally measured values which all fell beneath this bound. The Monash group, on the other hand, fixed R_u at experimentally measured values from the outset, and allowed α to vary. They then followed almost the same protocol, but included the values of the peak potentials in the harmonics in their calculation of E^0.

The results of the heuristic parameter fitting are shown in Table 2.3. There is good agreement between the two independently undertaken exercises, though the results are not identical. Both of these observations are consistent with our comments about the nature of heuristic methods. Overall we note that the values

Exp. No.	R_u / Ω	E^0 / V		k^0 / cm s^{-1}		C_{dl} / μF cm^{-2}		α	
		Mon.	Ox.	Mon.	Ox.	Mon.	Ox.	Mon.	Ox.
1	6	0.214	0.213	0.0105	0.0110	17	17	0.52	0.50
2	4	0.214	0.214	0.0090	0.0089	18	19	0.52	0.50
3	5	0.214	0.213	0.0065	0.0067	16	16	0.52	0.50
4	5	0.214	0.213	0.0055	0.0058	16	17	0.52	0.50
5	6	0.214	0.213	0.0095	0.0091	18	19	0.52	0.50
6	7	0.215	0.213	0.0080	0.0080	20	20	0.52	0.50
7	8	0.215	0.214	0.0095	0.0100	23	24	0.52	0.50
8	7	0.216	0.217	0.0160	0.0150	24	24	0.51	0.50
9	8	0.216	0.217	0.0180	0.0190	25	22	0.51	0.50
10	7	0.217	0.217	0.0115	0.0110	23	23	0.51	0.50

Table 2.3: Parameters recovered from the ten repeats of the $[Fe(CN)_6]^{3-/4-}$ experiment using a Heuristic approach at Monash [a] (Mon.) and Oxford [b] (Ox.) universities.

[a] Similar protocol was used to that in Figure 2.6, but in this case R_u was taken to be the experimentally measured value, and E^0 was deduced from peak potentials in odd harmonics and minima in even harmonics.

[b] The heuristic approach detailed in Figure 2.6 was used. In this evaluation, R_u was estimated to be less than 10 Ω but could not be determined beyond this, so we chose to use the values measured experimentally in simulations. We also regarded variations of α from 0.50 to be within experimental error, and did not attempt to vary this parameter to see whether a better fit could be obtained.

of k^0 do indeed fall in a range supporting the classification of this reaction as quasi-reversible, but we also note that both groups report significant variation in this range of k^0 values over the ten experiments, in spite of careful attempts to reproduce the experimental conditions.

2.3.2 Automated FT matching

The second parameter fitting method we consider is a frequency domain matching of the harmonics using the Nimrod software [3]. This package was both written and used at Monash, and employs parallel processing resources and a simplex-type method [74] to simultaneously fit all parameters over potentially all the available harmonics.

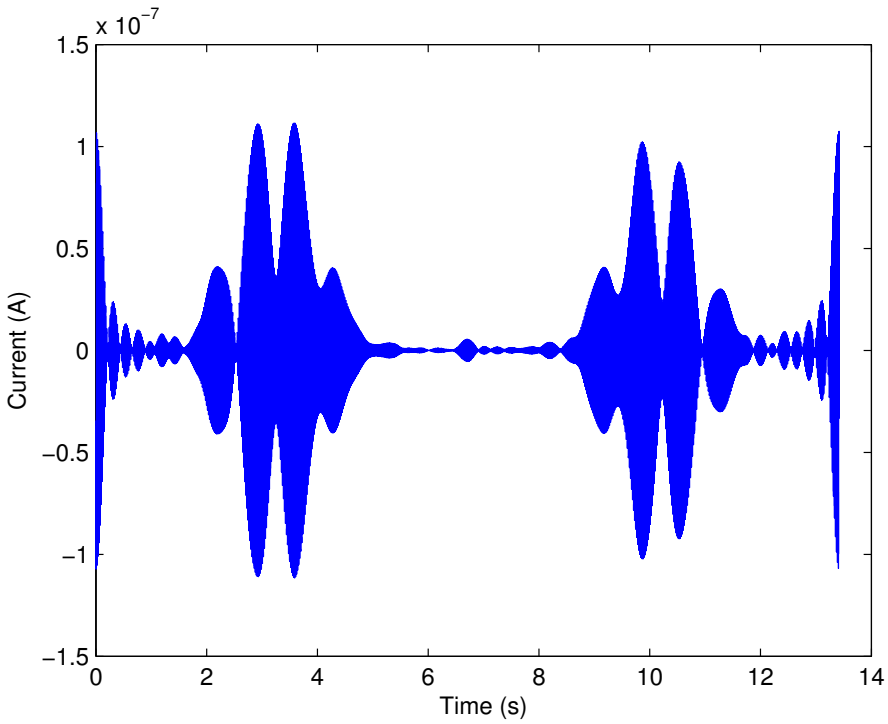

Figure 2.8: The 6th harmonic taken from the first $[Fe(CN)_6]^{3-/4-}$ experiment.

The method is extremely powerful, but ultimately has two serious drawbacks. Firstly, as can be seen in the lower panel of Figure 2.7 and more clearly in Figure 2.8, when dealing with higher harmonics there are often numerical artefacts at the beginning and end of the time series as a result of the Fourier transform and the filtering processes using a sharp rectangular window, often referred to as ringing. Figure 2.8 shows these effects exaggerated, as we have chosen to display the 6th harmonic where these effects are at their most extreme out of the harmonics actually used for frequency-domain parameter optimisation in this study. We can see even in the lower panels of Figure 2.7 that ringing effects are noticable, though of smaller magnitude than in this 6th harmonic. In the case of Figure 2.8, these undesired features are of comparable amplitude to the actual signal, so any numerical optimisation attempted would be in danger of being greatly distorted. In practice, this issue is addressed by an operator telling the program to ignore the initial and final portions of the data. In the case of our $[Fe(CN)_6]^{3-/4-}$ experiments, this was chosen to be the first and last second of the experiment. This results in the method not being fully automatable, as operator intervention is required to decide how much of the data must be ignored. It also means that higher harmonics are rarely of much use, as the signal is dominated by ringing, and in order to remove this using the method described above, portions of the information contained in the harmonic are also lost.

While an alternative method of filtering to the rectangular window described in Chapter 1 could be used, one must be careful to preserve the full magnitude of the harmonic, which other options such as the Gaussian or Hanning windows do not manage. During the course of this project a brief investigation of different forms of filter was conducted, and hybrid windows composed of a rectangular section joined to a Gaussian decay at the edges did result in some reduction in the magnitude of ringing effects over the rectangular window method, while preserving

the information contained in the harmonics. As frequency-domain methods are not the main focus of this thesis and ringing effects do not change the results from the time-domain method, however, we chose not to include these preliminary results.

The second drawback is that even in spite of the vast amount of resources available for running the optimisation, the number of parameters and search ranges for those parameters must often be small in order for the run time to be realistic. In the case of these experiments, a 4-parameter search took parallel computing resources at Monash on the order of an hour to perform the optimisation, while the algorithm of the following section required only minutes on a standard desktop computer.

The results of this method are shown in Table 2.4. As we can see, the optimisation was performed on only four parameters and in quite a narrow search space, which requires some prior knowledge of the expected results. In this case, the bounds on the search space were chosen based on the results of the heurstic approach of the previous section, with C_{dl} in fact being fixed at the value obtained via heuristic fitting in the fundamental harmonic. In the end, the results show good agreement with those obtained using the heuristic method.

2.3.3 Automated time-domain matching

The final method we consider is our time-domain optimisation method, as presented in Chapter 1. Unlike the two frequency-domain methods we have looked at, where the band selection for harmonics acts as a filter, we must quantify the amount of noise in the data before proceding. Our approach to this is simply a logical extension of the method behind obtaining the harmonics, which was outlined in Chapter 1. When looking at the power spectrum, we can clearly see where the contributions from the harmonics are located, and we simply define all other

Exp. No.	R_u / Ω	E^0 / V	k^0 / cm s^{-1}	C_{dl} / μF cm^{-2}	α	L_{Nim}
1	6	0.213	0.0110	17	0.52	0.08
2	5	0.213	0.0089	18	0.51	0.10
3	6	0.212	0.0064	16	0.51	0.16
4	7	0.213	0.0052	16	0.51	0.20
5	7	0.213	0.0093	18	0.51	0.09
6	6	0.214	0.0081	20	0.51	0.11
7	8	0.214	0.0096	23	0.51	0.08
8	6	0.216	0.0160	24	0.52	0.05
9	8	0.216	0.0180	25	0.52	0.04
10	7	0.217	0.0110	23	0.52	0.07

Table 2.4: The parameters recovered from the ten repeats of the ferricyanide experiment using Nimrod software and frequency domain matching [a,b].

[a] In this form of data analysis, Simplex optimisation was performed for the 2nd, 3rd, 4th, 5th and 6th harmonics to minimise the objective function, L_{Nim}, which is calculated as the relative root mean square deviation:

$$L_{Nim} = \sqrt{\frac{\sum_{i=1}^{N}(f^{exp}(x_i) - f^{sim}(x_i))^2}{\sum_{i=1}^{N} f^{exp}(x_i)^2}}, \tag{2.37}$$

where $f^{exp}(x)$ and $f^{sim}(x)$ are experimental and simulated functions, respectively, and N is the number of data points.

[b] Ten starting values for E^0, k^0, R_u and α optimisation were randomly selected within the search space 0.1 V $< E^0 <$ 0.3 V, 10^{-3} cm s^{-1} $< k^0 <$ 1 cm s^{-1}, 1 Ω $< R_u <$ 20 Ω, $0.4 < \alpha < 0.6$. The parameters with the lowest matching objective were selected, and the average values are presented. C_{dl} was fixed at the values given by Monash in Table 2.3.

frequencies as being "the noise", composed of a combination of random measurement errors along with systematic noise at 50 Hz and 100 Hz caused by mains electricity frequencies in Australia.

In previous work, questions have been asked about the relevance of this systematic contribution due to mains electricity frequencies, but here we can isolate those via the same band selection techniques as are used to filter harmonics. Selecting the bands at 50 and 100 Hz, we can perform an inverse Fourier transform, and then comparing the maximum amplitude of the resulting signal with the amplitudes both inside and outside the Faradaic region, we find that systematic noise accounts for less than 0.1% of the signal inside, and less than 1% outside, this region.

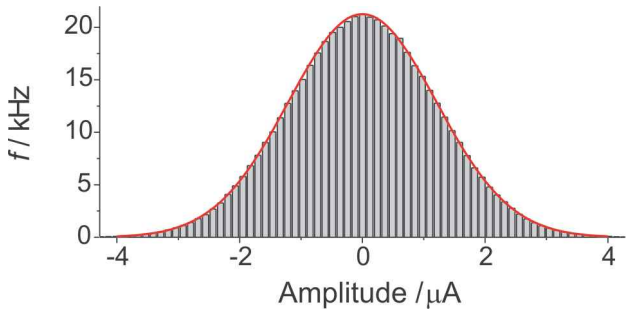

Figure 2.9: A histogram showing the noise recovered from the first $[Fe(CN)_6]^{3-/4-}$ experiment in blue. The red curve is a best-fit normal distribution to these data.

Similarly filtering the noise, or equivalently removing the contribution of the identifiable harmonics – in this case the first six – from the total signal, we can plot a histogram and look at its distribution, as shown in Figure 2.9. By eye, it appears as though the approximation of a normal distribution is quite valid. Indeed, statistical tests such as the Kolmogorov-Smirnov test [65] (implemented in Matlab as `kstest`) suggest that the hypothesis that the noise is sampled from a normal distribution should not be rejected at a 5% significance level.

Considering the noise from all ten experiments in this way, we can report the values

Experiment	Mean	std/I_{max}
1	4.7×10^{-22}	0.0178
2	-1.3×10^{-22}	0.0184
3	5.9×10^{-22}	0.0194
4	-6.9×10^{-23}	0.0193
5	4.5×10^{-22}	0.0184
6	-2.8×10^{-22}	0.0183
7	1.1×10^{-21}	0.0157
8	1.9×10^{-22}	0.0152
9	-3.8×10^{-22}	0.0144
10	-3.3×10^{-22}	0.0159

Table 2.5: The mean and scaled standard deviation of the noise recovered from each of the 10 runs of the $[Fe(CN)_6]^{3-/4-}$ experiment.

of the mean and standard deviation in each case, with the standard deviation scaled by the maximum current, consistent with Equation (2.36) from earlier in the chapter. The results of this are shown in Table 2.5. In every case, the mean is effectively zero, and the standard deviation is between 1.5% and 2% of the maximum current. This value is significantly lower than our estimate of 5% during the simulation section, and as that had very little perceptible impact on the results of the parameter recovery process, we will continue under the assumption that even lower levels of noise will have a similarly small effect.

After completing this check, we may move on to apply the time-domain parameter recovery method to the ten sets of experimental data. In this case, four parameters were optimised simultaneously, with search ranges similarly large to those used in the simulation section, and random initial guesses. The 5th parameter, R_u, was fixed at the experimentally measured values, as based on our heuristic work identification within the $0 \leq R_u \leq 10\ \Omega$ range was difficult, and had no effect on the other parameter values. Within the numerical solution scheme, 8192 equally-spaced time points were used. The number was a power of 2, as there were 2^{19} measurements in the experimental data file, so this means we take every 64th data point to correspond exactly to the same time point as in the simulation. The number was chosen far larger than was required for the numerical scheme to converge, but not so large that the subsequent optimisation took unfeasible amounts of time. On a standard office desktop PC with an AMD FX-4100 processor and 8 GB RAM, a single run of the optimisation algorithm took of the order of a minute, for the sake of comparison to the run-time of the Nimrod algorithm.

Results from the time-domain optimisation on each of the ten experiments are given in Table 2.6. Unlike in the other two methods, no operator intervention was involved in obtaining these. The disadvantage of the fully-automed time-domain

Exp. No.	R_u / Ω	E^0 / V	k^0 / cm s^{-1}	C_{dl} / μF cm^{-2}	α	L_{Glo}
1	6	0.213	0.0103	17	0.55	7.06e-8
2	4	0.212	0.0089	19	0.54	7.17e-8
3	5	0.212	0.0067	16	0.54	7.07e-8
4	5	0.212	0.0058	17	0.54	6.99e-8
5	6	0.212	0.0091	19	0.53	6.95e-8
6	7	0.214	0.0080	20	0.54	7.00e-8
7	8	0.214	0.0101	24	0.53	6.90e-8
8	7	0.215	0.0152	24	0.53	6.95e-8
9	8	0.216	0.0187	25	0.54	7.28e-8
10	7	0.217	0.0113	23	0.54	7.07e-8

Table 2.6: The parameters recovered from the ten repeats of the $[Fe(CN)_6]^{3-/4-}$ experiment using fully-automated time-domain matching.

parameter estimation method is that it relies on having an extremely accurate model of the "forwards" problem to produce simulated data. In the heuristic method it is acceptable for the simulations to match by eye, but to a computer, this concept is not as easily used. One simple example of this is to note that using an incorrect frequency for the AC component in the simulations, even by a very small amount, can produce results which an experienced electrochemist would dismiss on sight, due to introducing a seemingly minute but gradually increasing phase shift into the simulations, causing the rapid oscillations to become desynchronised. Another example, which we do not have to deal with here but will encounter again in Chapter 3, is that the assumption of constant background capacitative current is not always valid, as even to the eye it can be a clearly varying quantity, which then requires a different model. In this example, however, that is not an issue, and problems such as the phase shift due to incorrectly recorded frequency can be circumvented via adding ω as an additional free parameter to search, within a very narrow range around the reported value, so here $9.00 \leq \omega/2\pi \leq 9.03$ Hz. In the end, there is generally good agreement between the results from this method and those from both the heuristic and Nimrod methods. Once again, we notice consistent values for most parameters, along with a small but significant range over which k^0 varies.

2.3.4 Comparison between methods

Table 2.7 summarises the results of all three methods of parameter estimation, with averages and standard deviations over the ten data sets. We see good agreement between all methods, although it is noticeable that the values of α reported by the time-domain method are slightly higher than those given by the other methods. This is likely to be due to a combination of two factors. Firstly, the time-domain

Method		R_u / Ω	E^0 / V	k^0 / cm s^{-1}	C_{dl} / μF cm^{-2}	α
Heuristic (Oxford)	Avg	6.3	0.214	0.0104	20	0.50
	Std	1.3	0.002	0.0040	3.0	N/A
Heuristic (Monash)	Avg	6.3	0.215	0.0104	20	0.52
	Std	1.3	0.001	0.0039	3.5	0.01
Nimrod	Avg	6.6	0.214	0.0100	20	0.51
	Std	1.0	0.002	0.0040	3.5	0.01
Global automated	Avg	6.3	0.214	0.0102	20	0.54
	Std	1.3	0.002	0.0037	3.3	0.01

Table 2.7: Averages and standard deviations in the parameters recovered over all 10 data sets using each of the methods of analysis.

method is much less sensitive to relatively small changes in the value of α compared with the higher harmonics, which each of the other methods employ. We can see in Figure 2.10 that it is almost impossible to see a difference in the top panel, showing the time-domain, when α is changed from 0.50 to 0.55, whereas in the lower panel, showing the 5th harmonic, the difference is obvious. The second factor is that, even though we have claimed that the background current is constant, it may be that there is a small variation, or that there is some other subtlety not included in our simulation model. Such an effect would be small enough that to operator-dependent methods, there may be no difference detectable by eye. In addition, if it is simply the background current model being inaccurate, this is bypassed by the methods using the frequency domain, as in the higher harmonics the background current has almost no presence. In the time-domain, a small flaw in the model could easily be compensated for by comparably small adjustments in the other free parameters.

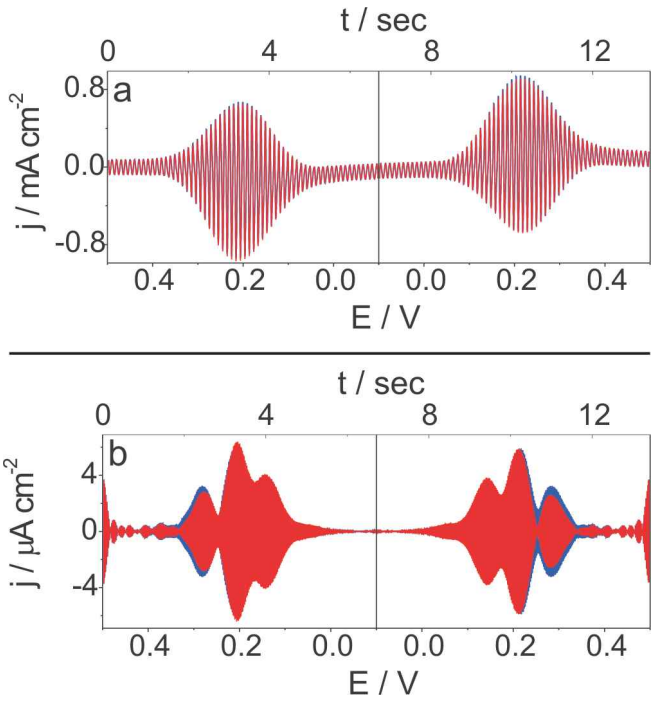

Figure 2.10: The total current (a) and fifth harmonic (b), showing the response to a variation in α. Here, blue plots use $\alpha = 0.50$ and red use $\alpha = 0.55$.

The agreement between available methods of parameter estimation is strong, and consistent with results in the literature. The variation noticed across all methods in the value of k^0 from experiment to experiment might be explained by microscopic variations in the surface of the carbon electrode, which has been the subject of study by other authors [8,27,30,31,54,55,60,68,69,78]. Although every attempt was made to ensure identical conditions for each experiment, in practice, even cleaning and polishing the electrode in between consecutive experiments is not an easily-repeatable process, and the effect of this pre-treatment could have contributed to the range of k^0 values reported being caused by such electrode surface variation.

2.4 Conclusions

We have presented an operator-independent method of parameter estimation for use on data from AC voltammetric experiments, and tested it both in simulation and on real data for the case of a single electron transfer under a quasi-reversible regime. In the case of the experimental data, we have compared the proposed method with two operator-dependent methods currently in use in laboratories, and it has successfully produced results consistent with both. All three methods have advantages and disadvantages, and the reality may be that using a combination of these approaches in their current forms would be the optimal approach to solving a problem. However, when taken along with the final goal of being able to provide a reproducible method for parameter estimation for use in different laboratories, the time-domain method is clearly a useful tool, and a step towards that goal.

Chapter 3

Problems of over- and under-parameterisation

In the previous chapter, we investigated the advantages and disadvantages of several methods of parameter recovery in the field of AC voltammetry and, in particular, used the experimental example of the reduction of $[Fe(CN)_6]^{3-}$ as a proof of concept of the time-domain method. In this chapter, we will extend this investigation by looking at a reaction whose kinetics fall close to the regime described as "fully reversible". Particular emphasis will be placed on the importance of using the most appropriate model for the underlying chemistry, and the problems encountered when this is not done. The work in this chapter is based on the paper *Inappropriate use of the quasi-reversible electrode kinetic model in simulation-experiment comparisons of voltammetric processes that approach the reversible limit* (accepted for publication in Analytical Chemistry).

3.1 Background

The main experimental system we will consider in this chapter is the single electron oxidation of ferrocene

$$Fc \rightleftharpoons Fc^{+} + e^{-}. \tag{3.1}$$

As with the reduction of ferricyanide in the previous chapter, to which we will briefly refer again, this reaction has also been the subject of numerous studies over a long period of time [10, 28, 53, 82, 89, 98]. In contrast with those from the $[Fe(CN)_6]^{3-}$ process, however, reported values of the reaction parmeters have varied widely from laboratory to laboratory over time with, in particular, estimates of the value of k^0 having ranged over several orders of magnitude, in spite of attempts to produce identical experimental conditions.

The process described in Equation (3.1) has been said to exhibit kinetics which approach the limit of reversibility [19]. Reactions such as this which fall into the "Nernstian" or "fully-reversible" regime may be modelled differently from quasi-reversible ones, with the parameters k^0 and α no longer featuring or having any meaning. In the course of this chapter, we will investigate the implications of the selection of either the fully-reversible or quasi-reversible model on the parameter recovery process. This will be done in the context of 10 repeated experiments on the $Fc^{0/+}$ reaction at each of two concentrations and two frequencies.

By making use of the statistical method of bootstrapping, as well as contour plots of some objective function surface cross-sections, we will describe some of the pitfalls that automated methods of parameter recovery can run into when an inappropriate model for the system under investigation is employed. This will serve as an important contribution to the overall goal of producing an operator-independent method of parameter recovery in AC voltammetry, as problems of over- and under-

parameterisation will appear often when more complex reaction mechanisms are considered.

3.2 Methods

As we are dealing with a single electron transfer reaction again, the mathematical model and solution scheme for a quasi-reversible process are exactly the same as in Chapter 2, only altered for this reaction being an oxidation rather than a reduction.

For a fully-reversible reaction, it is possible to use an alternative mathematical model. Substituting the boundary condition

$$\frac{c_{ox}(0,t)}{c_{red}(0,t)} = \exp\left[\frac{F}{RT}\left(E(t) - E^0\right)\right], \tag{3.2}$$

in place of Equation (2.6), it has been shown that for sufficiently large values of k^0 relative to the diffusion coefficient, D, and scan rate, ν, the quasi-reversible model produces results indistinguishable from the fully-reversible model [11]. In such a case, variations in α have no effect, therefore for our simulations of the $Fc^{0/+}$ reaction as a fully-reversible process, we will simply use the quasi-reversible model with fixed values of $k^0 = 1000$ cm s^{-1} and $\alpha = 0.5$.

As our tools of parameter recovery, we will again use the automated time-domain optimisation method from the previous chapter, along with frequency-domain optimsation via the Nimrod software developed at Monash.

3.3 Results

For this study, 10 sets of experimental data for the $Fc^{0/+}$ process were produced at each of two concentrations, c_{red}, being 0.92 mM ("1.0 mM" from now on) and 0.098 mM ("0.1 mM"), and each of two frequencies, f, being 9.02 Hz ("9 Hz") and 72.05 Hz ("72 Hz"), along with a single experiment run at 219 Hz at the lower concentration. Other controlled parameters were $D = 2.4 \times 10^{-5}$ cm^2 s^{-1}, $S = 0.07$ cm^2, $T = 297$ K, $\nu = 0.10431$ V s^{-1}, and $\Delta E = 0.08$ V. The potential limits, E_{start} and E_{max}, varied for each experiment, and are as given in Table 3.1.

Experiment	0.1 mM		1.0 mM	
	E_{start} (V)	E_{max} (V)	E_{start} (V)	E_{max} (V)
1	0.245	0.945	0.200	0.900
2	0.287	0.987	0.230	0.930
3	0.290	0.990	0.237	0.937
4	0.279	0.979	0.230	0.930
5	0.289	0.989	0.216	0.916
6	0.292	0.992	0.205	0.905
7	0.290	0.990	0.274	0.974
8	0.296	0.996	0.255	0.955
9	0.299	0.999	0.260	0.960
10	0.307	1.007	0.262	0.962

Table 3.1: The potential limits E_{start} and E_{max} for each of the 10 runs of the 0.1 mM and 1.0 mM Fc experiments.

3.3.1 Noise

Before proceding with the main analysis, we must again check the level of random noise on the data due to measurement errors, and ensure that it is of sufficiently low magnitude that the time-domain parameter recovery method can safely be used. Following exactly the same method as in the previous investigation, we can examine both this random noise and systematic noise due to mains frequencies at 50 Hz, by filtering out the first six harmonics using the Fourier transform.

Experiment	0.1 mM		1.0 mM	
	Mean	std/I_{max}	Mean	std/I_{max}
1	1.8e-10	0.0127	2e-18	0.0084
2	1.8e-10	0.0118	3e-18	0.0082
3	1.7e-10	0.0130	5e-18	0.0086
4	1.6e-10	0.0129	-1e-18	0.0089
5	1.8e-10	0.0136	-1e-18	0.0088
6	2.0e-10	0.0121	5e-19	0.0092
7	2.0e-10	0.0129	-3e-18	0.0086
8	1.8e-10	0.0118	-3e-18	0.0093
9	1.9e-10	0.0137	5e-18	0.0090
10	1.9e-10	0.0130	2e-18	0.0082

Table 3.2: The mean and scaled standard deviation of the noise recovered from each of the 10 runs of the 0.1 mM and 1.0 mM Fc experiments.

The "noise" on each set of data at 9 Hz is categorised in terms of its mean and standard deviation (std) scaled against the maximum current, I_{max}, in Table 3.2. At both 0.1 and 1.0 mM, the noise levels are low, with approximately mean 0 and standard deviation less than 1.5% and 1% of the maximum current in each

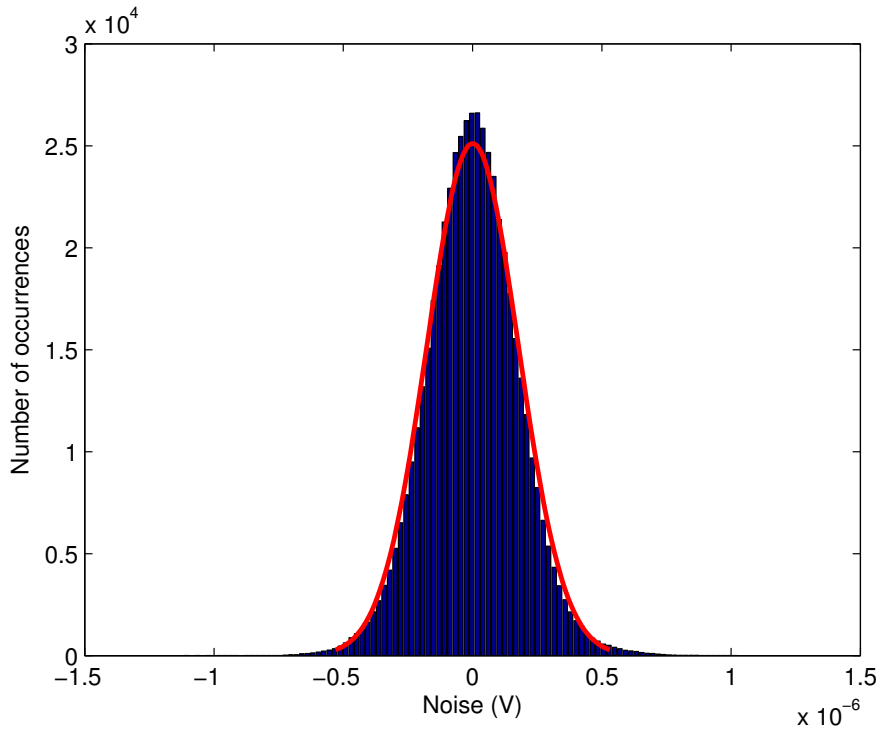

Figure 3.1: An example histogram of the noise taken from the first $Fc^{0/+}$ experiment at 0.1 mM. The red curve overlayed shows a best-fit normal distribution.

case, respectively. We also see again in Figure 3.1 that the noise is approximately normally distributed. Similarly, separating out the contributions at 50 and 100 Hz, the systematic noise can be seen to contribute less than 0.1% to the signal in the Faradaic region.

3.3.2 Parameter recovery: time-domain optimisation at 9 Hz

Having established that the noise is well under the 5% threshold that we tested in the previous chapter's simulations, we may now proceed to use the time-domain

parameter recovery method. We will begin by analysing the 1.0 mM $Fc^{0/+}$ data. Mathematical models used are abbreviated using the convention of model type followed by the number of parameters being fitted, where the model type is either QR (quasi-reversible) or FR (fully-reversible). For example QR5 would mean the quasi-reversible model where all five of E^0, k^0, C_{dl}, R_u and α are estimated, QR4 would mean the quasi-reversible model where E^0, k^0, C_{dl}, and α are estimated but R_u is fixed, and FR3 would mean the fully-reversible model where only E^0, C_{dl}, and R_u are estimated.

Exp. No.	R_u (EIS) / Ω	R_u / Ω	E^0 / V	C_{dl} / μF cm^{-2}	L_{Glo}
1	61	56	0.527	14.8	1.09e-8
2	66	59	0.558	18.8	1.65e-8
3	55	44	0.567	20.9	2.05e-8
4	63	53	0.559	21.4	2.22e-8
5	63	49	0.542	21.3	1.88e-8
6	54	38	0.531	21.1	2.19e-8
7	71	63	0.601	20.2	2.01e-8
8	53	38	0.585	20.7	1.95e-8
9	58	48	0.586	20.3	1.63e-8
10	85	72	0.589	24.6	2.50e-8

Table 3.3: The parameters recovered from the 10 repeats of the 1.0 mM Fc experiment using the FR3 model and the time-domain method. For comparison, experimentally measured (via EIS) values of R_u are included.

The results of parameter optimisation using the time-domain method with the FR3 model on the 10 repeats of the $Fc^{0/+}$ experiment at 1.0 mM are given in Table 3.3. In this case, there is very good agreement between the results from the time-domain optimisation and the results from frequency-domain optimisation obtained

using Nimrod by our collaborators at Monash (not included). Variation in E^0 from experiment to experiment is to be expected due to the use of a platinum quasi-reference electrode, which has a non-constant potential. In addition, there is also fairly good agreement between the recovered values of R_u and those measured experimentally via EIS.

Exp. No.	R_u / Ω	E^0 / V	k^0 / cm s^{-1}	C_{dl} / μF cm^{-2}	α	L_{Glo}
1	38	0.527	0.45	15.2	0.51	1.05e-8
2	55	0.558	1.76	18.9	0.54	1.65e-8
3	41	0.567	2.84	20.9	0.54	2.05e-8
4	53	0.559	5.71	21.6	0.00	2.22e-8
5	49	0.542	14.1	21.4	0.65	1.88e-8
6	36	0.531	162	21.0	0.98	2.19e-8
7	61	0.601	3.62	20.3	0.72	2.01e-8
8	37	0.585	8.33	20.7	0.57	1.95e-8
9	45	0.586	3.27	20.4	0.80	1.63e-8
10	67	0.589	1.56	24.6	0.49	2.50e-8

Table 3.4: The parameters recovered from the 10 repeats of the 1.0 mM Fc experiment using the QR5 model and the time-domain method.

In contrast, the results of fitting the QR5 model to the 1.0 mM data using the same time-domain method are shown in Table 3.4. Several comparisons are immediate. Firstly, there is absolutely no variation in the values of E^0 reported by each model in Table 3.3 (FR3) and Table 3.4 (QR5). This would come as no surprise to an experienced operator, as there is almost no way to compensate for a change in E^0 by a balancing change of the other four free parameters. In the case of this model selection problem, neither the QR nor FR models show any advantage for identification of E^0. In addition, values of C_{dl} are quite similar in both cases,

although those obtained using QR5 are marginally higher for most experiments. Again, variations in the other parameters do not affect the non-Faradaic regions of the current response, so it is possible to obtain a fairly accurate estimate of C_{dl} simply by matching to these. The small variation is probably accounted for by the fact that the background current is not entirely constant even in the high concentration experiments, so the parameter-fitting algorithm is able to match it within a range of values, and being allowed to vary all five parameters, it prefers the slightly higher values. The most notable difference between the three common parameters is in the values reported for R_u. Variations in this parameter can be compensated for by changes in the values of k^0 and α, as we have seen while applying the heuristic method for parameter optimisation in the previous chapter. It is perhaps unsurprising that there would be more variation in R_u now that both k^0 and α are allowed to vary as well, but the values returned from the QR5 model are all consistently lower than both those from the FR3 model and those measured using EIS.

Finally we note that in this case, values of α appear to have no correlation whatsoever, taking values ranging from 0.00 to 0.98 (out of a possible range of $0 \leq \alpha \leq 1$), and similarly k^0 ranges over more than an order of magnitude, even ignoring the outlying result from experiment six. These two parameters, k^0 and α, are the ones we have included in order to model the $Fc^{0/+}$ process as quasi-reversible, yet over 10 experiments conducted under as close to identical conditions as could be arranged, there appears to be no consistency from one experiment to the next in the resulting estimated parameter values. This already begins to suggest that using the QR5 model may be somewhat inappropriate for this particular reaction.

The other key point to highlight is that values of L_{Glo} are all lower when fitting QR5. This is, of course, completely logical: we are adding in two extra degrees of

freedom to the search space, and this search space is designed to include $\alpha = 0.5$ and an upper bound for k^0 high enough to be considered well past the reversible limit, and hence equivalent to the FR3 fixed value of $k^0 = 1000$cm s^{-1}. As a result, the L_{Glo} value from FR3 would be an upper bound for that from QR5. At the same time, this suggests a potential problem: simply having an algorithm select which model to use based on comparison between minimal objective function values would mean that the model with more free parameters would always be chosen, provided this condition of the previously fixed values of the extra parameters being inside the updated search space is met.

Exp. No.	R_u / Ω	E^0 / V	k^0 / cm s^{-1}	C_{dl} / μF cm^{-2}	α	L_{Glo}
1	61	0.527	4.70	15.2	0.00	1.13e-8
2	66	0.558	13.6	19.2	0.00	1.73e-8
3	55	0.567	69.3	21.3	0.90	2.28e-8
4	63	0.559	19.4	21.8	0.00	2.39e-8
5	63	0.541	2.21	22.3	0.00	2.45e-8
6	54	0.531	98.9	21.7	0.41	2.67e-8
7	71	0.600	17.7	20.6	0.00	2.13e-8
8	53	0.585	71.5	21.2	0.83	2.34e-8
9	58	0.586	14.9	20.7	0.00	1.82e-8
10	85	0.589	29.8	25.1	0.00	2.77e-8

Table 3.5: The parameters recovered from the 10 repeats of the 1.0 mM Fc experiment using the QR4 model (R_u fixed at experimentally measured values) and the time-domain method.

As a test, a QR4 model with R_u fixed at the EIS values was also fitted, with the results as in Table 3.5. Again we notice an excellent agreement in the values of E^0 with those from the FR3 and QR5 models, and C_{dl} values that appear to

be only slightly higher again than those resulting from use of the QR5 model. However, once again the k^0 and α exhibit considerable experiment-to-experiment variation, in addition to showing almost no resemblance to those reported in Table 3.4 resulting from use of the QR5 model. The values for k^0 vary by an order of magnitude in some experiment-to-experiment comparisons, and are all above a cut-off level that if one were using an heuristic method, would be called the reversible limit, above which further variation would be meaningless. Similarly, in terms of lack of meaning, α again appears to be able to take any value in the interval [0,1], though the algorithm in its current form often returns values close to the boundaries of the search space. Once again, values of L_{Glo} are not particularly different from those obtained using FR3 or QR5: of course in all cases they are larger than QR5 for the same reason as before, though interestingly they are also all higher than the L_{Glo} values from using the FR3 model as well, suggesting that the removal of the freedom for R_u to vary has a much higher impact on the minimisation of the objective function than the inclusion of the two extra parameters k^0 and α.

When we move to the 0.1 mM data, some trends become a lot easier to see. A large part of this is due to the background current, which at the lower concentration has a relatively much larger contribution to the overall current. Looking at Figure 3.2, it is clear to the eye that this background current is not constant throughout the experiment, and as such the inability to accurately model it with a single value of C_{dl} exaggerates inaccuracies in the estimates of k^0, R_u and α.

The results reported in Table 3.6 were obtained from fitting the FR3 model to the 0.1 mM $Fc^{0/+}$ data using the time-domain method. As anticipated, due to the flawed model of the capacitive component of the current having greater significance at this concentration, the values of R_u generally do not show as good agreement

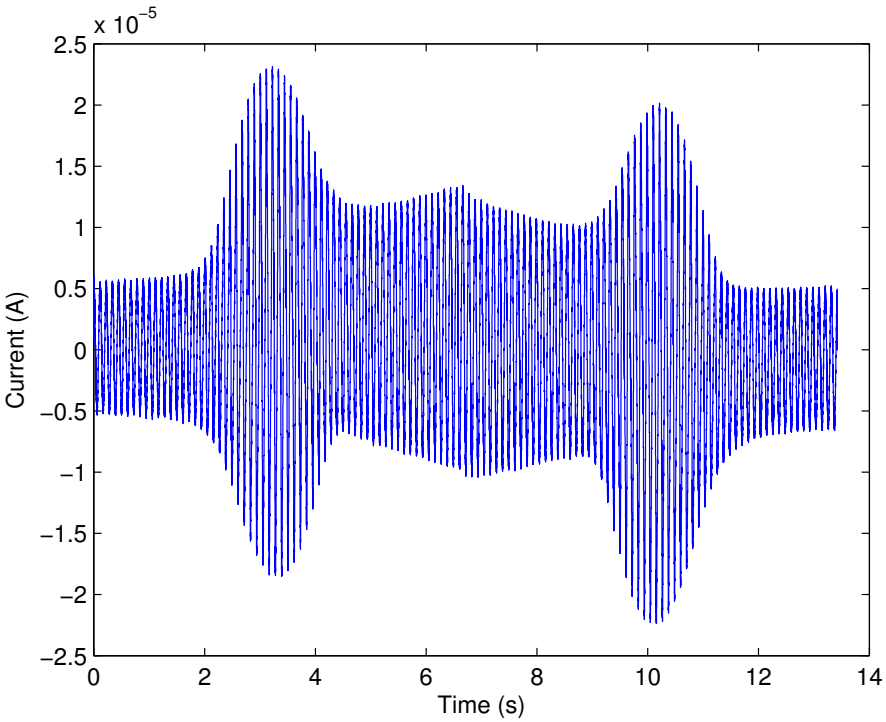

Figure 3.2: The voltammogram from the first of the 0.1 mM $Fc^{0/+}$ experiments. Of particular note is the obviously non-constant background current.

with EIS-measured values as in the 1.0 mM case. The values of C_{dl} represent the optimal constant approximation for the background current.

Attempting to fit the QR5 model to the 0.1 mM experiments gives the results shown in Table 3.7. As was the case with the 1.0 mM data, the reported values for E^0 are virtually identical using either of the FR3 or QR5 models, and C_{dl} values are similarly close. In this case, however, there is significant experiment-to-experiment variation in the values of R_u and k^0, with the latter now varying by, in extreme cases, up to almost two orders of magnitude. The reasoning behind these variations is the same as before, though with the added factor of the nonlinear background current included they are now far more pronounced. In particular, the combination

Exp. No.	R_u (EIS) / Ω	R_u / Ω	E^0 / V	C_{dl} / μF cm^{-2}	L_{Glo}
1	66	75	0.587	24.3	1.84e-8
2	61	87	0.632	22.3	1.53e-8
3	56	87	0.635	24.5	2.05e-8
4	54	79	0.621	18.8	1.10e-8
5	51	93	0.629	19.8	1.17e-8
6	50	47	0.630	23.7	1.19e-8
7	37	45	0.630	23.2	1.40e-8
8	64	62	0.638	21.5	1.35e-8
9	49	65	0.643	23.2	1.38e-8
10	56	96	0.647	24.4	1.58e-8

Table 3.6: The parameters recovered from the 10 repeats of the 0.1 mM Fc experiment using the FR3 model and the time-domain method. For comparison, experimentally measured (via EIS) values of R_u are included.

of poor background current modelling combined with uncertainty in the value of k^0 has resulted in the predicted R_u values displaying almost no correlation with the EIS-measured values. To an experienced electrochemist, $\alpha \geq 0.9$ also sets off alarm bells, as in a truly quasi-reversible system values closer to 0.5 are expected. Finally, we again note that L_{Glo} values are very similar between results from fitting the FR3 and QR5 models, though again slightly lower for QR5.

For completeness, the results of using the time-domain method to fit the QR4 model with R_u set to EIS-measured values are presented in Table 3.8. As we would by now expect, E^0 and C_{dl} are once again almost identical between all three models. When comparing the results of fitting QR4 and QR5, we can see that although at the reported level of accuracy there is no variation in the value of the

Exp. No.	R_u / Ω	E^0 / V	k^0 / cm s^{-1}	C_{dl} / μF cm^{-2}	α	L_{Glo}
1	71	0.588	2.18	24.3	0.92	1.84e-8
2	0	0.632	0.46	22.4	0.92	1.52e-8
3	67	0.635	1.47	24.5	0.92	2.04e-8
4	0	0.621	0.32	19.1	0.92	1.09e-8
5	2	0.629	0.39	19.9	0.93	1.16e-8
6	84	0.630	23.84	23.8	0.96	1.19e-8
7	33	0.630	1.48	23.2	0.94	1.40e-8
8	40	0.638	0.75	21.4	0.93	1.35e-8
9	18	0.644	0.66	23.2	0.94	1.37e-8
10	184	0.647	3.02	24.6	0.95	1.58e-8

Table 3.7: The parameters recovered from the 10 repeats of the 0.1 mM Fc experiment using the QR5 model and the time-domain method.

objective function, L_{Glo}, there is significant variation in both R_u and k^0. This already suggests that when fitting the constant C_{dl} model to the 0.1 mM data, there are significant flat contours in the objective function surface when varying R_u and k^0.

3.3.3 Parameter recovery: frequency-domain

To conclude the analysis of the data, we will include results obtained by our collaborators at Monash on the 72 Hz data at both 0.1 and 1.0 mM, and 9 Hz data at 1.0 mM. We will use the results from the 0.1 mM experiments to illustrate the issue of underparameterisation in the background current, and then those from the 1.0 mM experiments as an example of how much reported values of k^0 can vary

Exp. No.	R_u / Ω	E^0 / V	k^0 / cm s^{-1}	C_{dl} / μF cm^{-2}	α	L_{Glo}
1	66	0.588	3.2	24.3	0.91	1.84e-8
2	61	0.632	0.72	22.4	0.93	1.52e-8
3	56	0.635	1.3	24.5	0.92	2.04e-8
4	54	0.621	0.54	19.0	0.94	1.09e-8
5	51	0.629	0.48	20.0	0.94	1.16e-8
6	50	0.630	3.6	23.7	0.94	1.19e-8
7	37	0.630	1.3	23.3	0.94	1.40e-8
8	64	0.639	1.1	21.4	0.94	1.35e-8
9	49	0.644	0.85	23.2	0.95	1.37e-8
10	56	0.647	0.63	24.6	0.94	1.58e-8

Table 3.8: The parameters recovered from the 10 repeats of the 0.1 mM Fc experiment using the QR4 model (R_u fixed at experimentally measured values) and the time-domain method.

between sets of experiments.

At 0.1 mM, the most likely cause of experiment-to-experiment inconsistency and, in the case of R_u, lack of agreement between fitted and EIS-measured values, is the poor modelling of the background current as a constant capacitive effect. In a previous study [17], our collaborators have proposed a heuristic form for a potential-dependent capacitance, $C_{dl}(E)$, as

$$C_{dl}(E) = C_{dl0} + C_{dl2}\left(E(t) - E_{Cdl}\right)^2 + C_{dl3}\left(E(t) - E_{Cdl}\right)^3, \tag{3.3}$$

where again the notation $E(t)$ means

$$E(t) = E_{applied}(t) - I_{tot}R_u, \tag{3.4}$$

C_{dl0}, C_{dl2} and C_{dl3} are constant coefficients, and E_{Cdl} is the fourth constant of

the cubic, included in this way for computational reasons, to avoid our collaborators' software reporting negative values of capacitance. While this model has no published mathematical justification from a modelling point of view, it is intuitive from Figure 3.2 that a polynomial dependence of capacitance upon the potential might be more appropriate than a constant, and this proposed model has seen some success in applications to other experimental systems [9].

Exp. No.	R_u (EIS) / Ω	R_u / Ω	E^0 / V	C_{dl} / μF cm^{-2}	L_{Nim}
1	66	60	0.584	19.4	0.129
2	61	54	0.629	18.6	0.124
3	56	46	0.630	19.6	0.131
4	54	48	0.617	16.1	0.122
5	51	45	0.627	16.9	0.124
6	50	47	0.629	19.1	0.128
7	37	24	0.629	18.7	0.122
8	64	55	0.637	17.3	0.124
9	49	37	0.641	19.1	0.128
10	56	43	0.644	20.3	0.131

Table 3.9: The parameters recovered from the 10 repeats of the 0.1 mM Fc experiment at 72 Hz using the FR3 model and the frequency-domain method with Nimrod software.

Results of fitting the FR3 model are shown in Table 3.9. The objective function, L_{Nim}, is defined in exactly the same way as in Equation (2.37) in the previous chapter.

For comparison, Table 3.10 shows the results of fitting a model designated as FR6 to the same 0.1 mM 72 Hz data. FR6 represents a model with background current

Exp. No.	R_u (EIS) Ω	R_u Ω	E^0 V	E_{Cdl} V	C_{dl0} μF cm^{-2}	C_{dl2} μF cm^{-2} V^{-2}	C_{dl3} μF cm^{-2} V^{-3}	L_{Nim}
1	66	63	0.584	0.14	13.9	5.5	1.2	0.052
2	61	57	0.629	0.25	14.0	6.6	1.4	0.041
3	56	48	0.630	0.26	14.4	7.3	1.4	0.043
4	54	50	0.617	0.36	12.8	7.2	1.9	0.037
5	51	47	0.627	0.32	13.1	6.4	2.5	0.039
6	50	49	0.629	0.35	15.4	7.1	2.2	0.048
7	37	25	0.629	0.36	15.2	6.8	3.0	0.037
8	64	58	0.637	0.31	13.7	5.5	2.7	0.037
9	49	40	0.641	0.36	15.5	7.6	2.3	0.037
10	56	46	0.644	0.33	15.9	7.0	2.5	0.037

Table 3.10: The parameters recovered from the 10 repeats of the 0.1 mM Fc experiment at 72 Hz using the FR6 model and the frequency-domain method with Nimrod software.

modelled as a function, as defined in Equation (3.3). When comparing the results in this table with those in Table 3.9, we can see that the reported R_u values are closer to EIS values when fitting FR6 than when fitting FR3, and that L_{Nim} is noticeably lower. While it is not unexpected that L_{Nim} would be lower, for the same reasons as previously when one model is a special case of the other, looking at Figure 3.3, we can see by eye that the FR6 model does in fact fit the data better than the FR3 model when the harmonics are considered. This suggests that in cases such as our series of 0.1 mM $Fc^{0/+}$ experiments, modelling of the capacitive portion of the current as a constant value, C_{dl}, can be considered as under-parameterisation of the model, when compared with using a polynomial such as that suggested in Equation (3.3).

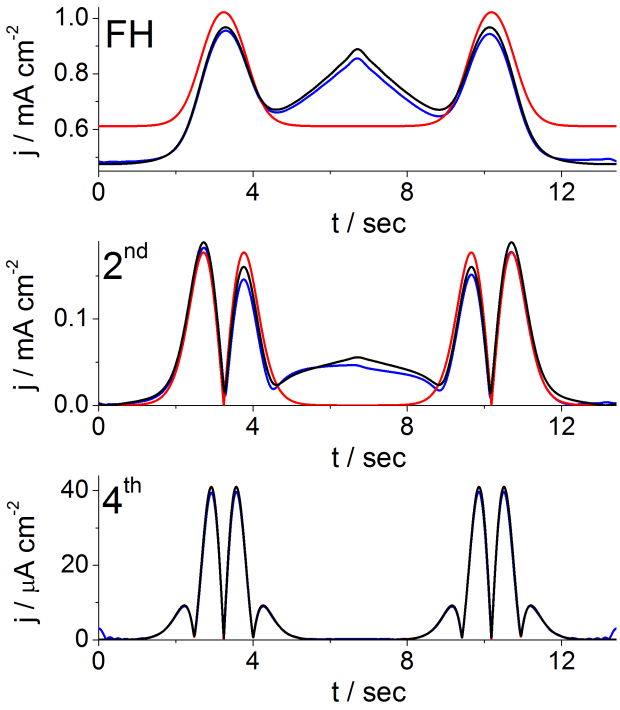

Figure 3.3: A comparison of the effect of the choice of background current model on the shape of the 1st, 2nd and 4th harmonics, using the data from experiment 5 at 0.1 mM and 72 Hz. The experimental data are represented by the blue line, constant background simulated using the FR3 model by the red line, and polynomial background consistent with Equation (3.3) and the FR6 model by the black line.

Our final set of results will be two different sets of experiments on the same system, namely 1.0 mM $Fc^{0/+}$ at each of 9 and 72 Hz, and will serve to highlight the vastly different ranges of parameters it might be possible to report using the QR5 model if one had access to only one of these sets of data.

The results from the 9 Hz data are given in Table 3.11. By themselves, these results appear quite consistent, although when compared with the results presented in Table 3.4, we see substantial variation in reported values of k^0 and α. In the

Exp. No.	R_u / Ω	E^0 / V	k^0 / cm s^{-1}	C_{dl} / μF cm^{-2}	α	L_{Nim}
1	50	0.527	1.3	14.8	0.53	0.013
2	60	0.558	3.0	18.0	0.50	0.014
3	46	0.567	2.9	22.1	0.50	0.015
4	55	0.559	3.0	22.9	0.48	0.015
5	53	0.541	2.3	23.5	0.48	0.018
6	43	0.531	3.0	23.8	0.48	0.016
7	65	0.600	1.9	21.5	0.48	0.014
8	38	0.584	1.0	23.9	0.51	0.023
9	47	0.587	1.4	21.9	0.51	0.014
10	76	0.589	2.5	24.6	0.48	0.017

Table 3.11: The parameters recovered from the 10 repeats of the 1.0 mM Fc Experiment at 9 Hz using the QR5 model and the frequency-domain method with Nimrod software.

case of α, proximity to 0.5 is a numerical artefact of the method by which Nimrod optimises parameters. A search space symmetrical about $\alpha = 0.5$ was used, but our collaborators at Monash found that if the search space centred around a different value, α would converge to that value instead. This is most likely programmed in as a solution to the parameter reaching both extremes of its allowed range during the course of the optimisation, though this is not confirmed. While k^0 values also appear much more consistent than those from the time-domain method, variation by a factor of up to three is still quite significant, and in all cases, reported values are still above the heuristically-determined "reversible limit". Regardless of the choice of method, R_u appears to be slightly low when compared with EIS-measured values (see Table 3.3). Finally, E^0 values are almost identical between the time-domain and frequency-domain methods, and C_{dl} values also show good agreement.

Exp. No.	R_u / Ω	E^0 / V	k^0 / cm s^{-1}	C_{dl} / μF cm^{-2}	α	L_{Nim}
1	57	0.503	49	12.8	0.51	0.041
2	63	0.554	57	16.0	0.49	0.048
3	50	0.568	62	14.9	0.49	0.050
4	59	0.547	60	17.5	0.50	0.056
5	59	0.545	41	15.4	0.50	0.058
6	48	0.534	45	17.7	0.49	0.057
7	67	0.596	45	17.1	0.50	0.053
8	47	0.580	60	16.3	0.49	0.054
9	53	0.585	57	17.1	0.48	0.054
10	82	0.579	33	19.4	0.50	0.065

Table 3.12: The parameters recovered from the 10 repeats of the 1.0 mM Fc Experiment at 72 Hz using the QR5 model and the frequency-domain method with Nimrod software.

It is when the results at 9Hz from Table 3.11 are compared with the results of the 72 Hz data, presented in Table 3.12, however, that the most interesting comparison can be made. The main thing to notice is that we suddenly see an increase in the k^0 values of more than an order of magnitude, and once again within the context of only the 72 Hz data, these values are very consistent. This example shows the power of AC voltammetry as an investigative technique compared with traditional DC methods. Reactions whose kinetics are close to the fully-reversible regime are very sensitive to increases in the rate of change of the applied potential, which can be altered by varying either the scan rate, ν, or much more easily, the frequency, f, of the AC perturbation. If the reaction under investigation is so fast that compared to the rate of change of applied potential reactions occur "instantly", increases in this rate should continue to result in changes to the measured current response, until the point is reached where the rate of reaction becomes the limiting factor.

3.3.4 Confidence intervals using bootstrapping

We have observed in several cases that there could be an issue of over-parameterisation when fitting the 5-parameter quasi-reversible model to the Fc reaction. As a means of investigating this, we make use of the technique of bootstrapping [35] to generate confidence intervals for our parameter estimates. For clarity, we will compare the results of applying this technique not only to an Fc experiment already analysed in this chapter, but also to an $[Fe(CN)_6]^{3-/4-}$ experiment from the previous chapter.

The principle of the bootstrapping technique that we use is to resample the residuals from a parameter optimisation in order to generate surrogate data sets by essentially re-distributing the existing experimental noise randomly throughout

the data.

In practice, given an experimental data set, I^M, we generate best-fit simulated data, I^S, which then gives us for each discrete time measurement point j

$$I_j^M = I_j^S + r_j, \tag{3.5}$$

where the r_j represent the residuals. We then generate new data sets I^G via

$$I_j^G = I_j^S + r_k, \tag{3.6}$$

where k is selected randomly with replacement from the range of possible values of j. This allows the construction of as many data sets as required, and by then performing a parameter optimisation on each data set, provided we have repeated the operations a sufficient number of times, we are able to obtain reliable bounds on parameter confidence intervals.

For our particular situation, there is one further complication. As has already been discussed, for the 0.1 mM data in particular, the nonlinearity of the background current is significant enough that assuming it to be constant will cause some bias in the residuals due to unavoidable inaccuracies in the non-Faradaic regions. As a result, when dealing with these sets of data, in particular, we will fit our initial set of data, I^S, with a background current model equivalent to that in Equation (3.3), given by

$$C_{dl}(E) = C_{dl0} + C_{dl1}E(t) + C_{dl2}E(t)^2 + C_{dl3}E(t)^3. \tag{3.7}$$

Subsequent fits to the generated data sets, I^G, are then performed using the same values of C_{dl1}, C_{dl2}, and C_{dl3} as were obtained for I^S, but with C_{dl0} allowed to vary.

We begin by testing the bootstrapping method on the $[Fe(CN)_6]^{3-/4-}$ data from the previous chapter. Table 3.13 shows the results of optimising over 1000 generated

	E^0 / V	k^0 / cm s^{-1}	α	C_{dl} / μF cm^{-2}
Mean	0.213	0.0096	0.52	24
Median	0.213	0.0096	0.52	24
Lower interval	0.213	0.0095	0.52	24
Upper interval	0.213	0.0096	0.53	24

Table 3.13: Results from 1000 iterations of the bootstrapping algorithm on experiment 7 of the 1.0 mM $[Fe(CN)_6]^{3-/4-}$ data set using the time-domain parameter fitting method. The lower and upper limits are for a 95% confidence interval. R_u was fixed at the experimentally measured value of 6 Ω, as we saw in the previous chapter that defining an exact value was neither meaningful or possible, and the experimental values were a suitable approximation.

data sets from the 7th $[Fe(CN)_6]^{3-/4-}$ experiment using the QR4 model, with 1000 chosen as a sufficient number of iterations to stabilise the bounds on the confidence interval. As we can see, the 95% confidence intervals are all extremely narrow, suggesting a high degree of reliability in the reported parameter values. In this case, attempting to fit a fully-reversible model such as FR3 produces nonsensical results.

In contrast, applying the boostrapping algorithm to the first experiment of the 0.1 mM Fc series produces results summarised in Table 3.14. As was explained above, the model fitted had five free parameters and three fixed ones for the nonlinear background current, making it a hybrid of the QR5 and QR8 models. Histograms showing these results are presented in Figure 3.4. It is immediately visible that the confidence intervals for k^0 and α from the 1000 runs of the bootstrapping process on the Fc data set are relatively large when compared with the confidence intervals generated for the parameters on the $[Fe(CN)_6]^{3-/4-}$ experiment. In particular, the

	R_u / Ω	E^0 / V	k^0 / cm s^{-1}	α	C_{dl} / μF cm^{-2}
Mean	139	0.585	2.03	0.52	23
Median	138	0.585	1.82	0.53	23
Lower interval	110	0.585	0.94	0.01	23
Upper interval	173	0.585	4.53	0.95	23

Table 3.14: Results from 1000 iterations of the bootstrapping algorithm on experiment 1 of the 0.1 mM Fc data set at 9 Hz using the time-domain method. The lower and upper limits are for a 95% confidence interval.

confidence interval for α covers almost the entire range of permissible values, and these wide intervals indicate that neither of these parameters can be estimated with any degree of certainty based on this experiment. While C_{dl} and E^0 both appear to be accurately estimatable, running a 5-parameter optimisation on the Fc experiment not only provides little information about k^0 and α, but the resulting effect on the reported value of R_u in the presence of significant background current also makes this parameter difficult to identify.

	R_u / Ω	E^0 / V	k^0 / cm s^{-1}	α	C_{dl} / μF cm^{-2}
Mean	60	0.600	11.8	0.58	18
Median	60	0.600	10.5	0.55	18
Lower interval	55	0.600	1.44	0.27	18
Upper interval	61	0.600	42.4	1.00	18

Table 3.15: Results from 1000 iterations of the bootstrapping algorithm on experiment 7 of the 1.0 mM Fc data set at 9 Hz using the time-domain method. The lower and upper limits are for a 95% confidence interval.

An even clearer picture is provided when this analysis is repeated on the higher

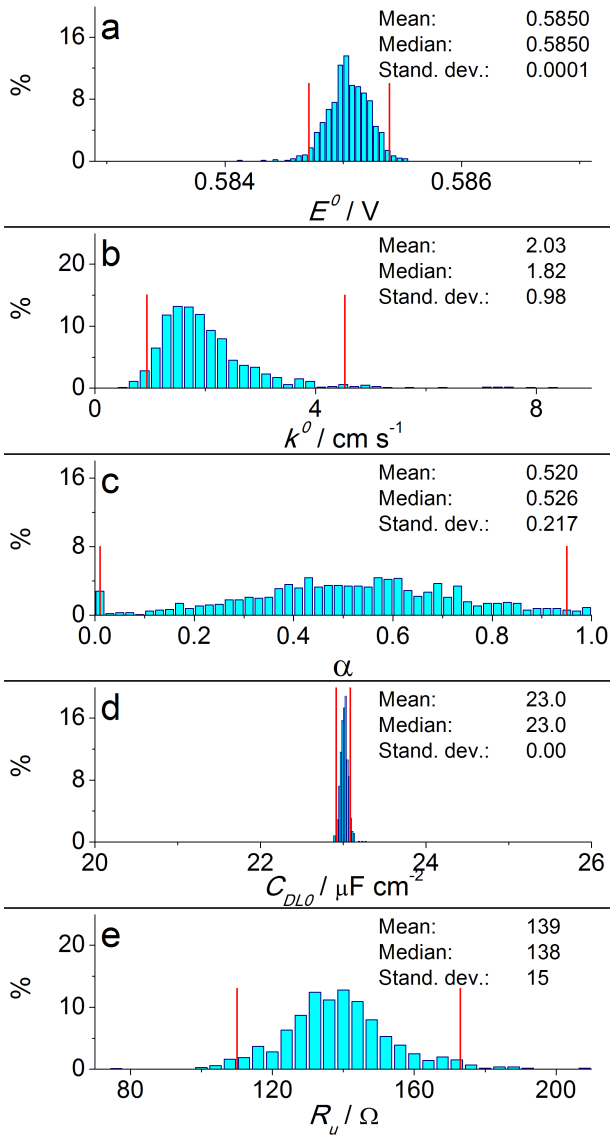

Figure 3.4: Histograms of the distributions of parameters recovered from the 1000 iterations of the boostrapping technique applied to experiment 1 of the 0.1 mM Fc data at 9 Hz, fitting a QR5/8 model (see text) using the time-domain method. Vertical red lines indicate the limits of the 95% confidence interval.

concentration data, where in this case experiment 7 was used. Confidence intervals are given in Table 3.15, and the results are displayed in Figure 3.5. Just as for the

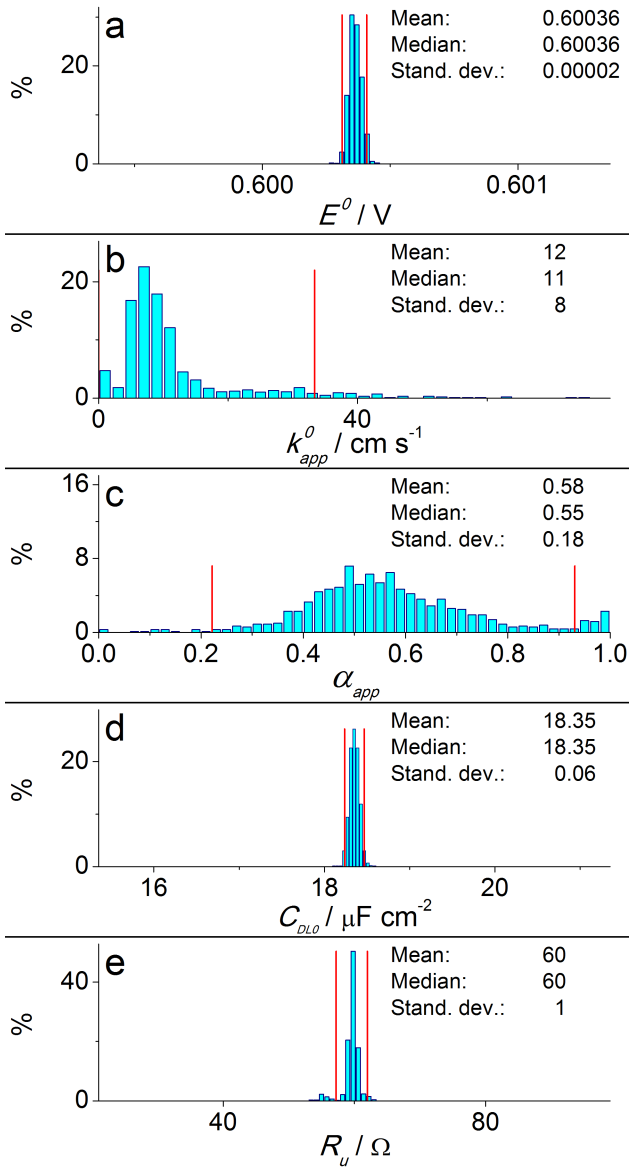

Figure 3.5: Histograms of the distributions of parameters recovered from the 1000 iterations of the boostrapping technique applied to experiment 7 of the 1.0 mM Fc data at 9 Hz, fitting a QR5/8 model (see text) using the time-domain method. Vertical red lines indicate the limits of the 95% confidence interval.

low concentration experiment, E^0 and C_{dl} can be estimated with a high degree of

confidence. We also see that with the background current nonlinearity being less of a factor, as has been remarked on in Sections 3.3.2 and 3.3.3, we also obtain a much narrower confidence interval for R_u, suggesting that this parameter is also identifiable. Again, though, confidence intervals for k^0 and α cover a large range of possible values. The value of k^0 appears to be able to take almost any value with $k^0 \geq 1$ cm s^{-1}, with the limits on the 95% confidence interval differing by more than a factor of 10. Similarly, α takes any value in the range $0 \leq \alpha \leq 1$, although with a slight preference for the upper end of the interval.

The insight offered from this analysis on the lack of identifiability of k^0 and α suggests that including these parameters through the use of the QR5 model might be of little benefit when compared with simply using the FR3 model. This is particularly evident when a single experiment might be capable of producing such variable parameter values simply as a result of variations in the random noise due to measurement errors.

3.3.5 Insights from contour plots

Some further explanation can be offered by observing contour plots generated by sampling the k^0-R_u plane of the objective function surface. These plots were generated at Monash, using Nimrod to repeatedly simulate data using a discrete mesh for k^0 and R_u values, and at each mesh point calculating the objective function L_{Nim} versus experimental data.

One example of the results of this method is pictured in Figure 3.6, with details on the mesh size and other details of the production given in the caption. Unsurprisingly, after seeing the results of both the parameter fitting and the confidence interval generation from the bootstrapping algorithm, we clearly see that at 72 Hz

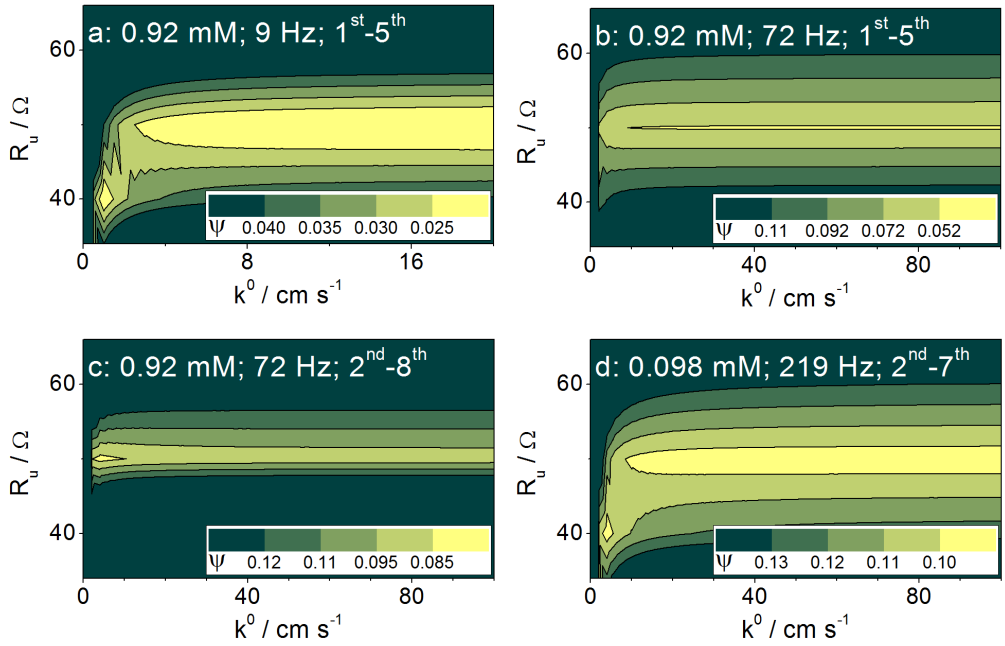

Figure 3.6: Contour plots obtained by calculating L_{Nim} at different values of k^0 and R_u against experiment 3 of the 1.0 mM 9 Hz Fc data (panel a), experiment 1 of the 1.0 mM 72 Hz data (panels b,c), and a single experiment run at 219 Hz and 0.1 mM Fc (panel d). L_{Nim} was calculated using harmonics 1-5 for panels (a,b), harmonics 2-8 for panel (c), and harmonics 2-7 for panel (d). In both cases R_u was sampled over the range 0-100 Ω at 10 Ω intervals. For the 9 Hz data, k^0 was sampled over the range 0-5 cm s^{-1} at 0.1 cm s^{-1} intervals, and for the 72 Hz and 219 Hz data it was sampled over the range 0-100 cm s^{-1} at 2 cm s^{-1} intervals. The other parameters were held fixed at the values recovered from the Nimrod frequency-domain optimisation (see Tables 3.11 and 3.12).

(panels b and c) there is a well-defined value of R_u but k^0 can take almost any value between some lower limit around $k^0 = 9$ cm s^{-1} and the end of the range provided in the figure, which was 100 cm s^{-1} in those panels. At 9 Hz (panel a) results are similar, with a slightly lower bound of about $k^0 \geq 3$ cm s^{-1}, although in this case there is also a local minimum located at a lower value of R_u around 40 Ω,

which may help to explain the low value of 41 Ω reported for experiment 3 in Table 3.4 compared with the EIS-measured value of 55 Ω, and a less well-defined value for this parameter even in the larger area where the objective function, L_{Nim}, is smallest. A similar story holds true at 219 Hz (panel d) for the low concentration data, where again there is an area of minimal variation in L_{Nim} for $k^0 \geq 9$ cm s^{-1}, along with an isolated local minimum around $k^0 = 2$ cm s^{-1} and $R_u = 40$ Ω. In all panels, this lack of identifiability of k^0 is consistent with our other observations, and provides further evidence for a conclusion about the appropriateness of fitting the QR5 model as opposed to the FR3 model.

3.3.6 A brief comment about further dangers of over-parameterisation

During the course of preparation of the paper on which this chapter is based, one further surprising result emerged. Due to an early communication mistake and an unrelated typographical error at Monash, both laboratories performed the parameter estimation exercise using incorrect values (0.94 mM at Oxford, instead of 0.92 mM) of the concentration for the high-concentration experiments. A roughly 2% error in the concentration would be expected to result in a proportional error in the current response produced during simulations, and in a truly quasi-reversible regime, this would have little impact on reported parameter values. However in the case of this study of the $Fc^{0/+}$ process, this error resulted in reported values of k^0 from fitting the QR5 model to the 9 Hz data being more than an order of magnitude lower than when the correct concentration was used. This is perhaps unsurprising given the lack of sensitivity of the current response to increases in k^0 that we have demonstrated throughout this chapter, but it still serves as a useful lesson. In an experimental setting, it cannot be guaranteed that values used for

parameters such as the concentration of the electroactive species or the electrode surface area will be measurable to such a high degree of accuracy, so given that such small errors in these measurements can result in such large changes in reported estimates of the value of k^0 when using a quasi-reversible model, this serves as a further recommendation that modelling this process as fully-reversible is a much more appropriate choice.

3.4 Conclusions

We have shown that for a system with such rapid kinetics as the $Fc^{0/+}$ mechanism, a wide range of k^0 and α values can be reported depending on the experimental setups used. While a simple comparison of objective function values might naively be thought to suggest that the quasi-reversible model is more appropriate, further evidence obtained using statistical techniques such as bootstrapping, and substantiated by contour plots of the objective function surfaces, in fact provide a strong argument that the inclusion of these extra parameters in the modelling process is meaningless for such systems. When coupled with the widely varying values of k^0 reported through the literature, these results imply that care must be taken over the choice of model when studying processes close to the reversible limit, and that it is often more appropriate to use a model of fully-reversible kinetics, along with a report of only a lower-bound for the rate constant, k^0. It is worth noting that this model selection problem is an area of much current research, particularly using the tools of Bayesian statistics such as the Akaike information criterion, and will be discussed again in the future work section in Chapter 6.

Chapter 4

Coupled reactions: a case study of the EC mechanism

In Chapters 2 and 3, we have considered a single electron transfer process, which is the simplest possible example of an electrochemical reaction. In practice, reaction mechanisms are often more complicated. The product of the initial electron transfer may itself be electroactive or, alternatively, may react chemically with another species present in the solution. The product or products of the following reaction may in turn be electroactive, and in this way a multi-step reaction can be conceived. Using a simple designation of "E" to represent an electron transfer reaction and "C" to represent a chemical reaction with no electron transfer, reaction mechanisms can be described as, for example, E, EC, CE, EE, ECE, EEC and so on. Perhaps the most straightforward coupled reaction is the EC mechanism, consisting of a heterogeneous electron transfer reaction followed by a homogeneous solution-phase chemical reaction involving the product. In this chapter we will consider the additional complexity involved in the analysis, and attempted recovery, of kinetic parameters from such a reaction.

4.1 Background

An EC reaction proceeds according to

$$\begin{aligned} A &\overset{E^0,k^0,\alpha}{\rightleftharpoons} B + e^-, \\ B &\underset{k_b}{\overset{k_f}{\rightleftharpoons}} C, \end{aligned} \tag{4.1}$$

where k_f and k_b (units s^{-1}) represent the forwards and backwards rates of the chemical reaction, respectively. Considering the work of Chapter 3, we might expect that this mechanism may fall into different regimes depending on whether the "E" step is fully-reversible, quasi-reversible or even irreversible. In addition we can consider the special case of the "C" step where $k_b = 0\ \mathrm{s}^{-1}$, i.e. the chemical reaction is irreversible. We will label these possible cases by E_{FR} for a fully-reversible electron transfer step, E_{QR} for quasi-reversible electron transfer, E_I for irreversible electron transfer, and C_{rev} and C_{irrev} for reversible ($k_b > 0\ \mathrm{s}^{-1}$) and irreversible chemical reactions, respectively.

Previous studies of the EC mechanism have focused mainly on DC cyclic voltammetric techniques. Authors have noted some of the difficulties encountered when attempting to estimate the relevant parameters of the system. One example of such a difficulty is shifting in the potential of the peak current when the electron transfer step is reversible [76], as predicted by the Nernst equation. Another example is the difficulty in distinguishing between an EC reaction and just an E reaction with reversible electron transfer or irreversible electron transfer in the absence of a back-sweep peak, in the cases of slow or rapid chemical reactions, respectively [87].

EC reactions have been categorised by the value of a dimensionless parameter λ

given by

$$\lambda = \frac{k_f RT}{F\nu}, \tag{4.2}$$

which we shall see emerges during the non-dimensionalisation of the equations of the mathematical model in the following section. Small values of λ ($\lambda < 0.1$ according to [11]) correspond to the chemical reaction having little effect over the timescale of the experiment, with the opposite being the case for large values of λ and, in particular for EC_{irrev} reactions, these large values of λ ($\lambda > 5$ [11]) represent the cases where no backwards-sweep peak is detected.

This hints at a strategy which is often used in DC voltammetry investigations into EC reactions. As the rates of the chemical reaction, k_f and possibly k_b, are unknown, a series of experiments will be run at varying scan rates, with the hope of finding a scan rate such that λ falls in the range $0.1 < \lambda < 5$, where determination of the kinetic parameters is possible using either heuristic techniques or numerical simulation software and experiment-theory comparison.

When AC voltammetric techniques are employed instead [20,21,58], the introduction of the second timescale determined by the frequency of oscillation of the sinusoidal perturbation suggests the possibility of developing a more intricate approach to this parameter estimation problem. While the same problems are ultimately encountered when a single experiment is performed, in this chapter we will explore whether the increased sensitivity of these techniques will allow similarly strong or even superior results, when compared with those reported using DC techniques, to be obtained from a smaller number of experiments.

In this chapter, we will begin by setting out a mathematical model and outlining a numerical solution scheme similar to the one developed in Chapter 2 for the E reaction. We will perform simulations in the framework of DC cyclic voltammetry to categorise combinations of k^0 and the rates of reaction k_f and, where relevant,

k_b, in terms of oxidation and reduction peak positions and magnitudes. Following this, we will consider some particular cases of the EC_{rev} and EC_{irrev} mechanisms, and investigate the reliability of our parameter recovery algorithm in the presence of 5% added measurement-error noise in the contexts of both DC voltammetry and AC voltammetry at different frequencies. The use of frequency domain methods will also briefly be considered.

4.2 Methods

The mathematical model and subsequent numerical solution scheme for the EC reaction mechanism are similar to those for the E reaction in Chapter 2, and have also been formulated previously elsewhere [95]. For our three species A, B and C with concentrations given by c_A, c_B and c_C, respectively, we have the equations

$$\frac{\partial c_A}{\partial t} = D_A \frac{\partial^2 c_A}{\partial x^2}, \tag{4.3}$$

$$\frac{\partial c_B}{\partial t} = D_B \frac{\partial^2 c_B}{\partial x^2} - k_f c_B + k_b c_C, \tag{4.4}$$

$$\frac{\partial c_C}{\partial t} = D_C \frac{\partial^2 c_C}{\partial x^2} - k_b c_C + k_f c_B, \quad x > 0,\ t > 0, \tag{4.5}$$

with the extra terms derived from the law of mass action applied to the chemical step of Equation (4.1). The analogous initial and boundary conditions are

$$c_A(x, 0) = c_\infty, \tag{4.6}$$

$$c_B(x, 0) = 0, \tag{4.7}$$

$$c_C(x, 0) = 0, \quad x \geq 0, \tag{4.8}$$

$$c_A \to c_\infty, \tag{4.9}$$

$$c_B \to 0, \tag{4.10}$$

$$c_C \to 0, \quad \text{as} \quad x \to \infty, \quad t > 0, \tag{4.11}$$

and at the electrode surface, $x = 0$, for $t > 0$, the conservation and flux conditions

$$FSD_A \frac{\partial c_A}{\partial x} = -FSD_B \frac{\partial c_B}{\partial x} = I_f, \tag{4.12}$$

$$D_C \frac{\partial c_C}{\partial x} = 0, \tag{4.13}$$

along with the Butler-Volmer condition

$$\begin{aligned} I_f = \; & FSk_0 \left[c_A \exp\left(\frac{(1-\alpha)F}{RT}(E(t) - E^0) \right) \right. \\ & \left. - c_B \exp\left(\frac{-\alpha F}{RT}(E(t) - E^0) \right) \right]. \end{aligned} \tag{4.14}$$

We can see again that with the assumption of equal diffusion coefficients, i.e. when $D_A = D_B = D_C$, we have $c_A + c_B + c_C = c_\infty$, and we can reduce the number of variables by one. To complete the model, our final equations are again

$$E(t) = E_{applied}(t) - I_{tot} R_u, \tag{4.15}$$

$$E_{applied}(t) = E_{start} + \nu t + \Delta E \sin(\omega t), \tag{4.16}$$

$$I_{tot} = I_c + I_f, \tag{4.17}$$

$$I_c = C_{dl} \frac{dE}{dt}. \tag{4.18}$$

We nondimensionalise the remaining equations exactly as in Chapter 2, and note that from Equation (4.4) we obtain the relationships

$$k_f^* = \left[\frac{RT}{F\nu} \right] k_f, \tag{4.19}$$

and

$$k_b^* = \left[\frac{RT}{F\nu} \right] k_b, \tag{4.20}$$

which we can see are exactly the form of λ from the previous section.

In terms of nondimensional variables, with u and v representing the nondimen-

sional concentrations of A and B, respectively, we now have

$$\frac{\partial u}{\partial t} = \frac{\partial^2 u}{\partial x^2}, \tag{4.21}$$

$$\frac{\partial v}{\partial t} = \frac{\partial^2 v}{\partial x^2} - k_f v + k_b(1-u-v), \quad x > 0,\ t > 0, \tag{4.22}$$

with initial and boundary conditions

$$u(x,0) = 1, \tag{4.23}$$

$$v(x,0) = 0, \quad x \geq 0, \tag{4.24}$$

$$u \to 1, \tag{4.25}$$

$$v \to 0, \quad \text{as} \quad x \to \infty, \quad t > 0, \tag{4.26}$$

and for $x = 0$, $t > 0$

$$\frac{\partial u}{\partial x} = -\frac{\partial v}{\partial x} = I_f, \tag{4.27}$$

and

$$\begin{aligned} I_f = \ & k_0 \left[u \exp\left((1-\alpha)(E(t)-E^0)\right) \right. \\ & \left. -v \exp\left(-\alpha(E(t)-E^0)\right) \right]. \end{aligned} \tag{4.28}$$

Completing the nondimensionalised model are

$$E(t) = E_{applied}(t) - I_{tot} R_u, \tag{4.29}$$

$$E_{applied}(t) = E_{start} + t + \Delta E \sin(\omega t), \tag{4.30}$$

$$I_{tot} = I_c + I_f, \tag{4.31}$$

$$I_c = C_{dl} \frac{dE}{dt}. \tag{4.32}$$

The numerical solution method is almost identical to that of Chapter 2. In this case, our Butler-Volmer equation contains both u and v so we must find expressions for both these variables in terms of I_{tot}, and then substitute back into Equation

(4.28). Using the same notation as Chapter 2, with V_j^m representing the finite-difference numerical approximation to $v(x = j\Delta x, t = m\Delta t)$ and $\mu = \Delta t/(\Delta x)^2$, we discretise both Equations (4.23) and (4.24), and use an explicit approximation for the source and sink terms, to give

$$\begin{aligned} &-\theta\mu U_{j-1}^{m+1} + (1+2\theta\mu)U_j^{m+1} - \theta\mu U_{j+1}^{m+1} = \\ &(1-\theta)\mu U_{j-1}^m + (1-2(1-\theta)\mu)U_j^m + (1-\theta)\mu U_{j+1}^m, \end{aligned} \tag{4.33}$$

and

$$\begin{aligned} &-\theta\mu V_{j-1}^{m+1} + (1+2\theta\mu)V_j^{m+1} - \theta\mu V_{j+1}^{m+1} = \\ &(1-\theta)\mu V_{j-1}^m + (1-2(1-\theta)\mu)V_j^m + (1-\theta)\mu V_{j+1}^m \\ &-k_f dt V_j^m + k_b dt U_j^m, \end{aligned} \tag{4.34}$$

for $1 \leq j \leq N-1$, $m \geq 0$. In practice, this approximation is acceptable provided a sufficiently small time-step is used, and we have checked that for the simulations in the remainder of this chapter the numerical solution no longer varies with a further reduction in the time-step or space-step. In addition, the approximation simplifies the solution as the equations are then decoupled. From here on, the Thomas algorithm [72] applies to both Equations (4.33) and (4.34), leading to equations of the form

$$U_0^{m+1} = f_U(I_f^{m+1}), \tag{4.35}$$

$$V_0^{m+1} = f_V(I_f^{m+1}), \tag{4.36}$$

for known functions f_U and f_V, which can be substituted into the discretised version of Equation (4.28), and re-arranged to give

$$g(I_{tot}^{m+1}) = 0, \tag{4.37}$$

for a known function g. Brent's method [22] can then be applied to solve for the total current, I_{tot}^{m+1}, at each subsequent time-step.

4.3 Results

Having set out our mathematical model and numerical solution scheme, we will proceed with a theoretical investigation into parameter estimation in the context of an EC reaction mechanism. We begin by identifying some potentially difficult parameter regimes to consider, using DC voltammetry, and then continue with our investigation into parameter estimation. We employ model-generated data sets which include simulation of the effect of measurement errors that occur during an experiment. For the purposes of this investigation, we consider only the case of $R_u = 0\ \Omega$ and $C_{dl} = 0\ \mu\text{F cm}^{-2}$.

4.3.1 DC results

In this section, we simulate current responses for DC cyclic voltammetry, using a scan rate of $\nu = 0.1\ \text{V s}^{-1}$. We consider five different regimes of k^0, corresponding to fully-reversible ($k^0 = 10^3\ \text{cm s}^{-1}$), quasi-reversible ($k^0 = 10^{-2}\ \text{cm s}^{-1}$) and irreversible ($k^0 = 10^{-6}\ \text{cm s}^{-1}$) electron transfer, along with two intermediate values ($k^0 = 10^{-1}\ \text{cm s}^{-1}$ and $k^0 = 10^{-4}\ \text{cm s}^{-1}$). At each of these, four values of k_f (0.1, 1, 10 and 100 s^{-1}) and five values of k_b (0, 0.1, 1, 10 and 100 s^{-1}) are used, with $k_b = 0\ \text{s}^{-1}$ representing an irreversible chemical reaction step. In the cases of an irreversible chemical reaction and at this scan rate, these values of k_f correspond to $\lambda = 0.026$ ($k_f = 0.1\ \text{s}^{-1}$), $\lambda = 0.26$ ($k_f = 1\ \text{s}^{-1}$), $\lambda = 2.6$ ($k_f = 10\ \text{s}^{-1}$) and $\lambda = 26$ ($k_f = 100\ \text{s}^{-1}$), and so they surround the region in which sensible parameter estimation should be possible according to [11].

For each combination of parameters, we record the ratio of the backwards (reduction, I_{pb}) to forwards (oxidation, I_{pf}) peak currents, the potentials at which they

occur, E_{Ipb} and E_{Ipf}, respectively, the mid-point potential $E_m = (E_{Ipf} + E_{Ipb})/2$ and the peak separation $\Delta E_p = E_{Ipf} - E_{Ipb}$. In addition, at each value of k^0 reference measurements for an E reaction, i.e. electron transfer with no coupled chemical reaction, are provided for comparison.

The potential limits of simulations were varied for the different regimes of k^0. The switching potential, E_{max}, was chosen to be approximately 500 mV greater than the oxidation peak potential of the E reaction at that value of k^0, and the starting and final potentials, E_{start} and E_{end}, were chosen such that a reduction peak was visible. It should be noted that under experimental conditions, such a large variation in potential as was used in, for example, the case of $k^0 = 10^{-6}$ cm s^{-1}, where $-1.0 \text{ V} \leq E \leq 1.0$ V, is often infeasible due to other reactions occuring within that range. As a result, typically when working with such an irreversible electron transfer step, there will be no access to a backwards (reduction in this case) peak at all.

Tables 4.1 and 4.2 summarise data taken from simulations of DC cyclic voltammetry at $k^0 = 10^3$ cm s^{-1} and $k^0 = 10^{-1}$ cm s^{-1}, respectively, which are values at and close to the reversible limit described in Chapter 3. We see unsurprisingly that when $k_b > k_f$, all measurements are very close to the reversible case, which is given in the first row of the tables. When $k_f > 0$ s^{-1} and $k_b = 0$ s^{-1}, as k_f (or λ) is increased, the peak current magnitude ratio decreases as the size of the reduction peak heads to zero, and the position of the oxidation peak becomes more negative, particularly at higher values of k_f, as seen in Figure 4.1. When $k_f \geq k_b > 0$ s^{-1}, the measurements vary with both the ratio $K = k_f/k_b$, where K is the equilibrium constant, and the sum $l = k_f + k_b$. We see that for K constant, increasing l results in a larger ratio and more negative peak potentials, while for a fixed value of k_b, increasing k_f (and hence K) results in a similar behaviour to the $k_b = 0$ s^{-1}

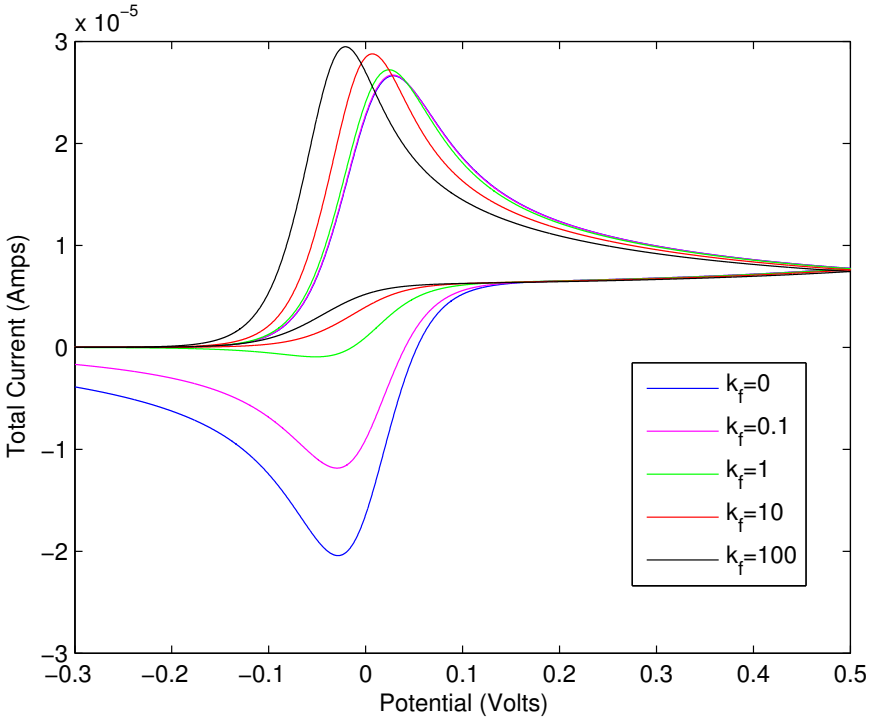

Figure 4.1: The effect of increasing k_f in simulations of DC cyclic voltammetry, with $k^0 = 10^3$ cm s^{-1} and $k_b = 0$ s^{-1}. Other parameters as in the caption of Table 4.1.

k_f (s^{-1})	k_b (s^{-1})	I_{pb}/I_{pf}	E_{Ipf} (mV)	E_{Ipb} (mV)	E_m (mV)	ΔE_p (mV)
0	0	1.06	28.4	-28.5	-0.1	56.8
0.1	0	0.733	28.0	-29.5	-0.7	57.4
0.1	0.1	0.820	28.0	-30.0	-1.0	58.0
0.1	1	1.00	28.0	-29.8	-0.9	57.8
0.1	10	1.05	28.2	-28.9	-0.4	57.0
0.1	100	1.06	28.4	-28.5	-0.1	56.8
1	0	0.318	24.3	-51.5	-13.6	75.8
1	0.1	0.395	24.3	-50.2	-13.0	74.4
1	1	0.743	24.8	-42.7	-9.0	67.6
1	10	1.03	27.0	-31.4	-2.2	58.4
1	100	1.06	28.2	-28.9	-4.0	57.0
10	0	0.264	6.9	N/A	N/A	N/A
10	0.1	0.286	7.1	-174.4	-83.7	181.5
10	1	0.447	8.6	-104.7	-48.1	113.3
10	10	0.893	17.0	-49.6	-16.3	66.6
10	100	1.05	26.2	-31.2	-2.5	57.4
100	0	0.252	-20.9	N/A	N/A	N/A
100	0.1	0.259	20.7	-243.4	-132.0	222.7
100	1	0.317	-19.7	-172.6	-96.2	152.9
100	10	0.632	-11.5	-100.4	-56.0	88.9
100	100	0.993	12.9	-47.6	-17.4	60.6

Table 4.1: Simulated peak height ratios, peak positions and peak separations for DC cyclic voltammetry of an EC reaction model with $k^0 = 10^3$ cm s^{-1}. Other parameters used were $E_{start} = -0.3$ V, $E_{max} = 0.5$ V, $\nu = 0.1$ V s^{-1}, $E^0 = 0$ V, $\alpha = 0.5$, $c_\infty = 1$ mM, $S = 0.07$ cm^2, $D = 2 \times 10^{-5}$ cm^2 s^{-1}, $T = 296$ K, $R_u = 0$ Ω, $C_{dl} = 0$ μF cm^{-2}.

k_f (s^{-1})	k_b (s^{-1})	I_{pb}/I_{pf}	E_{Ipf} (mV)	E_{Ipb} (mV)	E_m (mV)	ΔE_p (mV)
0	0	1.06	30.5	-30.4	0.1	60.9
0.1	0	0.736	30.1	-31.2	-0.5	61.3
0.1	0.1	0.823	30.1	-31.8	-0.8	61.9
0.1	1	1.01	30.1	-31.8	-0.8	61.9
0.1	10	1.06	30.5	-30.6	-0.6	61.1
0.1	100	1.06	30.5	-30.4	0.1	60.9
1	0	0.322	26.4	-52.7	-13.2	79.1
1	0.1	0.400	26.6	-51.9	-12.7	78.5
1	1	0.748	27.2	-44.7	-8.8	71.9
1	10	1.03	29.1	-33.4	-2.2	62.5
1	100	1.06	30.3	-30.6	-0.2	60.9
10	0	0.271	9.8	N/A	N/A	N/A
10	0.1	0.294	10.0	-176.4	-83.2	186.4
10	1	0.456	11.4	-107.8	-48.2	119.2
10	10	0.898	19.8	-51.9	-16.1	71.7
10	100	1.05	28.6	-33.2	-2.3	61.7
100	0	0.265	-16.2	N/A	N/A	N/A
100	0.1	0.272	-16.0	-245.5	-130.7	229.5
100	1	0.331	-15.0	-177.3	-96.2	162.2
100	10	0.645	-7.2	-104.9	-56.1	97.7
100	100	0.997	15.9	-50.2	-17.2	66.0

Table 4.2: Simulated peak height ratios, peak positions and peak separations for DC cyclic voltammetry of an EC reaction model with $k^0 = 10^{-1}$ cm s^{-1}. Other parameters used were $E_{start} = -0.3$ V, $E_{max} = 0.5$ V, $\nu = 0.1$ V s^{-1}, $E^0 = 0$ V, $\alpha = 0.5$, $c_\infty = 1$ mM, $S = 0.07$ cm^2, $D = 2 \times 10^{-5}$ cm^2 s^{-1}, $T = 296$ K, $R_u = 0$ Ω, $C_{dl} = 0$ μF cm^{-2}.

case, where the peak current ratio approaches a limiting value corresponding to the disappearance of the reduction peak, as well as the oxidation peak occurring at a more negative potential.

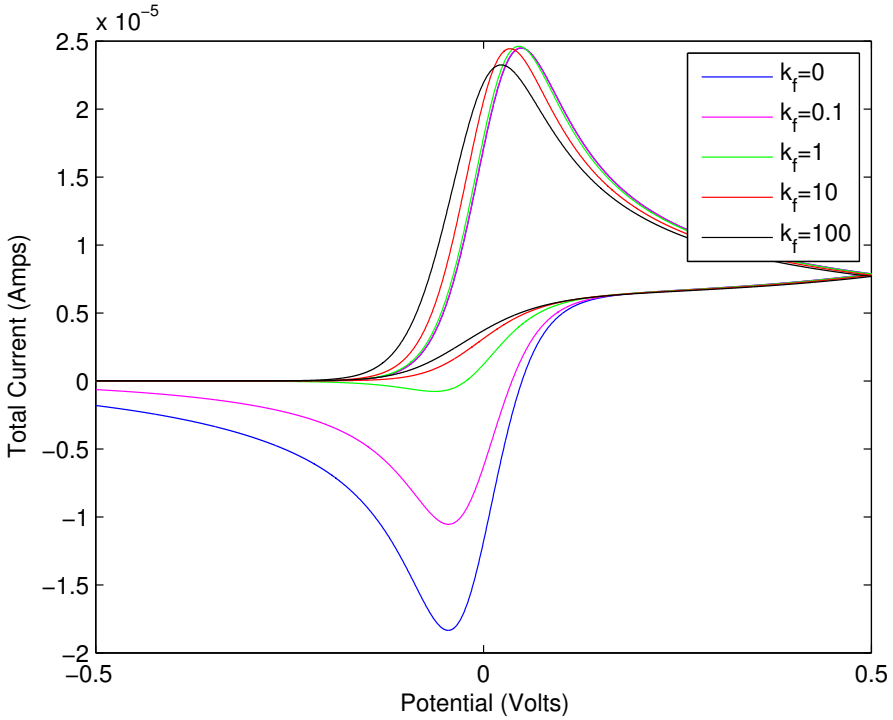

Figure 4.2: The effect of increasing k_f in simulations of DC cyclic voltammetry, with $k^0 = 10^{-2}$ cm s^{-1} and $k_b = 0$ s^{-1}. Other parameters as in the caption of Table 4.3.

Table 4.3 shows the measurements taken from DC cyclic voltammetry simulations using $k^0 = 10^{-2}$ cm s^{-1}, corresponding to a quasi-reversible electron transfer reaction. Again, the case of $k_b > k_f$ is relatively uninteresting, with measurements approaching those taken for the E reaction. For $k_b = 0$ s^{-1}, again increasing k_f rapidly causes the reduction peak to disappear, but in this case, further increases also result in a lessening in magnitude of the oxidation peak current, as shown in Figure 4.2. In the case of this EC$_{irrev}$ reaction, increases in k_f also shift the

oxidation peak to more negative potentials.

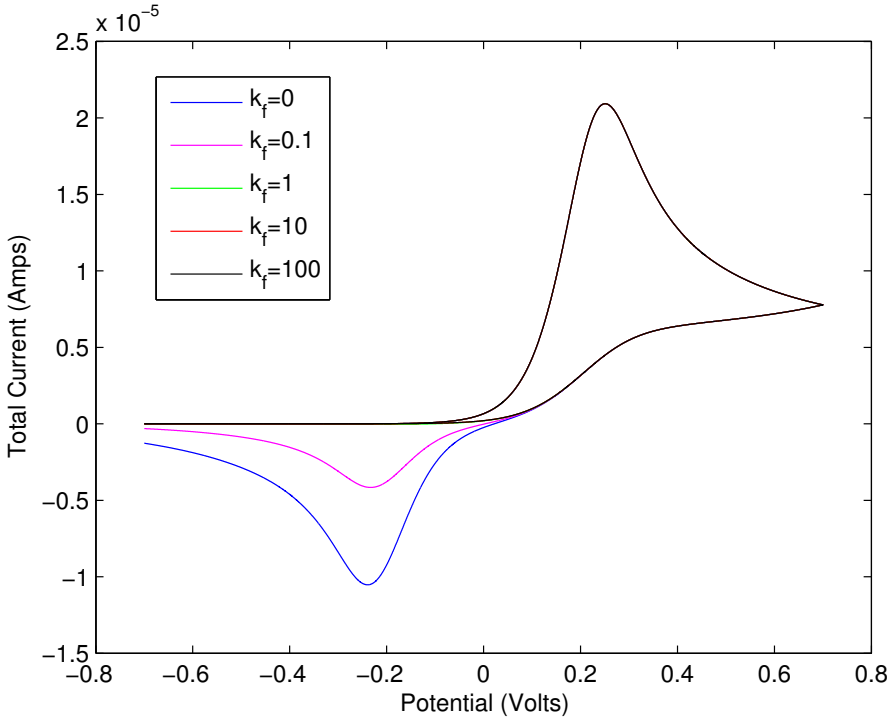

Figure 4.3: The effect of increasing k_f in simulations of DC cyclic voltammetry, with $k^0 = 10^{-4}$ cm s^{-1} and $k_b = 0$ s^{-1}. Other parameters as in the caption of Table 4.4.

Tables 4.4 and 4.5 show the resulting measurements from DC cylic voltammetric simulations at $k^0 = 10^{-4}$ cm s^{-1} and $k^0 = 10^{-6}$ cm s^{-1}, respectively. The immediately obvious pattern is that there is no variation at all in the oxidation peak position, and indeed the size and shape, as we see in Figure 4.3. Referring again to Tables 4.4 and 4.5, we see that changes in the chemical reaction rate parameters k_f and k_b do result in changes to the reduction peak size and position, with trends such as the reduction peak disappearing when $k_f \gg k_b$ again being apparent. As was mentioned previously, however, in an experimental setting, one is not guaranteed to have access to both an oxidation and a reduction peak. In

k_f (s^{-1})	k_b (s^{-1})	I_{pb}/I_{pf}	E_{Ipf} (mV)	E_{Ipb} (mV)	E_m (mV)	ΔE_p (mV)
0	0	1.07	48.7	-45.6	1.6	94.2
0.1	0	0.752	48.2	-45.4	1.4	93.5
0.1	0.1	0.838	48.2	-46.6	0.8	94.7
0.1	1	1.02	48.4	-47.3	0.5	95.7
0.1	10	1.07	48.4	-45.8	1.3	94.2
0.1	100	1.07	48.7	-45.6	1.6	94.2
1	0	0.350	45.5	-62.9	-8.7	108.4
1	0.1	0.429	45.5	-65.9	-10.2	111.3
1	1	0.776	46.0	-61.7	-7.9	107.7
1	10	1.05	47.7	-49.0	-0.7	96.7
1	100	1.07	48.4	-45.8	1.3	94.2
10	0	0.318	34.0	N/A	N/A	N/A
10	0.1	0.342	34.2	-192.3	-79.1	226.6
10	1	0.509	35.5	-132.0	-48.3	167.5
10	10	0.927	41.3	-71.0	-14.9	112.3
10	100	1.06	47.2	-48.8	-0.8	96.0
100	0	0.331	22.8	N/A	N/A	N/A
100	0.1	0.338	22.8	-262.4	-119.8	285.2
100	1	0.401	23.3	-211.6	-94.2	234.9
100	10	0.706	26.9	-137.4	-55.3	164.3
100	100	1.02	39.4	-70.0	-15.3	109.4

Table 4.3: Simulated peak height ratios, peak positions and peak separations for DC cyclic voltammetry of an EC reaction model with $k^0 = 10^{-2}$ cm s^{-1}. Other parameters used were $E_{start} = -0.5$ V, $E_{max} = 0.5$ V, $\nu = 0.1$ V s^{-1}, $E^0 = 0$ V, $\alpha = 0.5$, $c_\infty = 1$ mM, $S = 0.07$ cm^2, $D = 2 \times 10^{-5}$ cm^2 s^{-1}, $T = 296$ K, $R_u = 0$ Ω, $C_{dl} = 0$ μF cm^{-2}.

k_f (s^{-1})	k_b (s^{-1})	I_{pb}/I_{pf}	E_{Ipf} (mV)	E_{Ipb} (mV)	E_m (mV)	ΔE_p (mV)
0	0	0.875	251.0	-239.2	5.9	490.2
0.1	0	0.570	251.0	-233.0	9.0	484.0
0.1	0.1	0.675	251.0	-240.2	5.4	491.2
0.1	1	0.842	251.0	-241.9	4.5	492.9
0.1	10	0.873	251.0	-239.9	5.6	490.9
0.1	100	0.875	251.0	-239.2	5.9	490.2
1	0	0.373	251.0	N/A	N/A	N/A
1	0.1	0.436	251.0	-278.9	-13.9	529.8
1	1	0.692	251.0	-263.5	-6.3	514.5
1	10	0.861	251.0	-244.0	3.5	495.0
1	100	0.874	251.0	-239.9	5.6	490.9
10	0	0.372	251.0	N/A	N/A	N/A
10	0.1	0.390	251.0	-388.9	-69.0	639.9
10	1	0.512	251.0	-346.5	-47.8	597.5
10	10	0.785	251.0	-274.1	-11.6	525.1
10	100	0.868	251.0	-244.3	-3.4	495.3
100	0	0.372	251.0	N/A	N/A	N/A
100	0.1	0.377	251.0	-457.3	-103.1	708.3
100	1	0.422	251.0	-435.8	-92.4	686.6
100	10	0.630	251.0	-359.5	-54.3	610.5
100	100	0.831	251.0	-274.8	-11.9	525.7

Table 4.4: Simulated peak height ratios, peak positions and peak separations for DC cyclic voltammetry of an EC reaction model with $k^0 = 10^{-4}$ cm s^{-1}. Other parameters used were $E_{start} = -0.7$ V, $E_{max} = 0.7$ V, $\nu = 0.1$ V s^{-1}, $E^0 = 0$ V, $\alpha = 0.5$, $c_\infty = 1$ mM, $S = 0.07$ cm^2, $D = 2 \times 10^{-5}$ cm^2 s^{-1}, $T = 296$ K, $R_u = 0$ Ω, $C_{dl} = 0$ μF cm^{-2}.

k_f (s^{-1})	k_b (s^{-1})	I_{pb}/I_{pf}	E_{Ipf} (mV)	E_{Ipb} (mV)	E_m (mV)	ΔE_p (mV)
0	0	0.672	486.0	-474.5	5.8	960.6
0.1	0	0.428	486.0	-468.7	8.7	954.7
0.1	0.1	0.529	486.0	-477.5	4.3	963.5
0.1	1	0.652	486.0	-477.9	4.3	963.5
0.1	10	0.671	486.0	-475.0	5.5	961.1
0.1	100	0.672	486.0	-474.5	5.8	960.6
1	0	0.352	486.0	N/A	N/A	N/A
1	0.1	0.393	486.0	-516.1	-15.0	1002.1
1	1	0.557	486.0	-499.0	-6.5	985.0
1	10	0.664	486.0	-479.4	3.3	965.4
1	100	0.672	486.0	-475.0	5.5	961.1
10	0	0.352	486.0	N/A	N/A	N/A
10	0.1	0.364	486.0	-624.5	-69.2	1110.5
10	1	0.442	486.0	-582.0	-48.0	1068.0
10	10	0.616	486.0	-509.7	-11.9	995.7
10	100	0.669	486.0	-479.4	4.4	965.4
100	0	0.352	486.0	N/A	N/A	N/A
100	0.1	0.356	486.0	-692.3	-103.2	1178.4
100	1	0.385	486.0	-671.3	-92.7	1157.4
100	10	0.517	486.0	-594.7	-54.4	1080.7
100	100	0.645	486.0	-510.2	-12.1	996.2

Table 4.5: Simulated peak height ratios, peak positions and peak separations for DC cyclic voltammetry of an EC reaction model with $k^0 = 10^{-6}$ cm s^{-1}. Other parameters used were $E_{start} = -1.0$ V, $E_{max} = 1.0$ V, $\nu = 0.1$ V s^{-1}, $E^0 = 0$ V, $\alpha = 0.5$, $c_\infty = 1$ mM, $S = 0.07$ cm^2, $D = 2 \times 10^{-5}$ cm^2 s^{-1}, $T = 296$ K, $R_u = 0$ Ω, $C_{dl} = 0$ μF cm^{-2}.

the case of an extremely irreversible electron transfer step such as happens with $k^0 = 10^{-6}$ cm s^{-1}, with only one peak not only are k_f and k_b structurally unidentifiable using DC voltammetry, meaning that any combination of these parameters in a simulation model would fit the experimental data, but in addition the E and EC mechanisms are indistinguishable [87].

4.3.2 Parameter recovery

In the previous section, we have performed an extensive simulation exercise to identify some different parameter regimes for further investigation. From this point onwards, we will select a few examples, and test our ability to estimate the system parameters accurately using our time-domain parameter recovery algorithm when experiments are performed using either DC or AC cyclic voltammetry. In order to make the exercise not only non-trivial, but also to have it bear more resemblance to an actual experiment, we will generate simulated experimental data using our chosen parameters, and then perturb it by adding noise to mimic instrumentation measurement errors at a level of 5% of the peak current, as in Chapter 2, and according to Equation (2.36).

Our first example corresponds to a fully reversible electron-transfer reaction with $k^0 = 10^3$ cm s^{-1}, followed by a reversible chemical reaction with $k_f = k_b = 100$ s^{-1}. Comparing the first and final rows of Table 4.1, we see that in this case we have a peak current ratio and peak separation (using DC voltammetry) that are both close to those observed for an almost-reversible E reaction with no coupled chemical step, although with the peak positions shifted to more negative potentials, that could in the case of an E reaction be the result of a more negative value of E^0.

We have performed two exercises, using DC voltammetry and AC voltammetry

Model	E^0 (V)	k^0 (cm s^{-1})	α	k_f (s^{-1})	k_b (s^{-1})	L_{Glo}
DC EC QR5	0.067	0.29	0.41	0	44	3.03e-6
DC EC FR3	0.020	N/A	N/A	500	350	3.45e-6
DC E FR1	0.068	N/A	N/A	N/A	N/A	3.03e-6
AC E FR1	-0.011	N/A	N/A	N/A	N/A	8.78e-7
AC E QR3	-0.017	0.065	0.00	N/A	N/A	4.24e-7
AC EC QR5	0.000	2.0	0.61	98.0	99.0	4.18e-7
AC EC FR3	0.000	N/A	N/A	114.4	110.6	4.18e-7

Table 4.6: Parameters recovered from fitting models of different reaction mechanisms to data simulated using a model of an EC_{rev} reaction mechanism with $k^0 = 10^3$ cm s^{-1}, $k_f = 100$ s^{-1}, and $k_b = 100$ s^{-1} for both DC and AC voltammetry. Other parameters used were $E_{start} = -0.3$ V, $E_{max} = 0.5$ V, $\nu = 0.1$ V s^{-1}, $c_\infty = 1$ mM, $S = 0.07$ cm^2, $D = 2 \times 10^{-5}$ cm^2 s^{-1}, $T = 296$ K, $R_u = 0\ \Omega$, $C_{dl} = 0\ \mu F$ cm^{-2}, and for the AC voltammetry simulations, $\Delta E = 80$ mV and $f = 9$ Hz.

at 9 Hz, and attempted to fit up to four different models in each case: two EC reactions, designated as QR5 and FR3 (using the notation of Chapter 3, where QR5 represents a 5-parameter fit involving E^0, k^0, α, k_f and k_b in this case, and FR3 has $k^0 = 10^3$ cm s^{-1} and $\alpha = 0.5$ fixed), and two E reactions designated as QR3 and FR1. The results of these parameter fitting exercises are displayed in Table 4.6. As we can see, the DC technique is insufficient in this example, as we are unable to distinguish between the E and EC mechanisms, in addition to being unable to correctly identify the parameters. In contrast, with the AC technique we are able to find all parameters with some degree of accuracy when fitting the EC models, with E^0 being recovered precisely to the degree of accuracy reported, and the errors in k_f and k_b to be discussed in more detail in the following section.

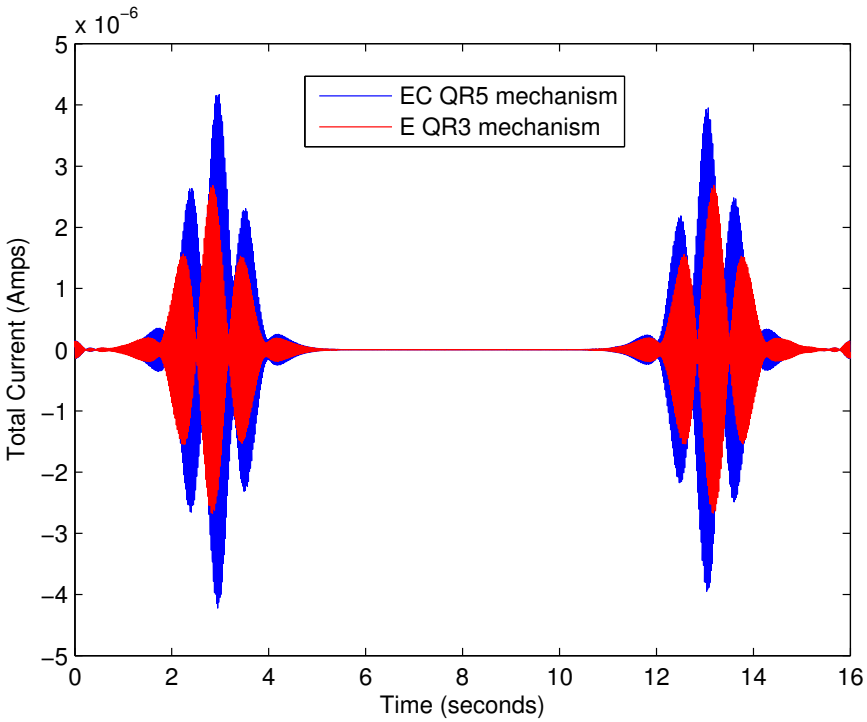

Figure 4.4: Comparing the 5th harmonic of simulations of an EC reaction with parameters taken from the "AC EC QR5" row of Table 4.6 (blue) and an E reaction with parameters taken from the "AC E QR3" row of the same table (red), showing a clear discrepancy.

As we would expect based on the work of Chapter 3, the values of k^0 and α are "incorrect" but k^0 falls within the regime of being "fully-reversible", and so the FR3 model is most likely more appropriate anyway.

When comparing the results of fitting the E and EC mechanisms, interestingly the objective functions are of similar magnitude when comparing the quasi-reversible models QR5 and QR3, with the anticipated result of the predicted E^0 value using FR1 being slightly more negative. The lack of ability to distintuish between the E and EC models using the automated time-domain parameter estimation method

is due to both models being able to compensate for the added noise in different ways and end up with a good fit. This inability to determine model parameters and, as a result, the most appropriate model to fit the data, is an example of practical unidentifiability in the presence of experimental noise. When simulations are performed based on each model with the parameter values reported by the parameter recovery algorithm, however, and particularly when higher harmonics such as the 5th harmonic pictured in Figure 4.4 are considered, it is clear that the differences between the predictions from the E and EC models are significant. The QR3 model of the E reaction falls short and would be rejected heuristically if such a check were performed. It would also be possible to include a similar check of the harmonics as well as just the time-domain in an automated parameter recovery algorithm to maintain operator-independence, in a way similar to the Nimrod software used in the previous chapters.

Model	E^0 (V)	k^0 (cm s^{-1})	α	k_f (s^{-1})	k_b (s^{-1})	L_{Glo}
DC	-0.004	0.0089	0.49	6.97	0.83	1.22e-8
AC	0.000	0.0099	0.50	9.91	0.99	1.04e-7

Table 4.7: Parameters recovered from using both DC and AC voltammetry and data simulated using a model of an EC_{rev} reaction mechanism with $k^0 = 10^{-2}$ cm s^{-1}, $k_f = 10$ s^{-1}, and $k_b = 1$ s^{-1}. Other parameters used were $E_{start} = -0.5$ V, $E_{max} = 0.5$ V, $\nu = 0.1$ V s^{-1}, $c_\infty = 1$ mM, $S = 0.07$ cm^2, $D = 2 \times 10^{-5}$ cm^2 s^{-1}, $T = 296$ K, $R_u = 0\ \Omega$, $C_{dl} = 0\ \mu F$ cm^{-2}, and for the AC voltammetry simulations, $\Delta E = 80$ mV and $f = 9$ Hz.

For our second example, we have chosen quasi-reversible electron transfer with $k^0 = 10^{-2}$ cm s^{-1}, followed by a reversible chemical reaction with $k_f/k_b = 10$. Again, referring to Table 4.3 (row 14), we see that the ratio of peak currents for a cyclic DC voltammetry experiment with these parameters is simulated as being in

the supposedly "identifiable" regime, being close to neither the "reversible" (row 1) nor "irreversible" (row 17) limits. Indeed, when we look at the results in Table 4.7 collected from this exercise, we see that both the AC and DC techniques recover parameters with reasonable accuracy, although AC voltammetry again appears to produce slightly preferable results. It is worth noting at this stage that we see that a "small" error in the estimation of E^0 using DC voltammetry may have had a follow-on effect on the estimates of the other parameters, almost by definition as k^0 is defined to be the value at E^0.

Model	E^0 (V)	k^0 (cm s^{-1})	α	k_f (s^{-1})	k_b (s^{-1})	L_{Glo}
DC EC$_{rev}$	0.003	0.0094	0.49	8.20	0.0024	1.20e-8
DC EC$_{irrev}$	-0.002	0.0092	0.49	9.61	N/A	1.20e-8
AC EC$_{rev}$	0.001	0.010	0.50	10.7	0.0011	9.89e-8
AC EC$_{irrev}$	-0.001	0.0099	0.50	9.41	N/A	9.89e-8

Table 4.8: Parameters recovered from using both DC and AC voltammetry and data simulated using a model of an EC$_{irrev}$ reaction mechanism with $k^0 = 10^{-2}$ cm s^{-1} and $k_f = 10$ s^{-1}. Other parameters used were $E_{start} = -0.5$ V, $E_{max} = 0.5$ V, $\nu = 0.1$ V s^{-1}, $E^0 = 0$ V, $\alpha = 0.5$, $c_\infty = 1$ mM, $S = 0.07$ cm^2, $D = 2 \times 10^{-5}$ cm^2 s^{-1}, $T = 296$ K, $R_u = 0\ \Omega$, $C_{dl} = 0\ \mu F$ cm^{-2}, and for the AC voltammetry simulations, $\Delta E = 80$ mV and $f = 9$ Hz.

Our final example in this section is of quasi-reversible electron transfer with $k^0 = 10^{-2}$ cm s^{-1}, followed by an irreversible chemical reaction with $k_f = 10$ s^{-1} (see Table 4.3, row 12). In this case, we have again run both DC and AC voltammetry simulations, and in each case we have fitted both an EC$_{rev}$ and an EC$_{irrev}$ model. The results of doing this are given in Table 4.8. The first observation to make is that in both the DC and AC cases it makes no real difference whether we attempt to fit a model with a reversible or irreversible chemical reaction step.

When the reversible model is used, the reported values of k_b are such that the ratio $K = k_f/k_b \approx 1000$, and the backwards reaction would be of negligible importance. Furthermore, similar levels of accuracy in recovering the parameters are obtained from both DC and AC voltammetry simulations, although it might be argued that the key parameter E^0 is again slightly more accurately estimated via AC voltammetry.

4.3.3 Bootstrapping

Having performed a preliminary investigation into the ability to estimate parameters from an EC reaction mechanism using our time-domain parameter recovery algorithm, we would like to gain further insight into the reliability of the reported parameter estimates by using the bootstrapping technique to generate confidence intervals, as in Chapter 3. In this case, as we are dealing only with simulated data rather than experimental data, for the sake of reproducibility we have generated both our time-series of current measurements and also an equal number of "noise" measurements, again drawn from a normal distribution with mean zero and standard deviation equal to 5% of the peak current. We have then generated our surrogate data sets by randomly re-sampling from this recorded noise distribution in an identical way to Chapter 3, according to Equation (3.6).

The results of five different bootstrapping experiments are presented in Table 4.9. These cover two cases: quasi-reversible electron transfer ($k^0 = 10^{-2}$ cm s^{-1}), followed by either a reversible chemical reaction with $k_f = k_b = 100$ s^{-1} (experiments 1, 4 and 5) or an irreversible chemical reaction with $k_f = 100$ s^{-1} (experiments 2 and 3). Techniques used, for purposes of comparison, were AC voltammetry with frequency 9 Hz (experiments 1 and 2), AC voltammetry with frequency 72 Hz

Experiment		E^0 (V)	k^0 (cm s^{-1})	α	k_f (s^{-1})	k_b (s^{-1})
1	input	0.000	0.010	0.50	100	100
	output	0.000 ± 0.002	0.010 ± 0.001	0.50 ± 0.01	101 ± 24	101 ± 14
2	input	0.000	0.010	0.50	100	0
	output	0.000 ± 0.004	0.010 ± 0.001	0.50 ± 0.01	102 ± 13	N/A
3	input	0.000	0.010	0.50	100	0
	output	0.000 ± 0.001	0.010 ± 0.000	0.50 ± 0.00	100 ± 4	N/A
4	input	0.000	0.010	0.50	100	100
	output	0.000 ± 0.001	0.010 ± 0.000	0.50 ± 0.00	100 ± 12	101 ± 12
5	input	0.000	0.010	0.50	100	100
	output	0.000 ± 0.002	0.010 ± 0.004	0.50 ± 0.01	99 ± 17	101 ± 13

Table 4.9: Parameters and their standard deviations recovered from 1000 iterations of the bootstrapping algorithm for five different experiments. The models used were: AC voltammetry with $\omega = 9$ Hz and $\Delta E = 80$ mV (experiments 1,2), AC voltammetry with $\omega = 72$ Hz and $\Delta E = 80$ mV (experiments 3,4), and DC voltammetry (experiment 5), with a scan rate of $\nu = 0.1$ V s^{-1} used in all cases. The parameters varied are given in the table in the "input" rows - in cases where $k_b = 0$ s^{-1}, an EC$_{irrev}$ model was fitted, otherwise the EC$_{rev}$ was used. Other parameters used were $E_{start} = -0.5$ V, $E_{max} = 0.5$ V, $c_\infty = 1$ mM, $S = 0.07$ cm^2, $D = 2 \times 10^{-5}$ cm^2 s^{-1}, $T = 296$ K, $R_u = 0\ \Omega$, $C_{dl} = 0\ \mu F$ cm^{-2}.

(experiments 3 and 4), and DC voltammetry (experiment 5). These combinations of parameters were both chosen to be nontrivial to recover, based on the measurements from Table 4.3 (row 17 and the final row), with the irreversible reaction ($k_b = 0$ s^{-1}) having a similar peak current ratio for different values of k_f and just a shift in the peak potential position which could result from a change in E^0, and the reversible reaction having similar peak current ratio and positions to those resulting from a reversible reaction with $k_f = k_b = 10$ s^{-1} (row 16), say. We have chosen to avoid the fully-reversible k^0 regimes due to overlap with the problem considered in Chapter 3, and the irreversible k^0 regime due to intractability of the problem when the back-sweep peak is assumed not to be present.

We can make several comparisons and comments. Across all three techniques, in the EC$_{rev}$ case, identification of the values of the chemical reaction rates k_f and k_b within even a 10% tolerance appears to be impossible. Again, this is a result of the ability of the other model parameters to compensate for changes in k_f and k_b in these simulations which include simulated experimental noise, which only allows us to report a confidence interval for each parameter, with the limits of the interval depending on the quantity of noise included. When comparing between the methods, however, we notice that the accuracy of the reported parameter estimates is superior when comparing 72 Hz AC voltammetry to 9 Hz. While the DC technique also appears to have produced a good estimate of k_f and k_b, it must be noted with caution that estimates of E^0 and k^0 obtained using DC voltammetry are worse than those recovered by the high frequency AC experiment. In addition, while the reported k_f and k_b values may appear to have similar ranges from both the AC and DC voltammetry methods, we can consider correlation between these two parameters and, in effect, the reported value of $K = k_f/k_b$. Figure 4.5 shows a scatter plot of pairs of reported k_f and k_b values from the DC (blue) and AC (red) bootstrapping experiments. We can see clearly that the (k_f,k_b) pairs from

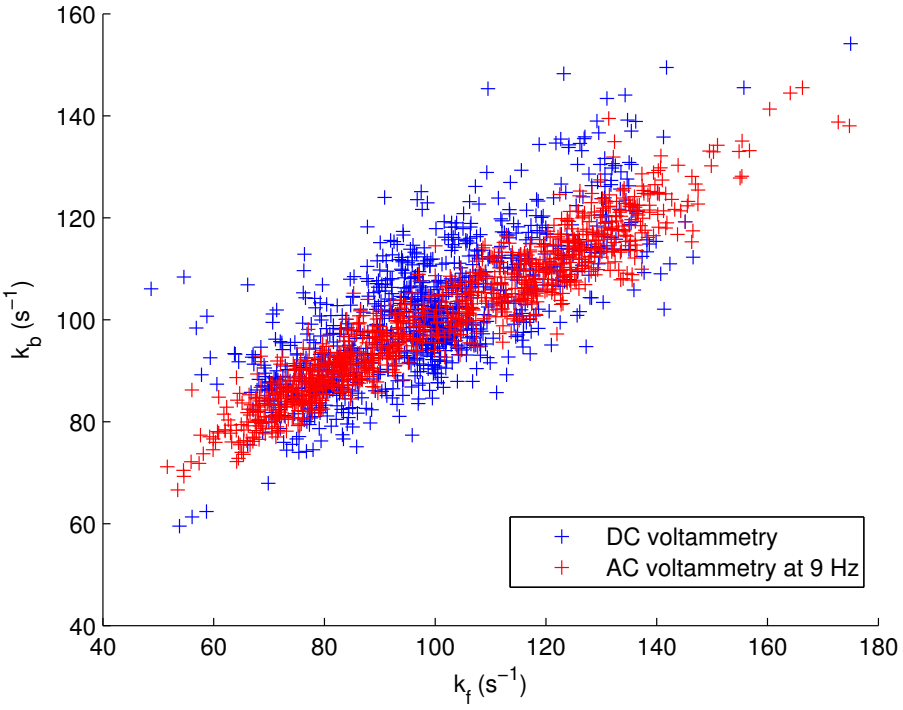

Figure 4.5: Scatter plot of the values of k_f and k_b recovered from the 1000 iterations of the bootstrapping experiments 1 (DC voltammetry, blue) and 5 (AC voltammetry, red) from Table 4.9. We observe a slightly weaker correlation between the values of k_f and k_b from the simulations based on DC voltammetry.

the AC experiment, shown in red, lie closer to a line of best fit which could be drawn through them than the corresponding pairs from the DC experiment, shown in blue. Upon calculation of the mean value of k_f/k_b, we also get an equlibrium constant $K = 1$, which is exactly the value of K that was used in the simulation. The (k_f,k_b) pairs from the DC experiment are not only more scattered, but also correspond to a slightly less accurate equilibrium constant value of $K = 0.97$.

In the case of the EC_{irrev} reaction, the high frequency AC method clearly outperforms the lower frequency one, as all parameter estimates have a narrower

interval, and indeed at 72 Hz, all parameters are recovered with less than a 5% error.

Frequency (Hz)	E^0 (V)	k^0 (cm s^{-1})	α	k_f (s^{-1})
Input	0.000	0.010	0.50	100
9	0.000 ± 0.004	0.010 ± 0.001	0.50 ± 0.01	102 ± 12.5
18	0.000 ± 0.002	0.010 ± 0.001	0.50 ± 0.01	101 ± 6.4
27	0.000 ± 0.002	0.010 ± 0.000	0.50 ± 0.01	102 ± 4.7
36	0.000 ± 0.002	0.010 ± 0.000	0.50 ± 0.01	101 ± 4.2
45	0.000 ± 0.001	0.010 ± 0.000	0.50 ± 0.00	100 ± 4.2
54	0.000 ± 0.001	0.010 ± 0.000	0.50 ± 0.00	100 ± 4.2
63	0.000 ± 0.001	0.010 ± 0.000	0.50 ± 0.00	100 ± 4.2
72	0.000 ± 0.001	0.010 ± 0.000	0.50 ± 0.00	100 ± 4.2
216	0.000 ± 0.001	0.010 ± 0.000	0.50 ± 0.00	100 ± 3.7

Table 4.10: The results of bootstrapping on a series of AC voltammetric simulation experiments observing the effect of using different frequencies on the accuracy of the results (based on confidence interval width). Parameters varied were E^0, k^0, α and k_f, with their values used to produce the "clean" simulated data (prior to addition of noise) listed in the "Input" row. Other parameters used were $E_{start} = -0.5$ V, $E_{max} = 0.5$ V, $\alpha = 0.5$, $c_\infty = 1$ mM, $S = 0.07$ cm^2, $D = 2\times10^{-5}$ cm^2 s^{-1}, $T = 296$ K, $R_u = 0\ \Omega$, $C_{dl} = 0\ \mu F$ cm^{-2}.

Motivated by our observations of the results presented in Table 4.9, for our final experiment, we investigate the effect of using different frequencies of AC perturbation on the accuracy of recovered parameters, using as our example the quasi-reversible electron transfer followed by an irreversible chemical reaction with $k_f = 100$ s^{-1} as in experiments 2 and 3 of Table 4.9. Our results are shown in Table 4.10. We notice significant gains in the accuracy of all parameters as the frequency is

increased from 9 Hz to 36 Hz, and small improvements with further increases in frequency beyond that.

4.3.4 A brief comment on the frequency domain

Our work in this chapter has been focused on using the time-domain optimisation algorithm to estimate model parameters. When employing AC voltammetric techniques, we have seen in Chapters 2 and 3 that another powerful method is to use the frequency domain and the harmonics of the AC perturbation.

As a short acknowledgement of the viability of this approach, we have included Figures 4.6 and 4.7, showing the effects of different regimes of k_f on the 2nd and 5th harmonics, respectively, for an EC_{irrev} reaction with quasi-reversible electron transfer. We see that in this range of k_f there is an immediately apparent effect across the time interval recorded. The various peaks in the harmonics become smaller compared with the case of no coupled chemical reaction (represented in blue as $k_f = 0\ s^{-1}$), and this decline in magnitude appears to occur at different rates depending on the harmonic in question. Observations of this nature suggest that a heuristic approach to parameter estimation, performed by an experienced operator, could still be useful, particularly as a guide or reference against which to test the results of automated parameter recovery algorithms. Alternatively, as was mentioned earlier, an automated parameter optimisation over the harmonics could also be performed to maintain the operator-independence of the parameter estimation process.

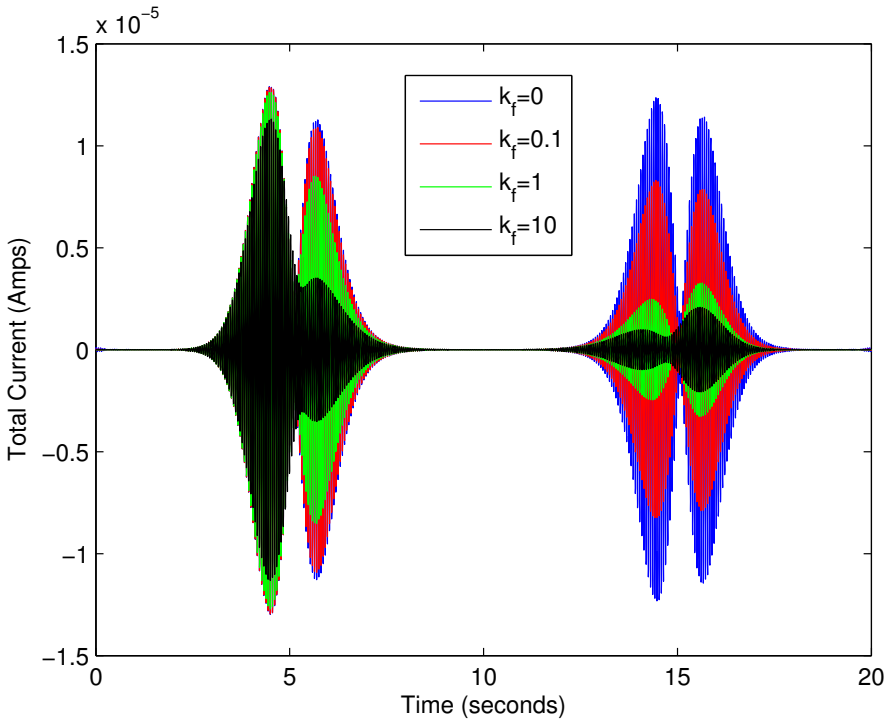

Figure 4.6: The effect of variations in k_f on the 2nd harmonic of an AC voltammetric simulation at 9 Hz of an EC_{irrev} reaction mechanism. Other parameters used were $E_{start} = -0.5$ V, $E_{max} = 0.5$ V, $E^0 = 0$ V, $k^0 = 10^{-2}$ cm s^{-1}, $\alpha = 0.5$, $\nu = 0.1$ V s^{-1}, $\Delta E = 80$ mV, $c_\infty = 1$ mM, $S = 0.07$ cm^2, $D = 2 \times 10^{-5}$ cm^2 s^{-1}, $T = 296$ K, $R_u = 0\ \Omega$, $C_{dl} = 0\ \mu F$ cm^{-2}.

4.4 Conclusions

In the course of this chapter, we have performed a theoretical exercise to test our ability to estimate parameters from EC reaction mechanisms in a variety of parameter regimes using the techniques of DC and AC cyclic voltammetry. Results of forwards simulations are consistent with those published by previous authors, and our initial attempts to set up and run parameter recovery exercises suggest that AC voltammetry is often capable of providing good estimates of the reaction paramet-

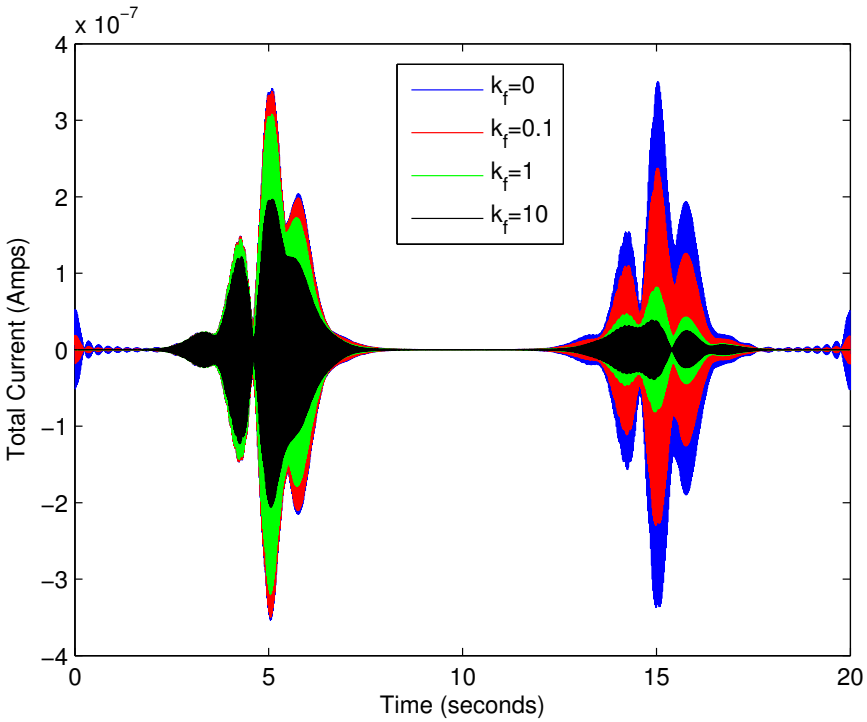

Figure 4.7: The effect of variations in k_f on the 5th harmonic of an AC voltammetric simulation at 9 Hz of an EC_{irrev} reaction mechanism. Other parameters used were $E_{start} = -0.5$ V, $E_{max} = 0.5$ V, $E^0 = 0$ V, $k^0 = 10^{-2}$ cm s^{-1}, $\alpha = 0.5$, $\nu = 0.1$ V s^{-1}, $\Delta E = 80$ mV, $c_\infty = 1$ mM, $S = 0.07$ cm^2, $D = 2 \times 10^{-5}$ cm^2 s^{-1}, $T = 296$ K, $R_u = 0\ \Omega$, $C_{dl} = 0\ \mu F$ cm^{-2}.

ers. Comparisons with DC techniques, further enhanced by use of bootstrapping to explore parameter identifiability, suggest that not only does AC voltammetry offer a more powerful toolkit for investigation of these more complicated reaction mechanisms but also that, in the case of the EC reaction mechanism, use of high AC frequencies can often further improve our ability to estimate the parameters in question. In the future work section in Chapter 6, we will briefly discuss how these ideas might be extended to other mechanisms involving coupled reactions.

Chapter 5

Dispersion

In the work presented up to this point, we have considered only electron transfer reactions taking place in a solution where the species involved in electron transfer reactions are able to move around freely by diffusion. A substantial branch of electrochemistry is concerned with reactions taking place between species which are adsorbed onto an electrode surface. In this chapter, we will consider two mathematical models for such a reaction, include the effects of the acknowledged phenomenon of dispersion, and demonstrate that our results are consistent with those found in the relevant literature.

5.1 Background

In the case of solution-phase voltammetry, as we have seen in previous chapters, agreement between theory and experiment is often obtained to a level where one is not easily able to distinguish between the two. For surface-confined studies, however, such a high degree of agreement between theory and experiment has

arguably never been achieved, even under what are considered to be the most ideal conditions. In terms of these theory-experiment comparisons, the closest matches between simulations based on current theoretical models and results from voltammetric experiments are obtained when the surface coverage of adsorbed molecules is of at most monolayer thickness [6, 7, 50, 62].

When this condition is imposed, there is an accepted analytical solution for the simulation of cyclic DC voltammetry of a reversible process in the presence of no uncompensated resistance or capacitive current, derived from the Nernst relationship [11, 16]. In particular, this analytical solution predicts a value for the width of the Faradaic peak at half its maximum height, designated as $W_{1/2}$, given by

$$W_{1/2} = 3.53\frac{RT}{nF}, \tag{5.1}$$

which for a single-electron transfer ($n = 1$) at 293 K works out to be 89 mV. In practice, these assumptions are not unreasonable: levels of R_u are typically very low in surface-confined experiments, background current due to double-layer capacitance can often be subtracted from the total current empirically and, even for a quasi-reversible process, if a sufficiently low scan rate is used a reaction can often appear to be almost reversible. Reported values of $W_{1/2}$ from experiments, however, are always greater than would be expected from this prediction, with a typical example being the low scan rate study by Armstrong et al. [50] of the quasi-reversible azurin process, where $W_{1/2}$ is reported as being 18 mV greater than the value predicted by the Nernst equation.

Several possible explanations have been proposed for this consistently reported discrepancy between theoretical predictions and experimental results, and in this chapter we will consider the oft-cited phenomenon of dispersion [16]. Dispersion in this context can be described as the absence of a single value of E^0 (thermodynamic dispersion) and/or k^0 (kinetic dispersion).

In the solution-phase voltammetry considered up to this point, this idea of a distribution of values of E^0 and k^0 is not encountered to such a degree. By definition, there can only be a single value of E^0 applying to all dissolved species. At an ideal homogeneous electrode such as mercury, there would only be a single value of k^0 as well, although more recent studies have shown that on some specific electrodes, different values of k^0 may occur due to, for example, areas of differing electrode composition in the study by Unwin et al. [81], or locally varying electrode geometry in studies at carbon electrodes [8, 30, 59, 67, 68]. Even in these cases, however, the presence of diffusion of species between these sites means that it is normally only possible to report an average value of k^0 across an experiment [31].

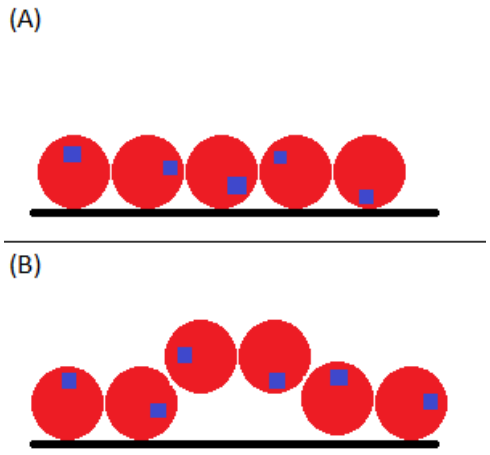

Figure 5.1: A cartoon showing different binding orientations of molecules (red discs) resulting in a varying distance between the electrode surface (black line) and the electroactive sites (blue squares) of each molecule (A), and an example of a possible defect in the monolayer attachment of molecules (B) which can also lead to variations in this distance.

In studies concerned only with surface-confined species, where there is no dissolution and a Langmuir isotherm is assumed, with no interaction between adsorbed

species, this blending together of different modes does not necessarily occur. Figure 5.1 shows two cartoon panels as an attempt to motivate the inclusion of dispersion into the theoretical consideration of applying voltammetry techniques to such surface-confined species. In the top panel, an ideal monolayer is shown adsorbed onto an electrode surface. Any variation in the orientation at which molecules have adsorbed relative to the electrode surface can result in variations in the distance from the redox-active site in each molecule and the electrode surface that will be traversed by electrons. These variations in distance can be expected, in turn, to result in variations in the values of k^0. The lower panel shows an example of an imperfection in the monolayer film of molecules, which also gives rise to different values of k^0 by similar reasoning. Unlike in, for example, the Boron-doped diamond study mentioned previously [81], where there were two distinct modes present, in this case we would expect a continuous variation of k^0 values to be possible, giving rise to a statistical distribution in the values of this parameter over all the molecules attached to the surface. Finally, in contrast to the solution-phase studies, each surface-confined molecule may have a slightly different environment for its redox site, which can also result in variations in E^0.

This intuitive justification for the inclusion of dispersion in theoretical models is appealing, and has been proposed by other authors, particularly relating to the study of catalytic processes involving enzymes adsorbed onto electrode surfaces. When voltammetric experiments are conducted on such enzymes using a rotating disk electrode configuration, potential-dependent limiting currents are almost always observed, rather than the ideal potential-independent limiting current. Leger et al. [63] suggested dispersion as a cause, citing an argument similar to the one stated here, and proposed an empirical model to incorporate dispersion based on a distribution of distances between the electrode surface and electroactive site of the catalyst. In this distribution, all values of the tunnelling distance between

the electrode surface and the electroactive site, d, occurred with equal probability between a minimum and maximum value, and zero probability outside of that range. This model has been elaborated upon [84] and applied to other enzymes in similar studies [33], and recently used as part of a substantial experimental study on the effects of dispersion by Fourmond et al. [37].

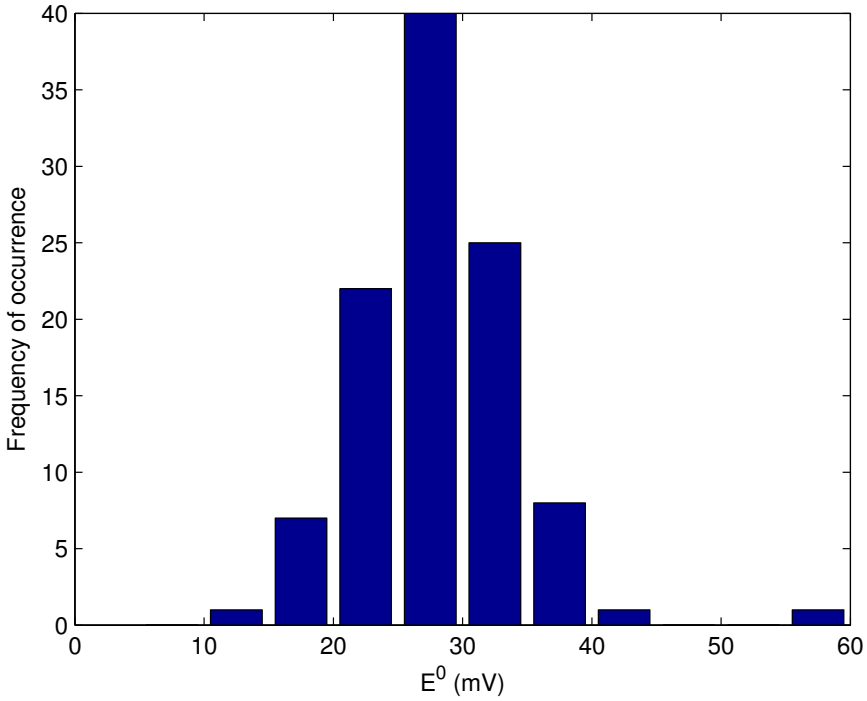

Figure 5.2: A reproduction of panel (a) in Figure 4 of [88], showing a histogram of the distribution of E^0 values reported.

A significant hurdle to be overcome before quantitative theory-experiment comparisions can be conducted has been the lack of any information on realistic distributions of E^0 and k^0 values that might be encountered experimentally. However, recent studies by Davis et al. [79,80,88] involving small numbers of modified azurin molecules with fluorescent properties has resulted in distributions of the values of these parameters being reported. Histograms adapted from [88] are shown in Fig-

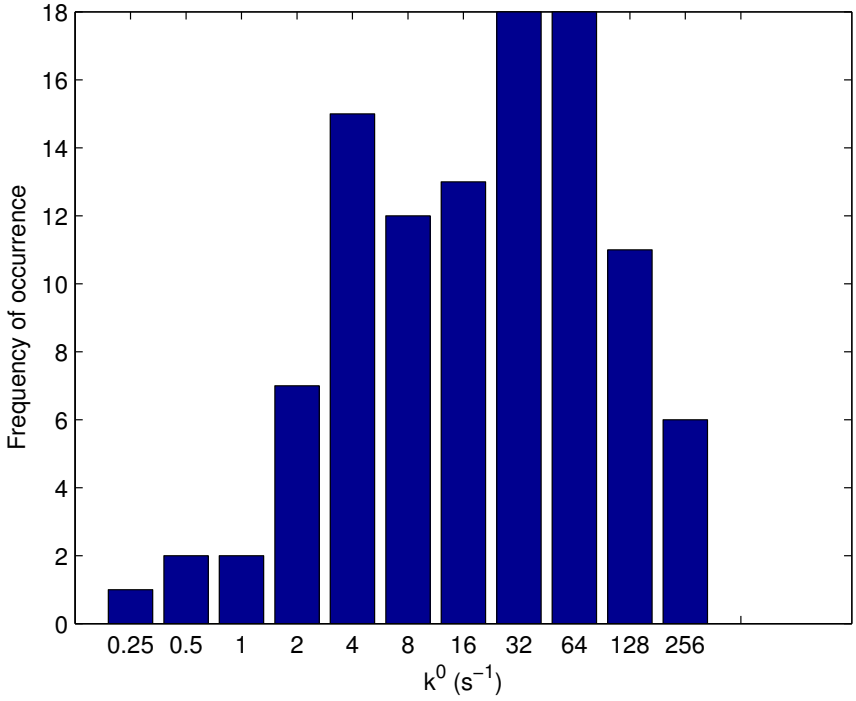

Figure 5.3: A reproduction of panel (c) in Figure 4 of [88], showing a histogram of the distribution of k^0 values reported.

ures 5.2 and 5.3, showing the distributions of E^0 and k^0, respectively. Using these distributions as a basis, we will proceed firstly to incorporate the effects of kinetic and thermodynamic dispersion into our simulations, and then to examine whether these phenomena are capable of accounting for the reported differences between experimental results and previously-accepted theoretical predictions, particularly the broadening of the Faradaic peak exemplified by increased values of $W_{1/2}$.

In the context of our overall theme of the inverse problem and parameter estimation in AC voltammetry, accounting for the discrepancies reported consistently throughout the literature between experimental results and theoretical predictions is essential. We have seen in our previous work with solution-soluble electroactive

species that even minor flaws in the underlying mathematical model can make parameter identification almost impossible to achieve with any confidence, so if we are able to fill this gap by updating the theory to match with experiments, we will have drawn significantly closer to being able to perform meaningful theory-experiment comparisions for voltammetric experiments on surface-confined species, and hence once again to the overall goal of producing an operator-independent method of parameter recovery in AC voltammetry.

5.2 Methods

We will present two different mathematical models for the underlying chemistry, namely: a continuum ODE-based model; and a stochastic formulation where each molecule is treated as an individual and the number of molecules in each possible state is tracked as it evolves with time according to probabilities that reactions take place. As in Chapters 2 and 3, we will consider the reaction

$$A \underset{k_{red}}{\overset{k_{ox}}{\rightleftharpoons}} B + e^{-}, \tag{5.2}$$

though in this case both species A and B will be attached to the electrode surface.

5.2.1 ODE model

Due to the fact that the species involved in the reaction are no longer mobile, we are required to set up a different framework to model the ongoing reactions than that of the diffusion equation, similarly to [11,46,51]. We introduce the idea of the proportion of surface coverage by each species up to at most a monolayer, and let θ be the proportion of the total surface coverage accounted for by species A. As a

result, the proportion of surface coverage by species B is given by $1-\theta$. Making the assumption of a Langmuir isotherm, where adsorbed species do not interact with each other, we can then write down the governing equation for the evolution of θ with time as

$$\frac{\mathrm{d}\theta}{\mathrm{d}t} = k_{red}(1-\theta) - k_{ox}\theta. \tag{5.3}$$

As previously, the rates of reaction k_{red} and k_{ox} are given in terms of the standard rate constant, k^0, and charge-transfer coefficient, α, via Butler-Volmer kinetics, as

$$\begin{aligned} k_{ox} &= k^0 \exp\left[\frac{(1-\alpha)F}{RT}(E_{app}(t) - I_{tot}R_u - E^0)\right], \\ k_{red} &= k^0 \exp\left[\frac{-\alpha F}{RT}(E_{app}(t) - I_{tot}R_u - E^0)\right]. \end{aligned} \tag{5.4}$$

The analogous form of the Faradaic current, I_f, without dependence on mass transport, is

$$I_f = -FS\Gamma\frac{\mathrm{d}\theta}{\mathrm{d}t}, \tag{5.5}$$

where Γ represents the combined surface coverage by A and B per unit area of the electrode.

The capacitive current, I_c, is once again given by

$$I_c = C_{dl}\frac{\mathrm{d}E}{\mathrm{d}t}, \tag{5.6}$$

where again $E(t)$ is the potential, and the total current, I_{tot}, is given by

$$I_{tot} = I_f + I_c. \tag{5.7}$$

The model is completed by the initial conditions

$$\begin{aligned} \theta(0) &= 1, \\ I_{tot}(0) &= 0. \end{aligned} \tag{5.8}$$

In order to obtain a numerical approximation, this system is then discretised according to a backwards Euler finite difference scheme and, noting that k_{red}^{m+1} and k_{ox}^{m+1} are functions of I_{tot}^{m+1} as in Equation (5.4), Equation (5.3) becomes

$$\theta^{m+1} = \frac{\theta^m + k_{red}^{m+1}(I_{tot}^{m+1})\Delta t}{1 + \left(k_{red}^{m+1}(I_{tot}^{m+1}) + k_{ox}^{m+1}(I_{tot}^{m+1})\right)\Delta t}, \tag{5.9}$$

after some re-arrangement, where, as in Chapter 2, m denotes the time index and Δt the time step, so θ^m represents $\theta(t = m\Delta t)$ and so on, and k_{red}^m and k_{ox}^m are evaluated according to Equation (5.4) at discrete time index m.

This is now an equation of the form

$$\theta^{m+1} = f(I_{tot}^{m+1}), \tag{5.10}$$

and substitution of this into a discretised form of Equation (5.7), expanded according to Equations (5.5) and (5.6) to be

$$I_{tot}^{m+1} = -FS\Gamma\frac{\theta^{m+1} - \theta^m}{\Delta t} + C_{dl}\left(\nu + \Delta E\omega\cos(\omega m\Delta t) - \frac{I_{tot}^{m+1} - I_{tot}^m}{\Delta t}R_u\right), \tag{5.11}$$

yields an equation also of the form

$$g(I_{tot}^{m+1}) = 0. \tag{5.12}$$

This equation can be solved using Brent's method [22] to complete the numerical solution.

We note that we have included both R_u and C_{dl} in this statement of the model to make it general, but for all simulations in this chapter, they will be neglected.

5.2.2 Stochastic model

The second model we will consider is an individual-based stochastic model, often referred to as the stochastic formulation of chemical kinetics where, for a system

that is assumed to be well-mixed, we track only the discrete population numbers of each molecular species and their evolution with time. Each possible reaction is then assigned a probability of occurring as a function of time, and the system is allowed to evolve according to these probabilities. As an individual-based model, this stochastic formulation is applicable to a wider range of systems than the ODE-type methods which rely on the assumption that the number of molecules can be modelled as varying continuously and deterministically, which may not be the case in systems involving, for example, a small number of molecules.

As an attempt to formulate and solve such a model, one might start from a chemical master equation, which tracks the time evolution of a quantity $\mathcal{P}(n_A, n_B, t)$, representing the probability at time t of being in the particular state where there are n_A molecules of A and n_B molecules of B. In our case, with the reaction proceeding according to Equation (5.2), the master equation would be

$$\begin{aligned}\frac{\mathrm{d}\mathcal{P}(n_A, n_B, t)}{\mathrm{d}t} = \; & \mathcal{P}(n_A + 1, n_B - 1, t)(n_A + 1)k_{ox} + \mathcal{P}(n_A - 1, n_B + 1, t)(n_B + 1)k_{red} \\ & - \mathcal{P}(n_A, n_B, t)n_A k_{ox} - \mathcal{P}(n_A, n_B, t)n_B k_{red}. \end{aligned} \tag{5.13}$$

The master equation accounts for all possible reactions which may happen, and as such is typically computationally intractable. Although in the case when only a single reaction is considered, the master equation can be manipulated to show that the average number of molecules of species A, say, evolves according to Equation (5.3), this is not of much interest for the problem of dispersion. When multiple reactions proceeding at different rates are included, this method becomes less useful.

Instead, a common approach for calculating the evolution of such a set of reactions is to use a stochastic simulation algorithm, such as the one originally proposed by Gillespie [44, 45], to generate a statistically exact sample path or trajectory along which the system may evolve. Trajectories are chosen based on the probabilities of

each reaction occuring at any time, an inherently random process which results in variation between iterations. It is then possible to calculate statistical summaries of features of interest such as the concentration of species at particular times, by averaging over many sample trajectories.

In Gillespie's approach, N chemical species X_i undergo M distinct chemical reactions R_i ($i = 1, ..., M$), each of which has a reaction parameter or "propensity function", $a_i(X(t))$, defined by the fundamental hypothesis of chemical kinetics to be such that $a_i(X(t))\Delta t$ is the probability, to first order in Δt, that reaction R_i takes place in the time interval $[t, t+\Delta t)$. Gillespie proceeds to show that the time until the next reaction, Δ, is exponentially distributed. The original algorithm which he proposed involved at each iteration drawing two random numbers: one from an exponential distribution to determine the time until the next reaction, and one from a uniform distribution to determine which of the M reactions occurred at that time.

Numerous improvements to Gillespie's so-called direct method, from the point of view of computational efficiency, have been offered. One such widely used method was proposed by Gibson and Bruck, named the "next reaction method", and crucially involves the generation of only a single random number per iteration loop within the algorithm [42]. The algorithm we employ is based on this next reaction method, and was designated by its creator, Anderson, as the "modified next reaction method" [5]. Importantly, and unlike both the direct method and the next reaction method, the modified next reaction method allows for propensity functions $a(X(t), t)$ which vary explicitly with time.

In this algorithm, the stochasticity of each of the M reactions is incorporated in

unit-rate Poisson processes, Y_i, with internal times, T_i, given by

$$T_i(t) = \int_0^t a_i(X(s))\mathrm{d}s, \tag{5.14}$$

and the time until the next firing of Y_i after time T_i is denoted by P_i.

The algorithm proceeds as follows:

1. Initialise. Set the initial number of molecues of A and B in state $X(0)$, set $t = 0$, and for every i set $P_i = 0$ and $T_i = 0$.
2. Calculate the propensity function, a_i, for each reaction.
3. Generate M independent uniform(0,1) numbers, r_i.
4. For each i, set $P_i = \log(1/r_i)$.
5. For each i, set $\Delta t_i = (P_i - T_i)/a_i$.
6. Set $\Delta = \min_i\{\Delta t_i\}$ and let μ be the reaction for which this minimum time is realised.
7. Set $t = t + \Delta$ and update the number of each species according to reaction R_μ.
8. For each i, set $T_i = T_i + a_i\Delta$.
9. For reaction μ, let r be a uniform(0,1) random number, and set $P_\mu = P_\mu + \log(1/r)$.
10. Recalculate the propensity functions, a_i.
11. Go to step 5 or end if a suitable amount of time has elapsed or a desired target state has been reached (in our case, for example, this could be the

system completing a full transition from only species A being present to only species B being present).

In order to use this method for our system of interest, we must know how to represent the propensity functions, a_i, in terms of the rates of reaction, k_i. According to Gillespie's original paper, for a reaction involving a single molecule of a single species, the relationship between the propensity functions and the rates of reaction is simply

$$a_i(X(t), t) = X_i(t)k_i(t). \tag{5.15}$$

For the case we are currently considering, described by Equation (5.2), we have $M = 2$ and $N = 2$, and our propensity functions are

$$\begin{aligned} a_1(X(t), t) &= X_1(t)k_{ox}(t) \\ &= X_1(t)k^0 \exp\left[\frac{(1-\alpha)F}{RT}(E_{app}(t) - I_{tot}R_u - E^0)\right], \\ a_2(X(t), t) &= X_2(t)k_{red}(t) \\ &= X_2(t)k^0 \exp\left[\frac{-\alpha F}{RT}(E_{app}(t) - I_{tot}R_u - E^0)\right], \end{aligned} \tag{5.16}$$

where X_1 represents A and X_2 represents B. We begin with the initial state

$$\begin{aligned} X_1(0) &= K, \\ X_2(0) &= 0, \end{aligned} \tag{5.17}$$

then as in the algorithm, at each step we find the time increments until each reaction would next take place, Δt_i, by solving

$$\int_t^{t+\Delta t_i} a_i(X(t), s)\mathrm{d}s = P_i - T_i, \tag{5.18}$$

for each Δt_i, and then set

$$\Delta = \min_i \Delta t_i. \tag{5.19}$$

Solving Equation (5.18) in general is nontrivial, and requires numerical approximations. It is worth mentioning that in the case where $R_u = 0$ and $E_{app}(t)$ is a DC signal given simply by

$$E_{app}(t) = E_{start} + vt, \tag{5.20}$$

we can solve this integral equation exactly to give

$$\begin{aligned}\Delta t_1 &= \frac{RT}{Fv(1-\alpha)} \log\left[1 + \frac{Fv(1-\alpha)}{RT}\frac{P_1 - T_1}{a_1(X(t),t)}\right], \\ \Delta t_2 &= -\frac{RT}{Fv\alpha} \log\left[1 - \frac{Fv\alpha}{RT}\frac{P_2 - T_2}{a_2(X(t),t)}\right].\end{aligned} \tag{5.21}$$

In the case where $R_u = 0$ and $E_{app}(t)$ is an AC signal given by

$$E_{app}(t) = E_{start} + vt + \Delta E \sin(\omega t), \tag{5.22}$$

we use a degree-2 Newton-Cotes formula to evaluate the integral, obtaining

$$P_1 - T_1 = X_1(t)k^0 \frac{\Delta t_1}{6}\left[f(t + \Delta t_1) + 4f\left(t + \frac{\Delta t_1}{2}\right) + f(t)\right], \tag{5.23}$$

where

$$f(s) = \exp\left(\frac{F(1-\alpha)}{RT}(E_{start} + vs + \Delta E \sin(\omega s) - E^0)\right), \tag{5.24}$$

and similarly for the second reaction. Equation (5.23) can then be trivially rearranged into a form

$$g(\Delta t_1) = 0, \tag{5.25}$$

which can be solved using, for example, Brent's method.

5.2.3 Including dispersion

Including the effects of dispersion into each of these models is in principle straightforward. The key decision for both is how to go about choosing and then sampling from the distributions of the values of E^0 and k^0.

For the general shape of the distributions of E^0 and k^0, we appeal to [88]. The authors report, in panels (a) and (c) of Figure 4, adapted here as Figures 5.2 and 5.3, that they have measured distributions for both parameters, which we claim as a first approximation to be normal for E^0 and normal on a log-scale, i.e. log-normal, for k^0.

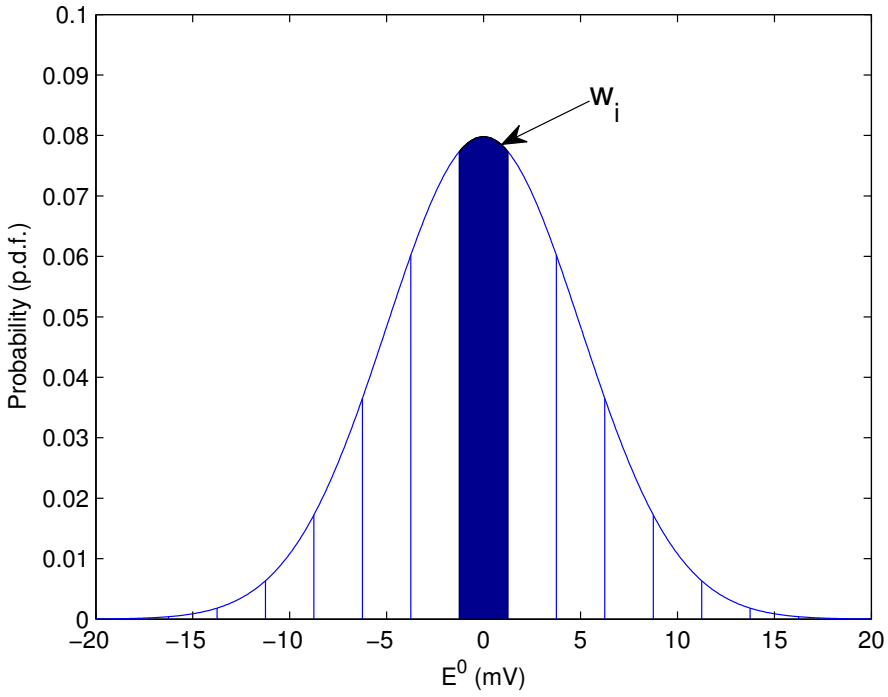

Figure 5.4: A figure showing the origin of the weights, w_i, as being equal to the area under the probability density function between the values at the edge of each bin.

There are two immediately obvious methods to sample from these distributions available to us. Firstly, we could divide the ranges of each of E^0 and k^0 values into q bins, and apply to each a weighting, w, derived from the cumulative distribution functions of their respective approximated distributions as pictured in Figure 5.4, or indeed make direct use of the weightings reported in the above paper. Alternat-

ively, we could randomly sample from the approximated distributions a number of times equal to the number of (k^0, E^0) pairs we wish to consider, when weightings would be applied via the sampling process itself. The first method lends itself more to reproducibility of results, so for the purposes of comparison between the two models, we will use that approach.

For the ODE model, we treat each combination of E^0 and k^0 as a separate system, solve the ODE for each such reaction, and then take a weighted average of the resulting concentration or current profiles according to our sampling technique described above. This results in an overall current for the system including dispersion, I_{disp}, given by

$$I_{disp} = \sum_{i=1}^{q^2} w_i I_i, \tag{5.26}$$

where I_i are the discrete current time series for each of the q^2 combinations of E^0 and k^0. The weightings w_i obtained by calculating the area under the probability density functions corresponding to the particular E^0 and k^0 intervals, w_{E_j} and w_{k_j} $(j = 1, ..., q)$, as shown in Figure 5.4, and then

$$w_i = w_{E\_j} w_{k\_j}, \tag{5.27}$$

with the property that

$$\sum_{i=1}^{q^2} w_i = 1. \tag{5.28}$$

For the stochastic simulation method, we similarly treat each combination of E^0 and k^0 as a separate reaction pair with its own populations and propensities. This increases the value of M in the above representation to be twice the number of (E^0, k^0) pairs, and the weighting is imposed by a suitable choice of the starting populations.

5.2.4 Comparison between models

As was mentioned previously, the model based on the stochastic formulation for chemical kinetics is arguably the superior model. It is valid in not only every case where the deterministic ODE model works, but also situations where the ODE model is not valid, such as when dealing with a small number of molecules, where the fact that the populations of species are integers and hence not actually continous can become important. At the same time, the computational cost of the stochastic model is significantly higher, with the generation of even a single sample trajectory taking many times longer (of the order of minutes or even hours) than solution of the ODE model (of the order of a second). We are ultimately hoping to be able to use one of these algorithms as part of a parameter estimation toolkit, which would most likely require multiple calls to the function implementing our numerical solution to simulate a voltammetric experiment. Computation time is therefore a significant factor, and ideally we would like to be able to justify using the much faster ODE method. As such, we would like to investigate the validity of the ODE model at surface concentration levels typical in experimental settings by comparing the simulated concentration profiles with those produced by solving the stochastic model. If we are able to discover that the ODE model predicts an indistinguishable concentration profile to that predicted by the stochastic model, we may safely use the ODE model for our future investigations.

Before presenting any comparisons between results from simulations of the ODE and stochastic models, we first need to motivate our choice of population size for simulations using the stochastic model. In Figure 5.5 we show sample trajectories generated using populations of 100 (blue), 500 (red), 1000 (green) and 5000 (black) molecules and using a DC potential input with no dispersion included. As we might expect, when a very small population is used, the resulting concentration

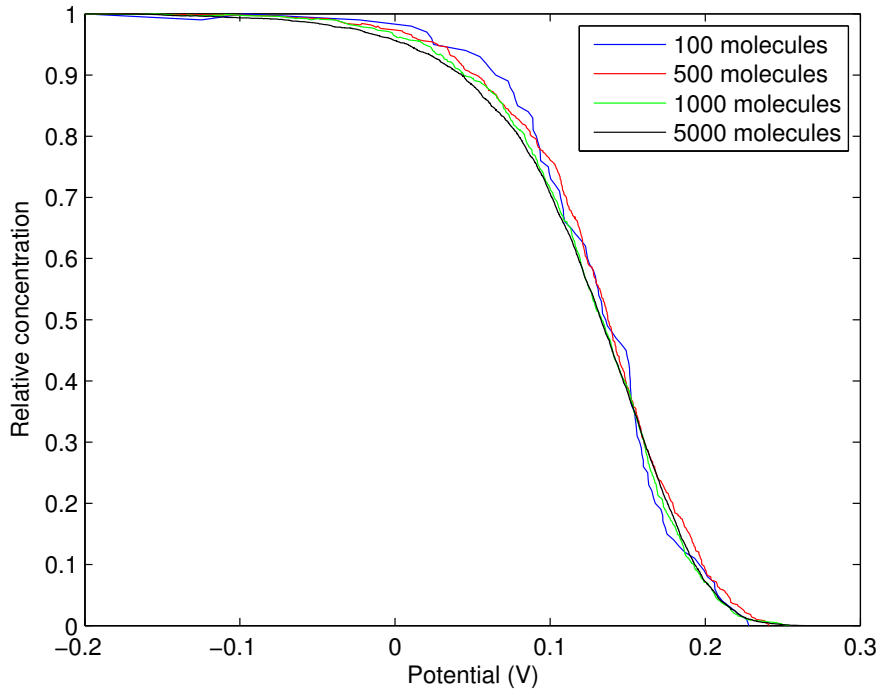

Figure 5.5: A comparison of the concentration profiles resulting from simulating sample trajectories from the stochastic model using different populations of molecules. Parameters used: $T = 293$ K, $v = 1$ V s^{-1}, $S = 1$ cm^2, $E^0 = 0$ V, $k^0 = 1$ s^{-1}, $\alpha = 0.5$, $E_{start} = -0.2$ V.

profile is not smooth, and is subject to substantial variation from the mean concentration on each calculated trajectory. As the population size is increased, we notice that individual trajectories deviate less from the mean concentration, and with a population of 5000 molecules, the concentration profile is indistinguishable from the mean concentration given by solving the equations of the ODE model (not included in the figure). Following a similar procedure, in each of the following examples we have chosen a population where sample trajectories exhibit little variation from each other, and can be said to have almost converged.

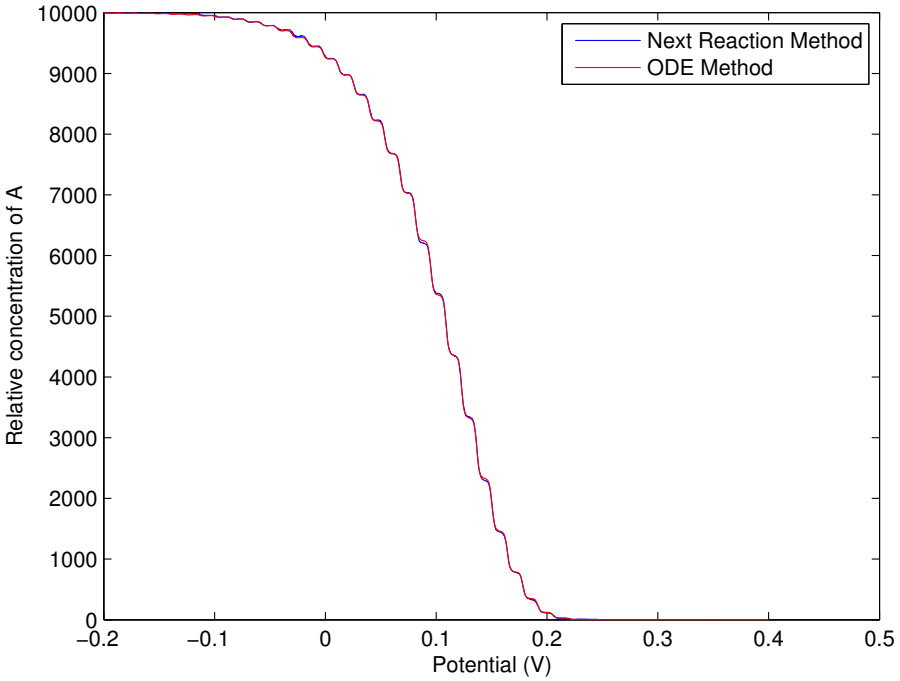

Figure 5.6: A comparison of the concentration profiles resulting from solving both the ODE (red) and stochastic (blue) models for a forwards sweep of AC voltammetry with no E^0 or k^0 dispersion included. The number of molecules used for the stochastic simulation was 10000. Parameters used: $T = 293$ K, $v = 1$ V s^{-1}, $S = 1$ cm^2, $\alpha = 0.5$, $E_{start} = -0.2$ V, $dE = 0.08$ V, $\omega = 2\pi \times 72$ Hz, $k^0 = 1$ s^{-1}, $E^0 = 0$ V, $\Gamma = 1 \times 10^{-11}$ mol cm^{-2}.

Figure 5.6 shows results from a typical example of AC voltammetry without including any dispersion in the values of either E^0 or k^0, using 10000 molecules in the simulation. As we can see, in this case there is a near perfect match between the surface concentration profile for A as predicted by both the ODE and stochastic methods.

k^0 (s^{-1})		k^0 and E^0	E^0 (V)	
exponent range	"mid"-point	weight	range	midpoint
(-∞,-6.5)	-7	0.0006	(-∞,-16.25)	-17.5
(-6.5,-5.5)	-6	0.0024	(-16.25,-13.75)	-15
(-5.5,-4.5)	-5	0.0092	(-13.75,-11.25)	-12.5
(-4.5,-3.5)	-4	0.0278	(-11.25,-8.75)	-10
(-3.5,-2.5)	-3	0.0656	(-8,75,-6.25)	-7.5
(-2.5,-1.5)	-2	0.1210	(-6.25,-3.75)	-5
(-1.5,-0.5)	-1	0.1747	(-3.75,-1.25)	-2.5
(-0.5,0.5)	0	0.1974	(-1.25,1.25)	0
(0.5,1.5)	1	0.1747	(1.25,3.75)	2.5
(1.5,2.5)	2	0.1210	(3.75,6.25)	5
(2.5,3.5)	3	0.0656	(6.25,8.75)	7.5
(3.5,4.5)	4	0.0278	(8.75,11.25)	10
(4.5,5.5)	5	0.0092	(11.25,13.75)	12.5
(5.5,6.5)	6	0.0024	(13.75,16.25)	15
(6.5,∞)	7	0.0006	(16.25,∞)	17.5

Table 5.1: k^0 and E^0 dispersion weights and values for use in simulations. The "mid"-points for k^0 correspond to the exponents used, so for example a midpoint of 3 corresponds to an actual value of $k^0 = 2^3$ s^{-1} (note the logarithmic scale).

For a comparison involving dispersion, we will first quantify the amount of both E^0 and k^0 dispersion to be included in our simulations, in terms of their distribution parameters. Table 5.1 shows dispersion weights for both k^0 and E^0. We have divided both regions into 15 bins, and we weight around a simulation run at the "mid"-point of each region, where in the case of k^0 the bins are of uneven widths, as both the end- and mid-points are given in terms of a logarithmic scale. The weights given are consistent with E^0 being normally distributed with mean 0 and standard deviation 5 mV, and k^0 being log-normally distributed with the underlying normal distribution having mean 0 and standard deviation 2 s^{-1}.

Figure 5.7 shows an example using a DC input potential and including dispersion according to the method and weightings described above, again comparing the concentration profile of A predicted by simulation of the ODE model with that predicted by simulation of the stochastic model using a population of 10000 molecules. Once more we see that the two models predict surface concentration profiles for A which to the eye are almost identical.

For our final check, Figure 5.8 shows a comparison between the results from simulations using the ODE and stochastic model using an AC input potential and dispersion. In this case, we used 80000 molecules for the stochastic algorithm to ensure convergence. It is not surprising that more molecules would be required than for a DC potential, as the time-step between reactions is decreased with a larger number of molecules, and the more rapidly varying AC potential in combination with the higher rate constants present when kinetic dispersion is included requires a relatively smaller timestep. Again we see that the match between simulations from the two models is extremely good.

It is worth noting that as the complexity of the modelled system increases, the run-time of the stochastic method becomes significantly longer than the ODE

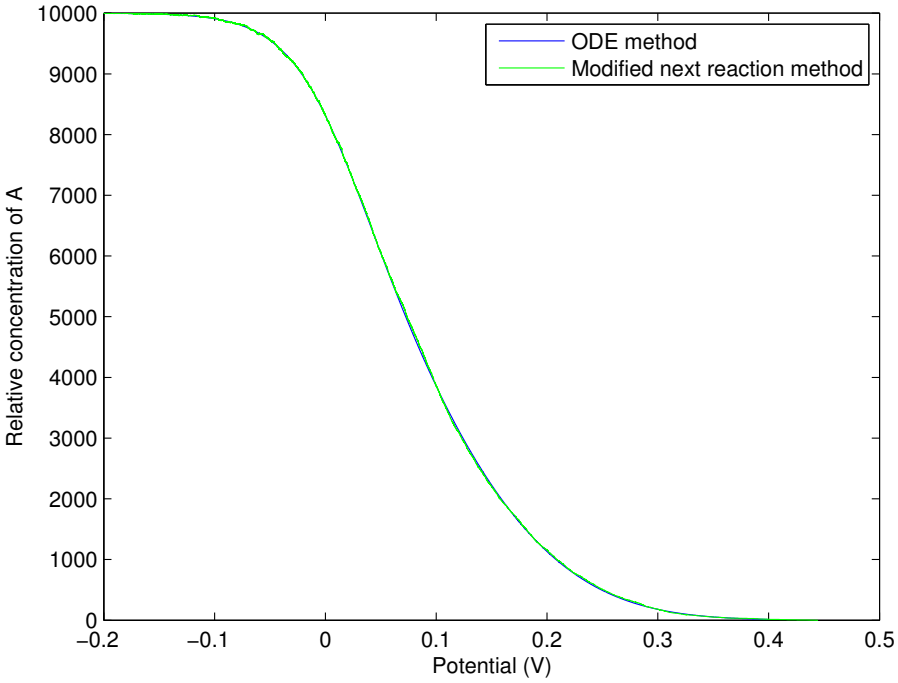

Figure 5.7: A comparison of the concentration profiles resulting from solving both the ODE (blue) and stochastic (green) models for a forwards sweep of DC voltammetry, with E^0 and k^0 dispersion included in quantities described in the text and Table 5.1. The number of molecules used for the stochastic simulation was 10000. Parameters used: $T = 293$ K, $v = 0.1$ V s^{-1}, $S = 1$ cm^2, $\alpha = 0.5$, $E_{start} = -0.2$ V, $\Gamma = 1 \times 10^{-11}$ mol cm^{-2}.

method. Producing a single trajectory for an AC potential using our code and the parameters listed may take as long as 10 minutes, compared with under one second for the ODE code to simulate a full system including dispersion effects. When k^0, or ω, is increased in AC simulations, both more oxidation and reduction reactions take place per fixed section of the underlying DC linear ramp due to the increased impact of the AC perturbation. In these cases, calculation of sample trajectories takes even longer, sometimes on a timescale of an hour, as many more reactions

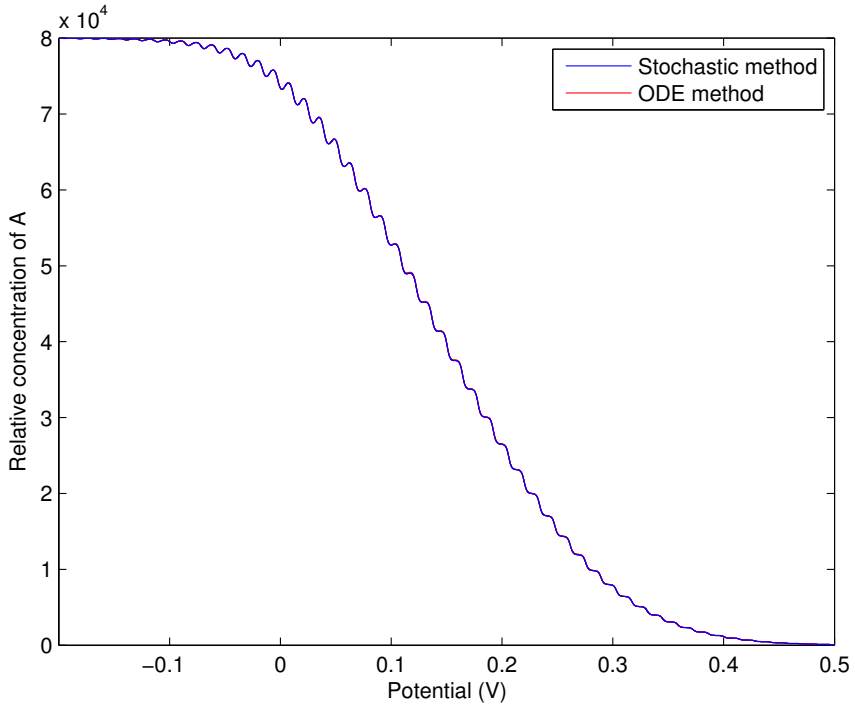

Figure 5.8: A comparison of the concentration profiles resulting from solving both the ODE (red) and stochastic (blue) models for a forwards sweep of AC voltammetry, with E^0 and k^0 dispersion included in quantities described in the text and Table 5.1. The number of molecules used for the stochastic simulation was 80000. Parameters used: $T = 293$ K, $v = 1$ V s^{-1}, $S = 1$ cm^2, $\alpha = 0.5$, $E_{start} = -0.2$ V, $dE = 0.08$ V, $\omega = 2\pi \times$ Hz, $\Gamma = 1 \times 10^{-11}$ mol cm^{-2}.

occur before the end condition for the algorithm is met. Some gains could be made to the computation time by making use of parallel processing resources. However not only are these not guaranteed to be available to a user, but it is also unlikely that the code would be sped up enough to compete with the ODE method.

As our two models produce near-identical output from the simplest cases all the way to the most difficult that we will consider, we may safely conclude that we

can use the computationally efficient ODE method for further calculations.

5.3 Results

Having justified our choice of simulation method, we proceed to investigate the effects of incorporating dispersion into our models, as opposed to ignoring it. We will begin by looking separately at the effects of E^0 and k^0 dispersion, respectively, and then at combining the two.

5.3.1 DC voltammetry

Initially, we will just consider DC voltammetry, and particularly the effect of both E^0 and k^0 dispersion on the half-height width, $W_{1/2}$, as this has been mentioned as one of the most obvious differences between predictions using a model that does not incorporate dispersion and results obtained experimentally for surface-confined species.

Figure 5.9 shows the results obtained by including E^0 dispersion in different amounts, but fixing $k^0 = 0.1$ s^{-1}. The full results are summarised in Table 5.2, comparing the amount of dispersion applied to the half-height width, $W_{1/2}$. The scaling was performed by using the E^0 values and weightings given in Table 5.1 and then multiplying the E^0 values by the scaling factor, l, to spread them out further, i.e.

$$E^0 = 0 + 2.5jl, \quad j = -7, -6, ..., 7. \tag{5.29}$$

In particular, we can see that including only E^0 dispersion in amounts consistent with those reported by Salverda et al. [88] and shown earlier in Figure 5.2 has

Scale, l	Spread (mV)	Half-height width (mV)
0	N/A	123
1	35	124
2	70	126
3	105	129
4	140	133
5	175	138
6	210	144
7	245	151
8	280	159
9	315	167
10	350	176

Table 5.2: The results of applying different amounts of E^0 dispersion as in Equation (5.29) with k^0 fixed at 0.1 s^{-1}, showing the effect on the half-height width $W_{1/2}$. For clarity, the column labelled "Spread" shows the separation between the minimum and maximum E^0 sample values in each case.

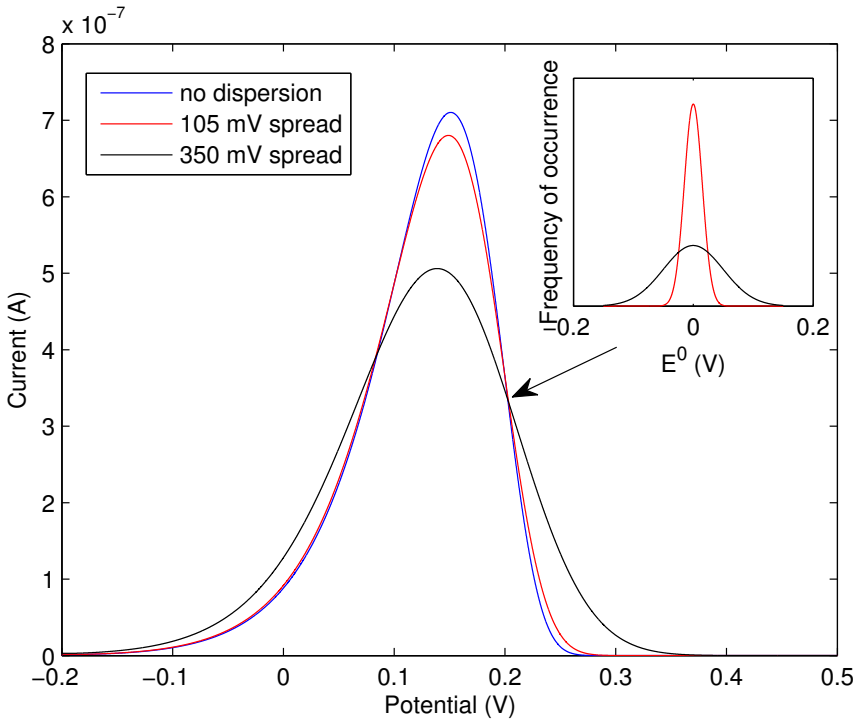

Figure 5.9: A comparison of the effects of including different amounts of E^0 dispersion, scaled as described in the text. The curves correspond to no dispersion ($l = 0$), i.e. $E^0 = 0$ V (blue), 105 mV separation ($l = 3$) between minimum and maximum E^0 values (red), and 350 mV separation ($l = 10$) between minimum and maximum E^0 values (black). Inset are the probability density functions corresponding to the distributions used for the two cases including dispersion. Other parameters used: $T = 293$ K, $v = 0.1$ V s^{-1}, $S = 1$ cm^2, $\alpha = 0.5$, $k^0 = 0.1$ s^{-1}, $E_{start} = -0.2$ V, $\Gamma = 1 \times 10^{-11}$ mol cm^{-2}.

almost no noticable impact on observable and measurable characteristics such as $W_{1/2}$ when compared with simply fixing E^0 at the mean value. In order to obtain anecdotally reported effects of a 20 mV gain in $W_{1/2}$ by including only E^0 dispersion, we would have to use roughly six times this experimentally measured spread in E^0 values.

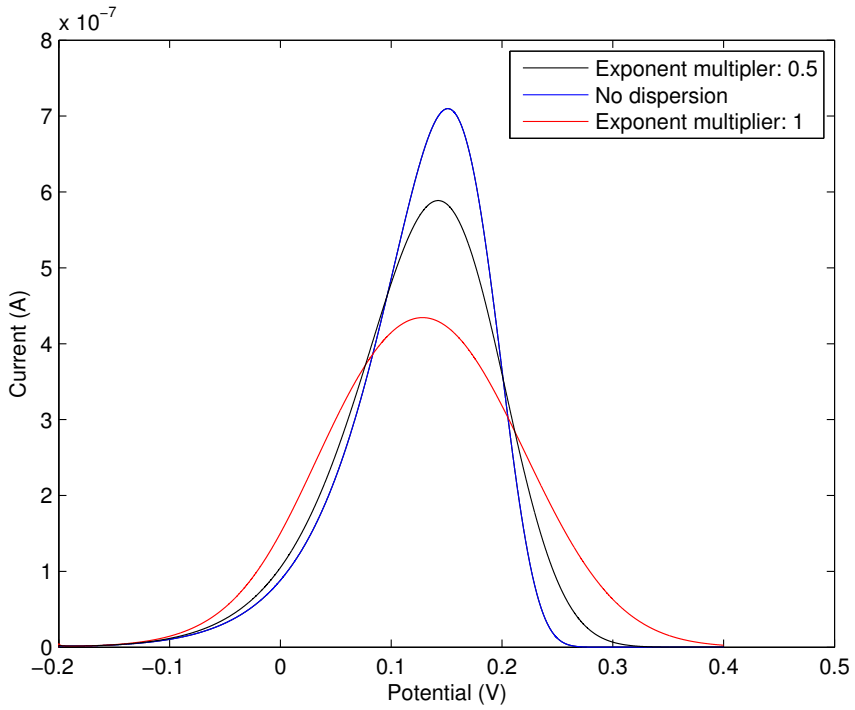

Figure 5.10: A comparison of the effects of including different amounts of k^0 dispersion, scaled as described in the text and Equation (5.30), and weighted according to Table 5.1. The curves correspond to no dispersion, i.e. $k^0 = 0.1$ s^{-1} (blue), exponent multipler $m = 0.5$ (black), and exponent multiplier $m = 1$ (red). Other parameters used: $T = 293$ K, $v = 0.1$ V s^{-1}, $S = 1$ cm^2, $\alpha = 0.5$, $E^0 = 0$ V, $E_{start} = -0.2$ V, $\Gamma = 1 \times 10^{-11}$ mol cm^{-2}.

A similar analysis for k^0 dispersion with fixed E^0 is displayed in Figure 5.10 and Table 5.3. E^0 was fixed at 0 V, and k^0 was scaled using the exponents from Table 5.1 multiplied by the "exponent multipler", m, from Table 5.3, an exponential base of 2, and an overall multiplier of 0.1, i.e.

$$k^0 = 0.1 \times 2^{mj}, \quad j = -7, -6, ..., 7. \tag{5.30}$$

This overall multiplier was added for the simulation work, as we notice that the

highest k^0 values encountered otherwise $(2^6, 2^7)$ are in such a range that they are almost indistinguishable from one another, similarly to the work from Chapter 3. We can see that using these slightly lower values of k^0 than were measured experimentally in [88] results in $W_{1/2}$ values significantly larger than we would hope for.

Exponent multiplier, m	Half-height width (mV)
0	123
0.1	124
0.2	128
0.3	134
0.4	141
0.5	150
0.6	161
0.7	172
0.8	185
0.9	198
1	211

Table 5.3: The results of applying different amounts of k^0 dispersion, included according to equation (5.30), with E^0 fixed at 0 mV, showing the effect on $W_{1/2}$.

This result, however, is perhaps not entirely unexpected. We have seen in Chapter 3 that when k^0 is close to or indeed at the reversible limit, further increases in its value by orders of magnitude are insignificant in terms of effect on the peak current and features such as the half-height width. We note by observation that at this scan rate, as can be seen in Figure 5.11, this limit appears to be around $k^0 = 10\ \mathrm{s}^{-1}$, and as such the source measurements for the distribution of k^0 values extends

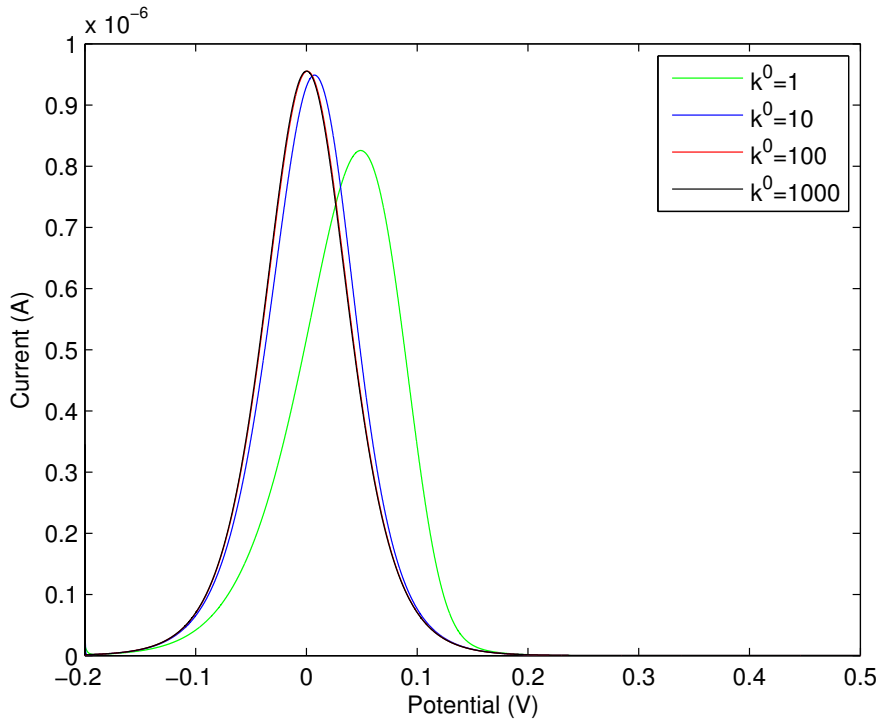

Figure 5.11: The effect of increasing k^0 for DC voltammetry at a scan rate of $v = 0.1$ V s^{-1}. We see that the reversible limit lies somewhere between $k^0 = 10$ s^{-1} and $k^0 = 100$ s^{-1}. Other parameters used: $T = 293$ K, $S = 1$ cm^2, $\alpha = 0.5$, $E^0 = 0$ V, $E_{start} = -0.2$ V, $\Gamma = 1 \times 10^{-11}$ mol cm^{-2}.

significantly beyond this. If our sample k^0 values for the dispersion distribution within a simulation are at the reversible limit, the effect is essentially the same as narrowing the upper end of the distribution and increasing the weighting closer to the centre, which we would expect to result in a smaller measurement of $W_{1/2}$.

Indeed if we repeat the simulation with weights adapted from the k^0 distribution reported in [88], and E^0 still fixed, we recover a half-height width value of $W_{1/2} = 99$ mV, contrasting with $W_{1/2} = 90$ mV with no dispersion included, or with the value $W_{1/2} = 89$ mV predicted for a fully-reversible process by the Nernst

relationship under these conditions. This suggests that k^0 dispersion encountered experimentally is typically less pronounced than the distribution reported in [88], if a gain of only 20 mV over the expected $W_{1/2}$ value is noticed even in lower regimes of k^0.

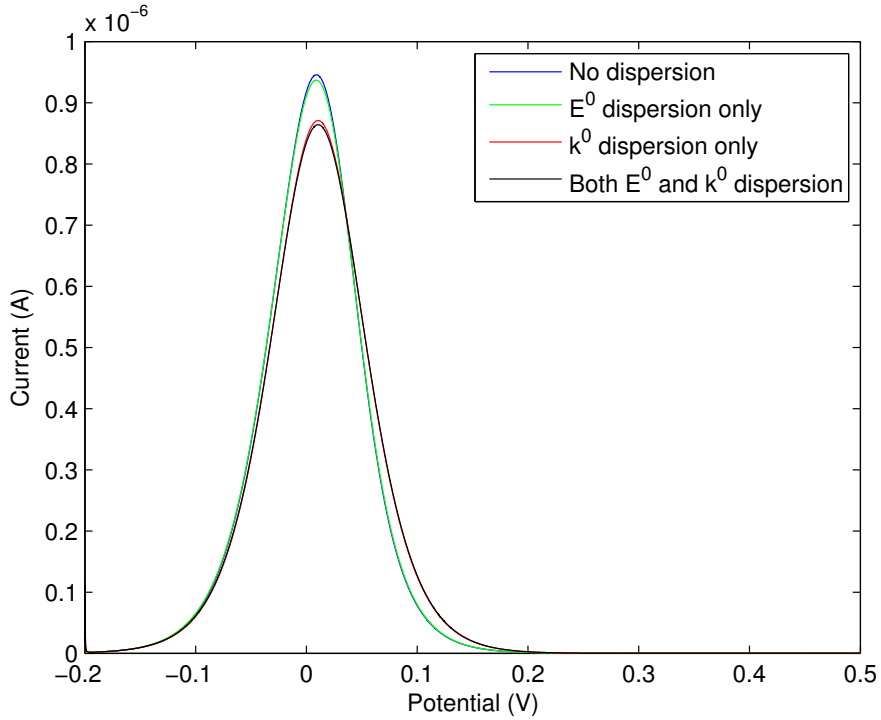

Figure 5.12: A comparision between the effects of including the different combinations of E^0 and/or k^0 dispersion on a DC voltammogram. We see that the blue and green curves, representing simulations without k^0 dispersion, lie almost on top of one another, as do the red and black curves, representing simulations including k^0 dispersion. These two cases, however, are clearly separated from each other, which shows the significantly greater impact of k^0 dispersion on the resulting current, compared with the impact of E^0 dispersion. Other parameters used: $T = 293$ K, $v = 0.1$ V s^{-1}, $S = 1$ cm^2, $\alpha = 0.5$, $E_{start} = -0.2$ V, $\Gamma = 1 \times 10^{-11}$ mol cm^{-2}. Where fixed, values of $E^0 = 0$ V and $k^0 = 1$ s^{-1} were used.

E^0 dispersion	k^0 dispersion	Half-height width (mV)
No	No	90
Yes	No	91
No	Yes	99
Yes	Yes	100

Table 5.4: The values of $W_{1/2}$ obtained from applying different combinations of E^0 and k^0 dispersion, weighted according to the distributions adapted from [88] and displayed in Figures 5.2 and 5.3, with E^0 re-scaled to be centred on 0 V.

To conclude our investigation of the effects of dispersion on DC voltammograms, we present a comparison of the effects of including either or both of kinetic (k^0) and thermodynamic (E^0) dispersion on the half-height width, $W_{1/2}$, using distributions adapted from reference [88] and the reproduced Figures 5.2 and 5.3. The results of these simulations are shown in Figure 5.12 and Table 5.4. As we can see, even with this combination of scan rate and k^0 range meaning that most of the k^0 values are essentially identical, lying above the reversible limit, we still notice a 10 mV increase in $W_{1/2}$ from including the effects of both kinetic and thermodynamic dispersion, although the majority of the contribution appears to come from kinetic dispersion alone.

5.3.2 AC voltammetry

In order to orientate the reader before presenting our results relating to dispersion in the AC case, we will first include a brief discussion of the sensitivity of harmonics in AC voltammetry to different ranges of k^0 in the absence of dispersion, and then consider the implications of including, in particular, kinetic dispersion on some of

these harmonics.

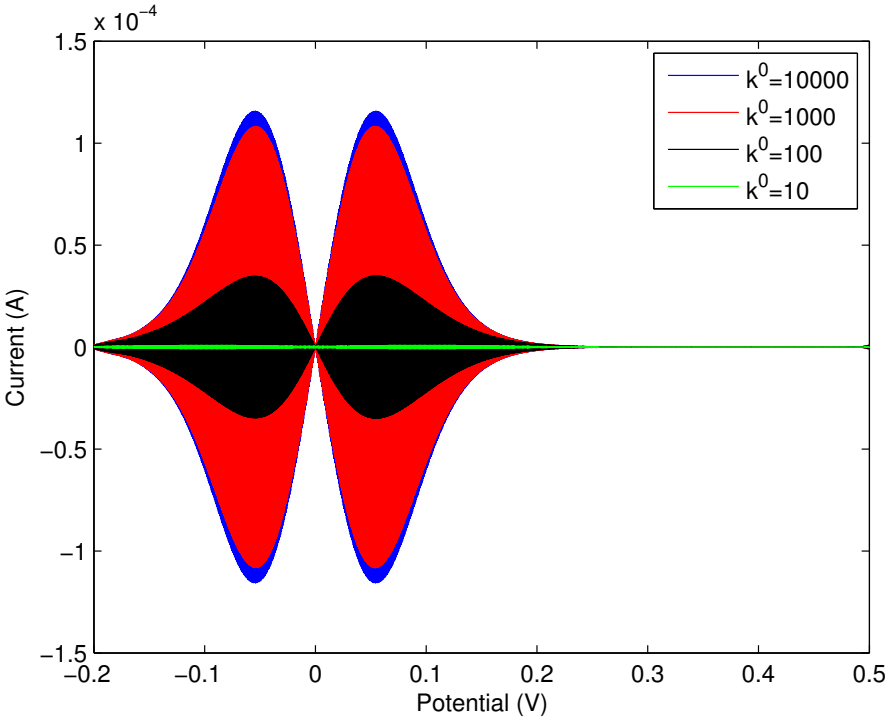

Figure 5.13: The effects of varying k^0 on the 2nd harmonic of an AC voltammetric experiment at 72 Hz and sine wave amplitude $\Delta E = 80$ mV. Clear variation in the figure is noticeable until k^0 is somewhere between 1000 and 10000, at which point further increases have no effect.

As we have remarked already, and in particular following our work in Chapter 3, DC voltammetry at $\nu = 100$ mV s^{-1} is sensitive to changes in k^0 only up to around $k^0 = 10$ s^{-1}. With our distribution of k^0 values having a mean above this limit, the effects on for example $W_{1/2}$ is lessened. Two methods of increasing sensitivity to k^0 would be either using a faster scan rate, ν, or running experiments using AC voltammetry, with a high frequency perturbation built in on top of the DC linear ramp. In practice, while it is possible to use significantly faster scan rates, one then encounters much greater problems caused by increased background

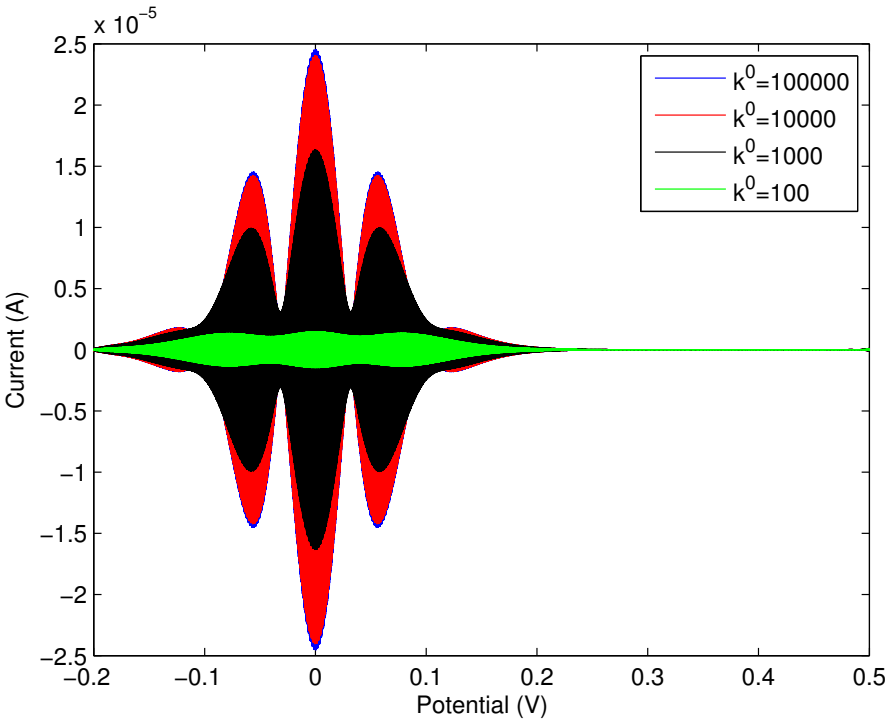

Figure 5.14: The effects of varying k^0 on the 5th harmonic of an AC voltammetric experiment at 72 Hz and sine wave amplitude $\Delta E = 80$ mV. Clear variation in the figure is noticeable until k^0 is somewhere between 10000 and 100000, at which point further increases have no effect.

current due to double layer capacitance. When using Fourier-transformed AC voltammetric techniques, these problems are less severe, and at the same time, access to higher harmonics provides even greater sensitivity to k^0, and almost a complete absence of double-layer charging current in an experimental setting. This increased sensitivity to k^0, again in the absence of dispersion effects, is shown in Figures 5.13 and 5.14, where we see that even using the same $\nu = 100$ mV s^{-1} scan rate, and an AC perturbation of amplitude 80 mV and frequency 72 Hz, we are able to detect variations in k^0 above $k^0 = 10000$ s^{-1} in the 5th harmonic.

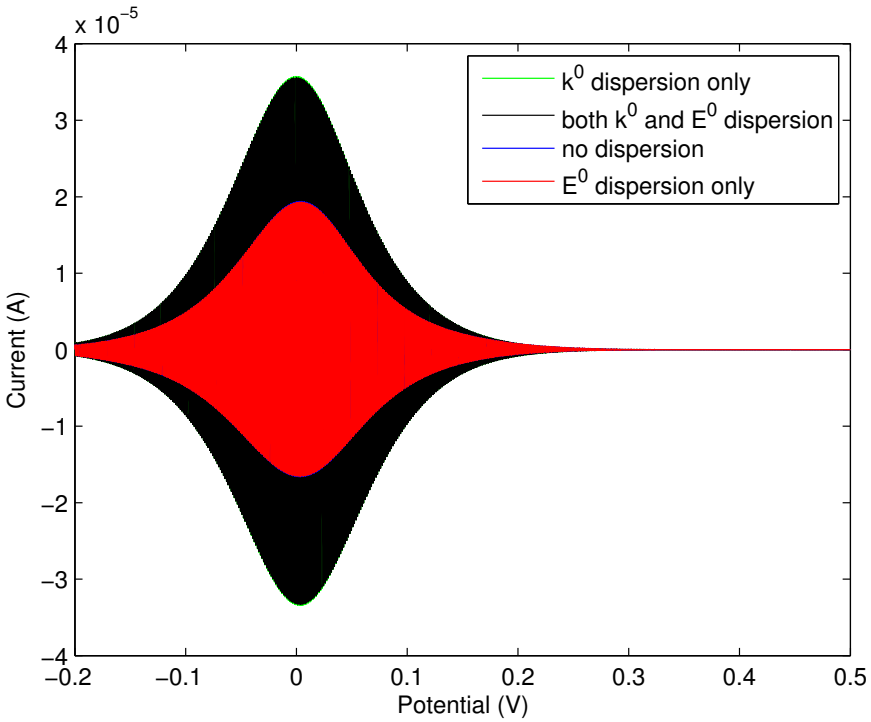

Figure 5.15: The effect of including all combinations of E^0 and k^0 dispersion, in quantities consistent with the distributions taken from [88], in an AC voltammetry simulation using a sine wave of amplitude 80 mV and frequency of 72 Hz on the overall time-domain voltammogram. We see again that k^0 dispersion effects dominate, with the black and green curves, representing simulations including k^0 dispersion with and without E^0 dispersion, being almost indistinguishable, as is also the case with the red and blue curves, representing simulations without k^0 dispersion and again, with and without E^0 dispersion.

Having illustrated the increased sensitivity to changes in k^0 in the frequency domain, we now return to the dispersion case, again using the typical levels of dispersion observed in the experiments reported in [88]. The results of including either, both, or neither of E^0 and k^0 dispersion in a simulation of AC voltammetry with amplitude 80 mV and frequency 72 Hz are pictured in Figure 5.15, showing the

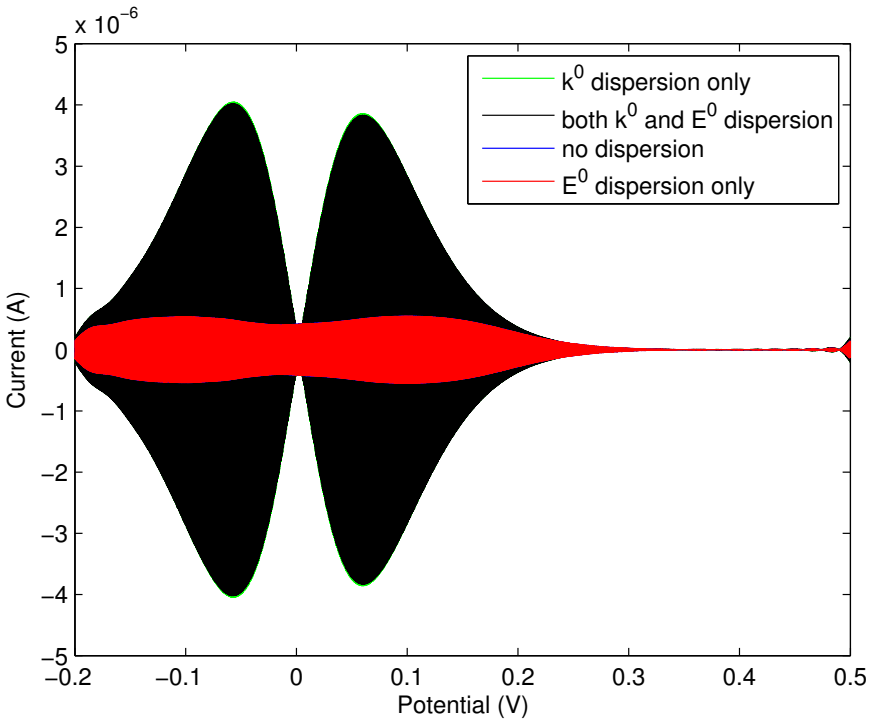

Figure 5.16: The effect of including all combinations of E^0 and k^0 dispersion in an AC voltammetry simulation using a sine wave of amplitude 80 mV and frequency of 72 Hz on the 2nd harmonic. Once again, the effects of k^0 dispersion are seen to be of far greater significance than those of E^0 dispersion, with the curves comparing the effects of including or excluding E^0 dispersion (blue vs red, green vs black) being almost indistinguishable.

time domain, Figure 5.16, showing the 2nd harmonic, and Figure 5.17, showing the 5th harmonic. In the case of AC voltammetry, there is not an intuitively obvious parameter we can use to quantify changes in the shape of the current response, unlike in the DC case, where $W_{1/2}$ fills this role. As a result, we will restrict ourselves to commenting on observable features of the graphs, as would be used in a heuristic parameter fitting exercise.

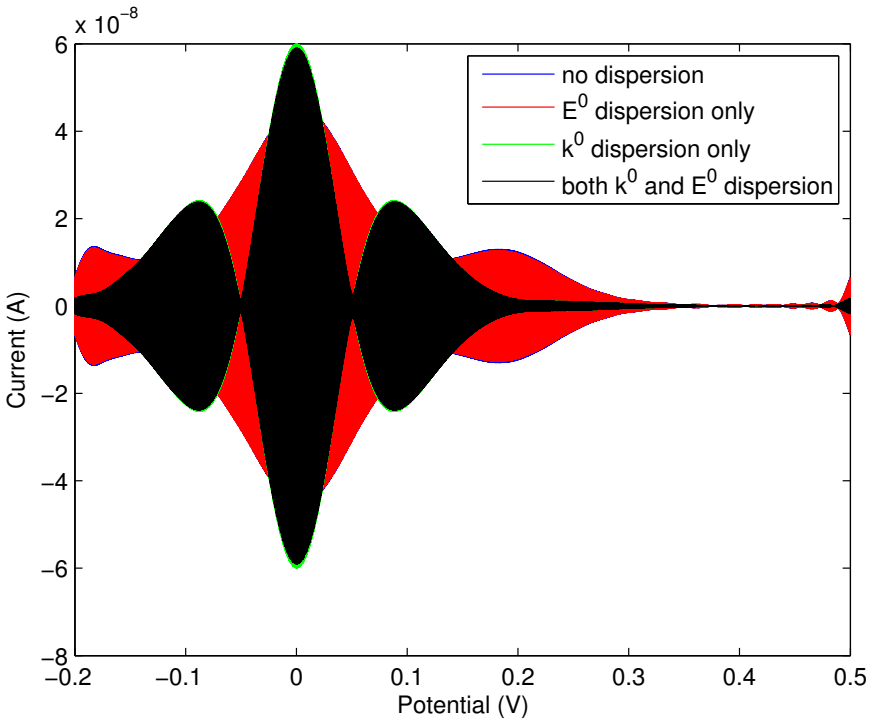

Figure 5.17: The effect of including all combinations of E^0 and k^0 dispersion in an AC voltammetry simulation using a sine wave of amplitude 80 mV and frequency of 72 Hz on the 5th harmonic. Yet again, the effects of k^0 dispersion are seen to be of far greater significance than those of E^0 dispersion, with the curves comparing the effects of including or excluding E^0 dispersion (blue vs red, green vs black) being almost indistinguishable.

Perhaps of most importance, we see in all three of these figures that although we consider all four combinations of kinetic and thermodynamic dispersion, when the distributions adapted from Figures 5.2 and 5.3 are used, the inclusion or exclusion of thermodynamic dispersion makes almost no difference to the resulting current. Indeed in all three of Figures 5.15, 5.16 and 5.17 we see the black and green curves showing the difference between including or excluding dispersion in E^0 when k^0 dispersion is included in simulations are almost indistinguishable, as are

the red and blue curves showing the inclusion and exclusion of E^0 dispersion when k^0 dispersion is excluded from simulations. These pairs of curves are, however, distinct from each other and it is the presence, or lack thereof, of kinetic dispersion which has the greatest impact. This is consistent with the results from the DC simulations given in Table 5.4.

The differences between the currents resulting from simulations with and without kinetic dispersion are also more pronounced in the case of AC voltammetry, when compared to the DC case. Even in the time domain, the peak current may vary significantly with k^0 although, just as in DC voltammetry, the overall area under the curve must remain constant in accordance with Faraday's law of electrolysis.

It is in the harmonics, however, that we see the greatest potential for development of a heuristic method for parameter estimation which may include the effects of dispersion. Each harmonic is sensitive to different ranges of k^0, so by splitting up the overall current into these components, we can gain a lot of information about which values of this parameter may be required to produce a good level of agreement between theory and experiment. In this example, we see that the 2nd harmonic, shown in Figure 5.16, exhibits not only a larger magnitude of current for simulations including kinetic dispersion, but a different overall shape as well. The 5th harmonic, shown in Figure 5.17, displays a similar magnitude of current when k^0 dispersion is included, but again the shapes of the curves are also markedly different. The 5th harmonic is insensitive to the lower values included in the k^0 distribution, and although it is significantly more sensitive to the higher values from this same distribution, their lower weighting means that they contribute only a little to the overall current. This results in the variation in shape, due to these higher values, but the corresponding discounting of low values means the magnitude of the peak current does not change significantly. The 2nd harmonic,

on the other hand, is sensitive to all values included in the k^0 distribution used, so not only do we see the expected shape due to the highest values, we also do not "lose" current due to the inclusion of low k^0 values.

5.4 Conclusions

In this chapter, we have started from the acknowledged discrepancies reported between theoretical predictions and experimental results for voltammetric studies undertaken on species confined to a monolayer on an electrode surface, and used data adapted from [88] to motivate the inclusion of kinetic and thermodynamic dispersion in an attempt to explain these discrepancies. We have taken an individual-based stochastic model for the electron transfer process of Equation (5.2), and shown that for the number of molecules present in a typical voltammetric experiment, the deterministic model using ODEs is a valid approximation, including in the presence of dispersion. We have then used our model to investigate the effects of including either or both of kinetic and thermodynamic dispersion in simulations of DC and AC voltammetry.

When the distributions reported in [88] were used, we found that dispersion in the values of E^0 is unlikely to be detectable experimentally due to its minimal impact at realistic parameter values [57], but that dispersion in k^0 can have a significant impact, and account for at least some of the unexplained variation between results predicted by theory and those obtained from experiments [6, 7, 16, 50, 57, 62, 79, 80, 88].

It is important to note that the field of surface-confined electrochemistry is less well-understood than its solution-phase counterpart, and all results obtained in

this chapter have been built upon certain modelling assumptions which may be disputed. We have used the Butler-Volmer model of electron-transfer with $\alpha = 0.5$ fixed in all simulations, however not only might it be possible that there could be dispersion in the value of α as well, but also arguments have been made for preferring the use of the Marcus-Hush model instead [96]. Our model is also built on the ideal thin film assumptions of a Langmuir isotherm and non-interacting molecules [56], but alternative isotherms [11, 48] and the possibility of allowing adsorbed molecules to react with one another [16], along with other reasons for non-ideal behaviour (for example [23,25,26,36,73,90]), have been proposed in some cases.

However, even though some of these alternatives might also assist in accounting for some of the fundamental differences between theoretical prediction and experimental results, they do not exclude the presence of dispersion. Indeed, the evidence for dispersion reported by Davis et al. [79, 80, 88] is compelling, and suggests that this phenomenon should still be taken into account in future efforts to model surface-confined voltammetric experiments.

Chapter 6

Conclusions and future work

The main goal towards which we have worked over the course of this project has been the development of an automated and operator-independent method for theory-experiment comparison in AC voltammetry. We have introduced a simple algorithm based on a least-squares optimisation, and tested this on both simulated and experimental data. The well-studied $[Fe(CN)_6]^{3-/4-}$ process from Chapter 2 served as a benchmark, and the algorithm produced parameter estimates consistent with those in the literature and those obtained using other operator-dependent methods.

In Chapter 3, we introduced the use of bootstrapping, using it to generate confidence intervals on parameter estimates, and hence comment on the appropriateness of using the fully-reversible or the quasi-reversible model to describe the $Fc^{0/+}$ process. In this way, we were able to explain some of the inconsistency in reported values of the rate constant, k^0, throughout the literature, and with this in mind, our algorithm again produced parameter estimates consistent with what was expected.

In Chapter 4, we undertook a theoretical study of an EC reaction mechanism. We saw that even in the case of one of the simplest coupled reaction systems, the complexity of parameter estimation increased significantly, with multiple regimes of behaviour observed based on combinations of the rate constants k^0, k_f and k_b. Further use of the bootstrapping technique allowed us to comment on the relative performance of our algorithm when applied to simulated data based on either DC or AC voltammetric experiments. We were also able to demonstrate some ability of the parameter recovery algorithm to select the correct reaction mechanism in this simple case.

In the final study of Chapter 5, we moved from the realm of solution-phase electrochemistry to reactions confined to an electrode surface. Motivated by the work of Davis et al. [79, 80, 88], we suggested a way of including the effects of kinetic and thermodynamic dispersion in our theoretical simulations, and performed a quantitative theoretical study of the effects of these phenomena on voltammetric experiments. We were able to show that using dispersion consistent with the distributions measured by Davis et al. [88], the effects of thermodynamic dispersion are negligible compared with the effects of kinetic dispersion. Furthermore, including the effects of kinetic dispersion in our simulations is sufficient to explain the inconsistencies between theoretical predictions and experimental results reported in the literature for studies of surface-confined electron transfer reactions.

6.1 Future work

Three particular areas requiring further investigation have become apparent during the course of this project.

Firstly, there is significant work to be done on extending the parameter recovery algorithm to include more reaction mechanisms and experimental setups. Our collaborators have proposed that about 10 reaction mechanisms would cover more than 90% of the reactions typically investigated using voltammetry. Producing mathematical models of these processes for inclusion in the parameter recovery algorithm is required, and then the aim would ultimately be to refine the algorithm so that it is capable of determining the reaction mechanism taking place when an unknown system was studied. From our work in Chapter 4, we have seen that as reaction mechanisms involving increasing numbers of steps are modelled, resulting in extra rate parameters for each additional reaction, problems can be encountered relating to identifiability of parameters and model selection. The problems that result from the ability to compensate for experimental noise in multiple ways by adjusting different parameters may become more tractable when mathematical techniques incorporating the tools of Bayesian statistics are employed, as will be discussed shortly.

In addition, now that we have provided some initial insight into the quantitative effects of dispersion on surface-confined reactions, an interesting problem would be to attempt a similar parameter estimation treatment of reactions taking place between surface-confined species, and to see whether it is possible to report estimates of not only the mean parameter values, but also their distributions. Further complexity can be introduced by allowing systems where species can adsorb or desorb onto or from an electrode surface, and electron transfer reactions can take place between species either in solution or confined to the electrode. Recent work [96] has also introduced the possibility of using the Marucs-Hush model of electron transfer [64] as an alternative to the empirical Butler-Volmer model, which may prove to be a superior choice in some scenarios. Finally for some particular reactions, experimentalists are interested in using different experimental setups,

such as microdisk or channel electrodes, or even electrodes which rotate during the course of an experiment, and these alternative geometries should also be taken into account.

A second area that could be explored would be the use of more advanced statistical methods for addressing the issues of parameter identifiability and model selection. Typically, a direct method for testing lack of identifiability might be used, involving examination of the inverse Hessian matrix used by the Newton method that we employ for our optimisation. A flat direction in the objective function surface is suggested by the inverse Hessian being singular or, equivalently, having at least one eigenvalue equal to zero. In our problem, the exact evaluation of the inverse Hessian is analytically intractible, and rather than use a computationally expensive numerical approximation, we have instead used the bootstrapping method of Chapters 3 and 4 to explore the objective function surface in the locality of the minimum value via the random re-distribution of noise onto the signal. While the bootstrapping method has given us some insight into identifiability, alternative methods based on Bayesian inference may also prove useful [49]. For model selection problems, such as the choice between the fully-reversible and quasi-reversible models in Chapter 3, or the E or EC mechanism models in Chapter 4, working in a Bayesian framework, which we began to develop in Chapter 1, also offers access to tools such as the Akaike Information Criterion [4, 24] as a method for determining which of the possible models is the most likely to fit the data being considered.

The third area which could produce significant advances is the study of "designer" input waveforms. In a standard AC voltammetry experiment, a single sine wave is usually superimposed onto the cyclic linear ramp from DC voltammetry. There is no reason, however, for restricting the AC perturbation to a single frequency and amplitude. If a measure can be provided for the identifiability of parameters from

a given system based on the controlled parameters of an input potential waveform, it should be possible to optimise this input in order to maximise the identifiability of parameters from the resulting experiment. This method has been applied with some success in other fields such as magnetic resonance [34], and is an exciting possibility for voltammetry. Some initial work relating to parameter identifiability and designer waveforms in voltammetry has been published by other authors [99, 101], but further investigation in this area could prove extremely productive.

6.2 Closing remarks

The opportunity to have worked on this project is one I am unlikely to forget. I have had the chance to experience research in the context of applying mathematical techniques to a real scientific problem, and to see the results of my theoretical work in action with the experimental examples. It has also been a fantastic chance to participate in a collaborative endeavour, and come to see the importance of people with different areas of expertise combining their skills to work towards a single objective. Alongside the mathematical applications, this has been one of several eye-opening experiences which I shall carry forward with me after the completion of this project.

Bibliography

[1] http://www.gamry.com/products/digielch-electrochemical-simulation-software/.

[2] http://www.comsol.com/products/multiphysics/.

[3] D. Abramson, B. Bethwaite, C. Enticott, S. Garic, and T. Peachey, *Parameter exploration in science and engineering using many-task computing*, IEEE Trans. Parallel and Distributed Syst., 22 (2011), pp. 960–973.

[4] H. Akaike, *A new look at the statistical model identification*, IEEE T. Automat. Contr., 19 (1978), pp. 716–723.

[5] D. F. Anderson, *A modified next reaction method for simulating chemical systems with time dependent propensities and delays*, J. Chem. Phys., 127 (2007), p. 214107.

[6] F. A. Armstrong, *Recent developments in dynamic electrochemical studies of adsorbed enzymes and their active sites*, Curr. Opin. Chem. Biol., 9 (2005), pp. 110–117.

[7] F. A. Armstrong, H. A. Heering, and J. Hirst, *Reaction of complex metalloproteins studied by protein-film voltammetry*, Chem. Soc. Rev., 26 (1997), pp. 169–179.

[8] C. E. Banks, T. J. Davies, G. G. Wildgoose, and R. G. Compton, *Electrocatalysis at graphite and carbon nanotube modified electrodes: edge-plane sites and tube ends are the reactive sites*, Chem. Commun., (2005), pp. 829–841.

[9] K. Bano, G. F. Kennedy, J. Zhang, and A. M. Bond, *Large amplitude Fourier transformed ac voltammetry at a rotating disc electrode: a versatile technique for covering Levich and flow rate insensitive regimes in a single experiment*, Phys. Chem. Chem. Phys., 14 (2012), pp. 4742–4752.

[10] A. S. Baranski, K. Winkler, and W. R. Fawcett, *New experimental evidence concerning the magnitude of the activation parameters for fast heterogeneous electron transfer reactions*, J. Electroanal. Chem., 313 (1991), pp. 367–375.

[11] A. J. Bard and L. R. Faulkner, *Electrochemical Methods: Fundamentals and Applications*, John Wiley & Sons, 2nd ed., 2001.

[12] E. Barsoukov and J. R. Macdonald, *Impedance Spectroscopy: Theory, Experiment, and Applications*, John Wiley & Sons, 2nd ed., 2005.

[13] C. Beriet and D. Pletcher, *A further microelectrode study of the influence of electrolye concentration on the kinetics of redox couples*, J. Electroanal. Chem., 375 (1994), pp. 213–218.

[14] T. Berzins and P. Delahay, *Oscillographic polarographic waves for the reversible deposition of metals on solid electrodes*, J. Am. Chem. Soc., 75 (1953), pp. 555–559.

[15] W. J. Blaedel and R. C. Engstrom, *Investigations of the ferricyanide-ferrocyanide system by pulsed rotation voltammetry*, Anal. Chem., 50 (1978), pp. 476–479.

[16] A. M. Bond, *Broadening Electrochemical Horizons: Principles and Illustration of Voltammetric and Related Techniques*, Oxford University Press, 2002.

[17] A. M. Bond, N. W. Duffy, D. M. Elton, and B. D. Fleming, *Characterization of nonlinear background components in voltammetry by use of large amplitude periodic perturbations and Fourier transform analysis*, Anal. Chem., 81 (2009), pp. 8801–8808.

[18] A. M. Bond, N. W. Duffy, S.-X. Guo, J. Zhang, and D. Elton, *Changing the look of voltammetry*, Anal. Chem., 77 (2005), pp. 186A–195A.

[19] A. M. Bond, T. L. E. Henderson, D. R. Mann, T. F. Mann, W. Thormann, and C. G. Zoski, *A fast electron transfer rate for the oxidation of ferrocene in acetonitrile or dichloromethane at platinum disk ultramicroelectrodes*, Anal. Chem., 60 (1988), pp. 1878–1882.

[20] A. M. Bond, R. J. O'Halloran, I. Ruzic, and D. E. Smith, *Fundamental and second harmonic alternating current cyclic voltammetric theory and experimental results for simple electrode reactions involving solution-soluble redox couples*, Anal. Chem., 48 (1976), pp. 872–883.

[21] A. M. Bond, R. J. O'Halloran, I. Ruzic, and D. E. Smith, *Fundamental and second harmonic alternating current cyclic voltammetric theory and experimental results for simple electrode reactions involving amalgam formation*, Anal. Chem., 50 (1978), pp. 216–223.

[22] R. P. Brent, *Algorithms for Minimization without Derivatives*, Prentice Hall, 1973.

[23] A. P. Brown and F. C. Anson, *Cyclic and differential pulse voltammetric behavior of reactants confined to the electrode surface*, Anal. Chem., 49 (1977), pp. 1589–1595.

[24] K. P. Burnham and D. R. Anderson, *Model Selection and Multimodel Inference: A Practical Information-Theoretic Approach*, Springer Verlag, 2nd ed., 2002.

[25] J. Q. Chambers, K. Scaboo, and C. D. Evans, *Cyclic voltammetry of a $(TCNQ)^{0/-1}$ solid-state redox couple role of nucleation and nonideality for a square scheme surface redox reaction*, J. Electrochem. Soc., 143 (1996), pp. 3039–3045.

[26] C. E. D. Chidsey and R. W. Murray, *Redox capacity and direct current electron conductivity in electroactive materials*, J. Phys. Chem., 90 (1986), pp. 1479–1484.

[27] R. G. Compton and C. E. Banks, *Understanding Voltammetry*, Imperial College Press, 2nd ed., 2011.

[28] R. M. Crooks and A. J. Bard, *Electrochemistry in near-critical and supercritical fluids: Part VI. the electrochemistry of ferrocene and phenazine in acetonitrile between 25 and* 300 $^\circ C$, J. Electroanal. Chem., 243 (1988), pp. 117–131.

[29] P. H. Daum and C. G. Enke, *Electrochemical kinetics of the ferri-ferrocyanide couple on platinum*, Anal. Chem., 41 (1969), pp. 653–656.

[30] T. J. Davies, C. E. Banks, and R. G. Compton, *Voltammetry at spatially heterogeneous electrodes*, J. Solid State Electrochem., 9 (2005), pp. 797–808.

[31] T. J. Davies, R. R. Moore, C. E. Banks, and R. G. Compton, *The cyclic voltammetric response of electrochemically heterogeneous surfaces*, J. Electroanal. Chem., 574 (2004), pp. 123–152.

[32] P. Delahay, *Theory of irreversible waves in oscillographic polarography*, J. Am. Chem. Soc., 75 (1953), pp. 1190–1196.

[33] L. dos Santos, V. Climent, C. F. Blanford, and F. A. Armstrong, *Mechanistic studies of the 'blue' Cu enzyme, bilirubin oxidase, as a highly efficient electrocatalyst for the oxygen reduction reaction*, Phys. Chem. Chem. Phys., 12 (2010), pp. 13962–13974.

[34] I. Drobnjak, B. Siow, and D. C. Alexander, *Optimizing gradient waveforms for microstructure sensitivity in diffusion-weighted MR*, J. Magn. Reson., 206 (2010), pp. 41–51.

[35] B. Efron and R. J. Tibshirani, *An Introduction to the Bootstrap*, Chapman and Hall, 1993.

[36] S. W. Feldberg and I. Rubinstein, *Unusual quasi-reversibility (UQR) or apparent non-kinetic hysteresis in cyclic voltammetry: An elaboration upon the implications of n-shaped free energy relationships as explanation*, J. Electroanal. Chem., 240 (1988), pp. 1–15.

[37] V. Fourmond, C. Baffert, K. Sybirna, T. Lautier, A. Abou Hamdan, S. Dementin, P. Soucaille, I. Meynial Salles, H. Bottin, and C. Leger, *Steady-state catalytic wave-shapes for 2-electron reversible electrocatalysts and enzymes*, J. Am. Chem. Soc., 135 (2013), pp. 3926–3938.

[38] D. J. Gavaghan and A. M. Bond, *A complete numerical simulation of the techniques of alternating current linear sweep and cyclic voltammetry: analysis of a reversible process by conventional and fast Fourier transform methods*, J. Electroanal. Chem., 480 (2000), pp. 133–149.

[39] D. J. Gavaghan and A. M. Bond, *Numerical simulation of the effects of experimental error on the higher harmonic components of Fourier transformed AC voltammograms*, Electroanalysis, 18 (2006), pp. 333–344.

[40] D. J. Gavaghan, D. Elton, and A. M. Bond, *A comparison of sinusoidal, square wave, sawtooth, and staircase forms of transient ramped voltammetry when a reversible process is analysed in the frequency domain*, J. Electroanal. Chem., 513 (2001), pp. 73–86.

[41] D. J. Gavaghan, J. C. Myland, and K. B. Oldham, *The effect of periodic modulation on the aperiodic current in linear-scan and cyclic voltammetries*, J. Electroanal. Chem., 516 (2001), pp. 2–9.

[42] M. A. Gibson and J. Bruck, *Efficient exact stochastic simulation of chemical systems with many species and many channels*, J. Phys. Chem. A, 104 (2000), pp. 1876–1889.

[43] P. E. Gill and W. Murray, *Algorithms for the solution of the nonlinear least-squares problem*, SIAM J. Numer. Anal., 15 (1978), pp. 977–992.

[44] D. T. Gillespie, *A general method for numerically simulating the stochastic time evolution of coupled chemical reactions*, J. Comput. Phys., 22 (1976), pp. 403–434.

[45] D. T. Gillespie, *Exact stochastic simulation of coupled chemical reactions*, J. Phys. Chem., 81 (1977), pp. 2340–2361.

[46] S. Guo, J. Zhang, D. M. Elton, and A. M. Bond, *Fourier transform large-amplitude alternating current cyclic voltammetry of surface-bound azurin*, Anal. Chem., 76 (2004), pp. 166–177.

[47] P. Heiduschka and J. Dittrich, *Impedance spectroscopy and cyclic voltammetry at bare and polymer coated glassy carbon electrodes*, Electrochim. Acta, 37 (1992), pp. 2573–2580.

[48] J. Heyrovsky and J. Kuta, *Principles of Polarography*, Academic Press, 1966.

[49] K. E. Hines, T. R. Middendorf, and R. W. Aldrich, *Determination of parameter identifiability in nonlinear biophysical models: A Bayesian approach*, J. Gen. Physiol., 143 (2014), pp. 401–416.

[50] J. Hirst and F. A. Armstrong, *Fast-scan cyclic voltammetry of protein films on pyrolytic graphite edge electrodes: Characteristics of electron exchange*, Anal. Chem., 70 (1998), pp. 5062–5071.

[51] M. J. Honeychurch and A. M. Bond, *Numerical simulation of fourier transform alternating current linear sweep voltammetry of surface bound molecules*, J. Electroanal. Chem., 529 (2002), pp. 3–11.

[52] X. Ji, C. E. Banks, A. Crossley, and R. G. Compton, *Oxygenated edge plane sites slow the electron transfer of the ferro-/ferricyanide redox couple at graphite electrodes*, ChemPhysChem, 7 (2006), pp. 1337–1344.

[53] K. M. Kadish, J. Q. Ding, and T. Malinski, *Resistance of nonaqueous solvent systems containing tetraalkylammonium salts. evaluation of heterogeneous electron transfer rate constants for the ferrocene/ferrocenium couple*, Anal. Chem., 56 (1984), pp. 1741–1744.

[54] K. R. Kneten and R. L. McCreery, *Effects of redox system structure on electron-transfer kinetics at ordered graphite and glassy carbon electrodes*, Anal. Chem., 64 (1992), pp. 2518–2524.

[55] S. C. S. Lai, A. N. Patel, K. McKelvey, and P. R. Unwin, *Definitive evidence for fast electron transfer at pristine basal plane graphite from high-resolution electrochemical imaging*, Angew. Chem. Int. Ed., 124 (2012), pp. 5501–5504.

[56] E. Laviron, *Theoretical study of a reversible reaction followed by a chemical reaction in thin layer linear potential sweep voltammetry*, J. Electroanal. Chem., 39 (1972), pp. 1–23.

[57] C.-Y. Lee and A. M. Bond, *Systematic evaluation of electrode kinetics and impact of surface heterogeneity for surface-confined proteins using analysis of harmonic components available in sinusoidal large-amplitude Fourier transformed ac voltammetry*, Anal. Chim. Acta, 652 (2009), pp. 205–214.

[58] C.-Y. Lee, J. P. Bullock, G. F. Kennedy, and A. M. Bond, *Effects of coupled homogeneous chemical reactions on the response of large-amplitude AC voltammetry: Extraction of kinetic and mechanistic information by Fourier transform analysis of higher harmonic data*, J. Phys. Chem. A, 114 (2010), pp. 10122–10134.

[59] C.-Y. Lee, B. D. Fleming, J. Zhang, S.-X. Guo, D. M. Elton, and A. M. Bond, *Evaluation of levels of defect sites present in highly ordered pyrolytic graphite electrodes using capacitive and faradaic current components derived simultaneously from large-amplitude Fourier transformed ac voltammetric experiments*, Anal. Chem., 81 (2009), pp. 584–594.

[60] C.-Y. Lee, S.-X. Guo, A. M. Bond, and K. B. Oldham, *Effect of heterogeneity on the dc and ac voltammetry of the* $[Fe(CN)_6]^{3-/4-}$ *solution-phase process at a highly ordered pyrolitic graphite electrode*, J. Electroanal. Chem., 615 (2008), pp. 1–11.

[61] C.-Y. Lee, G. P. Stevenson, A. Parkin, M. M. Roessler, R. E. Baker, K. Gillow, D. J. Gavaghan, F. A. Armstrong, and A. M. Bond, *Theoretical and experimental investigation of surface-confined two-center metalloproteins by large-amplitude Fourier transformed ac voltammetry*, J. Electroanal. Chem., 656 (2011), pp. 293–303.

[62] C. Leger and P. Bertrand, *Direct electrochemistry of redox enzymes as a tool for mechanistic studies*, Chem. Rev., 108 (2008), pp. 2379–2438.

[63] C. Leger, A. K. Jones, S. P. J. Albracht, and F. A. Armstrong, *Effect of a dispersion of interfacial electron transfer rates on steady state catalytic electron transport in [NiFe]-hydrogenase and other enzymes*, J. Phys. Chem. B, 106 (2002), pp. 13058–13063.

[64] R. A. Marcus, *On the theory of oxidation-reduction reactions involving electron transfer. I*, J. Chem. Phys., 24 (1956), pp. 966–978.

[65] F. J. Massey, *The Kolmogorov-Smirnov test for goodness of fit*, J. Am. Stat. Assoc., 46 (1951), pp. 68–78.

[66] H. Matsuda and Y. Ayabe, *Zur theorie der Randles-Sevcikschen kathodenstrahl-polarographie*, Z. Elektrochem., 59 (1955), pp. 494–503.

[67] R. L. McCreery, in Electroanalytical Chemistry, A. J. Bard, ed., Marcel Dekker, 1991, pp. 221–374.

[68] R. L. McCreery, *Advanced carbon electrode materials for molecular electrochemistry*, Chem. Rev., 108 (2008), pp. 2646–2687.

[69] R. L. McCreery and M. T. McDermott, *Comment on electrochemical kinetics at ordered graphite electrodes*, Anal. Chem., 84 (2012), pp. 2602–2605.

[70] M. T. McDermott, K. Kneten, and R. L. McCreery, *Anthraquinonedisulfonate adsorption, electron-transfer kinetics, and capacitance on graphite electrodes: the important role of surface defects*, J. Phys. Chem., 96 (1992), pp. 3124–3130.

[71] G. P. Morris, A. N. Simonov, E. A. Mashkina, R. Bordas, K. Gillow, R. E. Baker, D. J. Gavaghan, and A. M. Bond, *A comparison of fully automated methods of data analysis and computer assisted heuristic methods in an electrode kinetic study of the pathologically variable $[Fe(CN)_6]^{3-/4-}$ process by AC voltammetry*, Anal. Chem., 85 (2013), pp. 11780–11787.

[72] K. W. Morton and D. F. Mayers, *Numerical Solution of Partial Differential Equations*, Cambridge University Press, 1994.

[73] R. D. Mounts, K. Widlund, H. Gunadi, J. Perez, and B. Pech, *Spectroelectrochemistry of 9-aminoacridine tetracyanoquinodimethane conducting salt electrodes. proton transport and cation intercalation solid state redox reactions*, J. Electroanal. Chem., 340 (1992), pp. 227–239.

[74] J. A. Nelder and R. Mead, *A simplex method for function minimization*, Comput. J., 7 (1965), pp. 308–313.

[75] R. S. Nicholson, *Theory and application of cyclic voltammetry for measurement of electrode reaction kinetics*, Anal. Chem., 37 (1965), pp. 1351–1355.

[76] R. S. Nicholson and I. Shain, *Theory of stationary electrode polarography single scan and cyclic methods applied to reversible, irreversible, and kinetic systems*, Anal. Chem., 36 (1964), pp. 706–723.

[77] Numerical Algorithms Group. `http://www.nag.co.uk`.

[78] A. N. Patel, M. G. Collignon, M. A. O'Connel, W. O. Y. Hung, K. McKelvey, J. V. Macpherson, and P. R. Unwin, *A new view of electrochemistry at highly oriented pyrolitic graphite*, J. Am. Chem. Soc., 134 (2012), pp. 20117–20130.

[79] A. V. Patil and J. J. Davis, *Visualizing and tuning thermodynamic dispersion in metalloprotein monolayers*, J. Am. Chem. Soc., 132 (2010), pp. 16938–16944.

[80] A. V. Patil and J. J. Davis, *Molecular scale bioelectrochemistry*, Coord. Chem. Revs, 255 (2011), pp. 1970–1980.

[81] H. V. Patten, K. E. Meadows, L. A. Hutton, J. G. Iacobini, D. Battistel, K. McKelvey, A. W. Colburn, M. E. Newton, J. V. Macpherson, and P. R. Unwin, *Electrochemical mapping reveals direct correlation between heterogeneous electron-transfer kinetics and local density of states in diamond electrodes*, Angew. Chem. Int. Ed., 51 (2012), pp. 7002–7006.

[82] R. M. Penner, M. J. Heben, T. L. Longin, and N. S. Lewis, *Fabrication and use of nanometer-sized electrodes in electrochemistry*, Science, 250 (1990), pp. 1118–1121.

[83] J. E. B. Randles, *A cathode ray polarograph. Part II–the current-voltage curves*, Trans. Faraday Soc., 44 (1948), pp. 327–338.

[84] T. Reda and J. Hirst, *Interpreting the catalytic voltammetry of an adsorbed enzyme by considering substrate mass transfer, enzyme turnover, and interfacial electron transport*, J. Phys. Chem. B, 110 (2006), pp. 1394–1404.

[85] W. H. Reinmuth, *Theory of stationary electrode polarography*, Anal. Chem., 33 (1961), pp. 1793–1794.

[86] M. Rudolph, D. P. Reddy, and S. W. Feldberg, *A simulator for cyclic voltammetric responses*, Anal. Chem., 66 (1994), pp. 589A–600A.

[87] I. Ruzic and S. Feldberg, *The heterogeneous equivalent: A method for digital simulation of electrochemical systems with compact reaction layers*, J. Electroanal. Chem., 50 (1974), pp. 153–162.

[88] J. M. Salverda, A. V. Patil, G. Mizzon, S. Kuznetsova, G. Zauner, N. Akkilic, G. W. Canters, J. J. Davis, H. A. Heering, and T. J. Aartsma, *Fluorescent cyclic voltammetry of immobilized azurin: Direct observation of thermodynamic and kinetic heterogeneity*, Angew. Chem., 122 (2010), pp. 5912–5915.

[89] H. Scholl and K. Socha, *Cyclic voltammetry of some ferrocenephanes in acetonitrile*, Electrochim. Acta, 36 (1991), pp. 689–694.

[90] U. Schroeder, K. B. Oldham, J. C. Myland, P. J. Mahon, and F. Scholz, *Modelling of solid state voltammetry of immobilized microcrystals assuming an initiation of the electrochemical reaction at a three-phase junction*, J. Solid State Electrochem., 4 (2000), pp. 314–324.

[91] A. Sevcik, *Oscillographic polarography with periodical triangular voltage*, Collect. Czech. Chem. Commun, 13 (1948), pp. 349–377.

[92] A. A. Sher, A. M. Bond, D. J. Gavaghan, K. Harriman, S. W. Feldberg, N. W. Duffy, S. Xuan Guo, and J. Zhang, *Resistance, capacitance, and electrode kinetic effects in Fourier-transformed large-amplitude sinusoidal voltammetry: Emergence of powerful and intuitively obvious tools for recognition of patterns of behaviour*, Anal. Chem., 76 (2004), pp. 6214–6228.

[93] D. S. Sivia, *Data Analysis: A Bayesian Tutorial*, Oxford University Press, 1996.

[94] D. E. Smith, in Electroanalytical Chemistry, A. J. Bard, ed., Marcel Dekker, 1966, pp. 1–148.

[95] G. P. Stevenson, *Mathematical modelling of ac voltammetry and its application in electrochemistry and biochemistry*, PhD thesis, University of Oxford, 2010.

[96] G. P. Stevenson, R. E. Baker, G. F. Kennedy, A. M. Bond, D. J. Gavaghan, and K. Gillow, *Access to enhanced differences in Marcus-Hush and Butler-Volmer electron transfer theories by systematic analysis of higher order AC harmonics*, Phys. Chem. Chem. Phys, 15 (2013), pp. 2210–2221.

[97] G. P. Stevenson, C.-Y. Lee, G. F. Kennedy, A. Parkin, R. E. Baker, K. Gillow, F. A. Armstrong, D. J. Gavaghan, and A. M. Bond, *Theoretical analysis of the two-electron transfer reaction and experimental studies with surface-confined cytochrome c peroxidase using*

large-amplitude fourier transformed ac voltammetry, Langmuir, 28 (2012), pp. 9864–9877.

[98] P. Sun and M. V. Mirkin, *Kinetics of electron-transfer reactions at nanoelectrodes*, Anal. Chem., 78 (2006), pp. 6526–6534.

[99] Y. Tan, G. P. Stevenson, R. E. Baker, D. Elton, K. Gillow, J. Zhang, A. M. Bond, and D. J. Gavaghan, *Designer based fourier transformed voltammetry: A multi-frequency, variable amplitude, sinusoidal waveform*, J. Electroanal. Chem., 634 (2009), pp. 11–21.

[100] The Mathworks, Inc. `http://www.mathworks.com/`.

[101] A. Vikhansky, S. M. Matthews, and A. C. Fisher, *Numerical analysis of alternating current voltammetry: Identifiability, parameter selection and experimental design*, Ind. Eng. Chem. Res., 50 (2011), pp. 2831–2838.

[102] A. F. Wait, A. Parkin, G. M. Morley, L. dos Santos, and F. A. Armstrong, *Characteristics of enzyme-based hydrogen fuel cells using an oxygen-tolerant hydrogenase as the anodic catalyst*, J. Phys. Chem. C, 114 (2010), pp. 12003–12009.